COMPUTATIONAL INVESTIGATION OF LIGHT HARVESTING IN PURPLE PHOTOSYNTHETIC BACTERIA

BY

JOHAN ALBERT STRÜMPFER

DISSERTATION

Submitted in partial fulfillment of the requirements
for the degree of Doctor of Philosophy in Biophysics and Computational Biology
in the Graduate College of the
University of Illinois at Urbana-Champaign, 2012

Urbana, Illinois

Doctoral Committee:

Professor Robert M. Clegg, Chair
Professor Klaus J. Schulten, Director of Research
Professor Govindjee
Professor Antony R. Crofts

Abstract

Purple photosynthetic bacteria achieve remarkably high light harvesting efficiency, thus reconciling multiple competing processes in the chromatophore. The first step in photosynthesis is the capture and transport of light energy in the form of short-lived electronic excitation called excitons. Rapid long-range exciton transport is key to the high light harvesting efficiency associated with purple bacteria. The light harvesting system of purple bacteria consists of light harvesting complex 2 (LH2), light harvesting complex 1 (LH1) and reaction center (RC) assembeled into a structure known as the chromatophore. The pigments embedded into the complexes in the chromatophore are placed close together and are tightly held by their surrounding proteins. Pigment excited states thus interact very strongly and are also strongly coupled to surrounding environmental fluctuation. Exciton dynamics in purple bacteria is thus described using the hierarchy equations of motion (HEOM) for open quantum systems, which does not rely on assumptions of relative interaction strengths and includes quantum coherence effects. An efficient implementation of the HEOM is developed and utilized to describe exciton dynamics in the light harvesting complexes of purple bacteria, and calculate excitation transfer between LH2-LH2, LH2-LH1 and LH1-RC pairs. It is shown that strong environmental coupling is reponsible for rapid exciton relaxation into equilibrium prior to inter-complex exciton transfer, thus allowing inter-complex transfer rates to be calculated with the much simpler generalized Förster theory. The effect of intra-complex correlated environmental fluctuations is also examined and found to substantially affect inter-complex exciton transfer. Strong coupling between pigments within a complex results in inter-pigment quantum coherence that significantly improves the rate of inter-complex exciton transfer, vital to efficient light harvesting in purple bacteria.

To my family and friends, for their love and support.

Acknowledgements

The work presented in this dissertation is the result of many years of intense labour, with many people key to its completion and all of whom I owe many thanks:

First and foremost is my mom and dad. Without the education they provided for me, the values they instilled in me, their unquestioning love and support I would not be the person I am today, and would not have been able to undertake this research. My sister Lani always supports me and is available for wonderful chats, provided I let her know to make time in her busy social schedule. My mom and dad's respective families have always been there, indulging my incessant talking about research and computing and providing their unwavering support. Dankie ma, pa, sus en families vir al julle liefde en steun en die lekker kersfees en ander tye wat ek in Suid Afrika kon spandeer.

My wife Louise is my love and my greatest supporter through the excitement of new results and the trials of encountered difficulties. She has supported me from the start despite us living in different continents and then time zones and cities for nearly four years. She has stuck by me and kept me going throughout and for her I'm eternally grateful. Thank you for your love and for the love and support of your family.

My advisor Klaus Schulten has been central in guiding me through my work, teaching me how to perform cutting edge research and providing me with the ability to distil and communicate complex ideas. Melih Sener for introducing to me many of the concepts and methods in photosynthesis and for many enjoyable and stimulating discussions. Ilia Solov'yov for great chats over good coffee. JC Gumbart for showing me how to successfully navigate the subtleties of research in the TCBG. John Stone for long discussions and showing me why it's important to know the details of modern computer hardware. David Tanner for being the best office mate and his daughters for decorating our office. Jen Hsin for her sense of humour and showing me how to give a good TCBG-directed presentation. Danielle Chandler for being a font of purple bacteria related knowledge and her subtle sense of humour. Yanxin Lui for pushing me to implement a method in NAMD, and then folding a protein with it. Chaitanya Sathe for being a great travel partner to Germany. Eduardo Cruz, Leo

Trabuco and Eduard Schreiner for inviting me to fun soccer games and the tradition of Monday after-meeting lunch. The TCBG has been an amazing environment in which to work with too many people making it great to mention here.

Of great assistance has been my collaborators and has it has been an absolute pleasure to work with them. Chris Chipot for great chats about science, and not science, and putting up with all my failed crazy ideas. Ulrich Kleinekathöfer and his group in Bremen have been great to work with and discuss the complex, quantum nature of the world.

There are many who have helped me in Urbana-Champaign: friends, colleagues and advisors. I am deeply thankful to all of them

This work was supported by grants R01-GM067887 and P41-RR005969 from the National Institutes of Health, and MCB-1157615 and PHY0822613 from the National Science Foundation. Supercomputer time was provided by the National Center for Supercomputing Applications, the Pittsburgh Supercomputer Center, the Texas Advanced Computing Center, and the National Institute for Computational Sciences through the National Science Foundation with the Extreme Science and Engineering Discovery Environment (XSEDE) grant XRAC-MCA93S028. All molecular visualizations were made with VMD [11].

Table of Contents

List of Tables

List of Figures

Chapter 1

Light harvesting in purple bacteria

1.1 Introduction

Solar energy harvested by photosynthetic organisms is the primary source of energy in the biosphere [12]. In photosynthetic purple bacteria, light harvesting is performed by spherical, tubular or lamellar membrane domains called chromatophores (Fig. 1.1a) [2–5, 7], comprising supra-molecular assemblies of hundreds of cooperating protein subunits that convert short-lived electronic excitations resulting from photon absorption to stable chemical energy. Chromatophores constitute the simplest known photosynthetic system and, therefore, are ideal for study [13, 14].

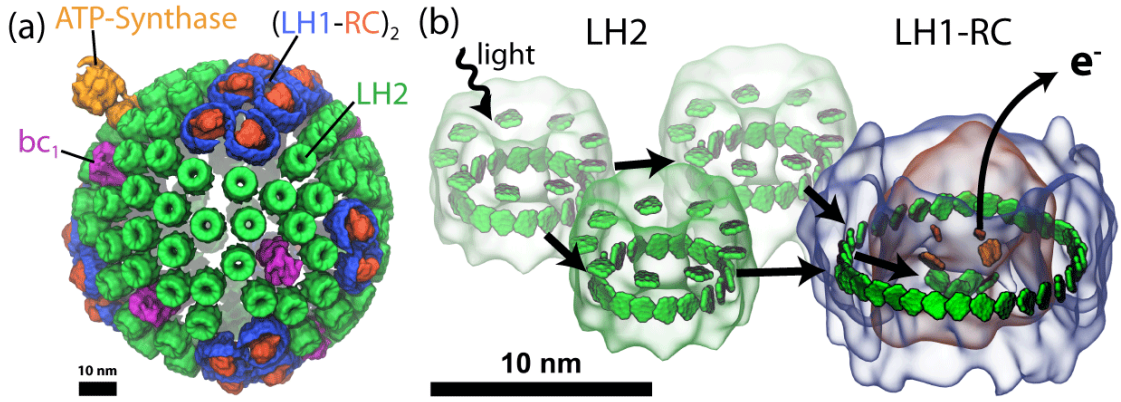

Figure 1.1: (a) Chromatophore from *Rb. sphaeroides* consisting of LH2s (green), LH1-RC dimers (red, blue), cyt. bc_1 (purple) and ATP synthase (orange). (b) The so-called "light reactions" of photosynthesis: light energy absorbed by BChls (green squares) is transferred (arrows) to a RC where an electron is transferred (see text), establishing a charge gradient. Part (b) shows the monomeric form of LH1-RC.

Photosynthesis in purple bacteria begins with photon absorption by the pigment-protein com-

plexes, light harvesting complex 2 (LH2) and light harvesting complex 1 (LH1). Excitation energy is transferred between LH2s, from LH2 to LH1 and, subsequently, to a reaction center (RC), as shown in Fig. 1.1b, initiating in the RC transmembrane electron transfer. This transfer places electrons jointly with cytoplasmic protons onto molecules of quinone, Q, reducing them to quinol, QH_2. Quinol diffuses through the chromatophore membrane to cytochrome (cyt.) bc_1 complexes where electrons and protons are separated from quinol, thus reforming quinone; the electrons are shuttled back to RC and the protons are deposited on the periplasmic side of the membrane. Thus, initial electron transfer produces a proton gradient across the cellular membrane, driving ATP synthesis. [12, 15, 16]

Table 1.1: Components of a chromatophore*

LH2 (60-100)		LH1 monomer (10-20)	
Protein components:		Protein components:	
9	α-subunits	16	α-subunits
9	β-subunits	16	β-subunits
Cofactors:		Cofactors:	
27	bacteriochlorophylls	32	bacteriochlorophylls
9	carotenoids	16	carotenoids

RC (10-20)		ATP-synthase (1)	
Protein components:		Protein components:	
1	L-subunit	3	α-subunits
1	M-subunit	3	β-subunits
1	H-subunit	1	γ-subunit
Cofactors:		1	δ-subunit
4	bacteriochlorophylls	1	ϵ-subunit
2	bacteriopheophytins	1	a-subunit
1	carotenoid	1	b-subunit
2	quinones	10-11	c-subunits

cyt. bc_1 (5-10)			
Protein components:		Cofactors:	
2	Cytochrome b	4	Fe-S centers
2	Cytochrome c_1	6	hemes
2	Rieske-subunits		

* Numbers in parentheses give approximate number of the complexes in the chromatophore.

The solution of the structure of the first light harvesting protein complex, LH2, in 1995 [17] and 1996 [18] immediately suggested strong excitonic coupling among a ring of closely spaced BChls and, accordingly, a role of quantum coherence in purple bacterial light harvesting [19]. Excitation is coherently shared between pigments within light harvesting complexes LH1 and LH2, forming what is known as excitons [20]. The amount of coherence between the pigments, often characterized by the coherence length or oscillator strength, determines how each exciton state participates in

excitation transfer to nearby complexes. Exciton states greatly enhance the rate of inter-complex excitation transfer, improving overall light harvesting efficiency [7].

Although the calculation of inter-complex excitation transfer rates for the purple bacterial light-harvesting complexes have been performed [3–5, 7], they have been done with theories that use previously untested assumptions about the exciton dynamics of the system. These assumptions have now been tested for inter-LH2 excitation transfer [1, 6], LH2-LH1 transfer [9] and LH1-RC [10] excitation transfer. This thesis presents the results of the investigation into excitation transfer and dynamics in pigment-protein complexes of purple photosynthetic bacteria.

1.2 Light harvesting complexes

The light harvesting complex LH2. The light-harvesting process begins with light-harvesting complex II (LH2), also referred to as the peripheral light-harvesting complex antenna. LH2 is a ring-shaped protein complex, formed by 8 or 9 identical subunits. [18, 19] Each subunit contains two separate transmembrane helices which serve as a scaffold for the embedded pigment molecules, of which there are three BChls and one carotenoid per subunit (see Fig. 1.2 and Table 1.1). Altogether, an LH2 is then made of 54 seperate components. LH2 complexes are found in large numbers (100-200) in the chromatophore and act as a broad light-harvesting antenna that funnels energy to the LH1-RC complexes (see Fig. 1.1). Through the LH2 complexes, the chromatophore not only realizes excellent light-absorption, but also makes use of light at different wavelengths, namely the far-red light absorbed by the bacteriochlorophylls and yellow-green light absorbed by the carotenoids. While the bacteriocholorphylls in LH1 absorb maximally at 875 nm, the BChls in LH2 absorb maximally at 800 and 850 nm; the carotenoid molecule absorbs maximally at 500 nm. Naturally, excitation is transferred most easily energetically downhill, namely from 500 nm pigments [21] to 800 nm pigments to 850 nm pigments onto 875 nm ones, but opposite transfer is also possible, in particular from 875 nm to 850 nm pigments as the energy difference is 0.96 kcal/mol, which is 1.62 k_BT (k_BT = thermal energy at temperature T; k_B is the Boltzmann constant). The absorption of 850-800 nm and 500 nm photons is the result of evolutionary pressure, as purple bacteria are found in murky water where only light around 800 nm and 500 nm penetrates[22, 23]; other wavelengths of light being harvested by plants and algae living "above" the bacteria, i.e. they are closer to the sun. A review of the action of LH2 is available [24].

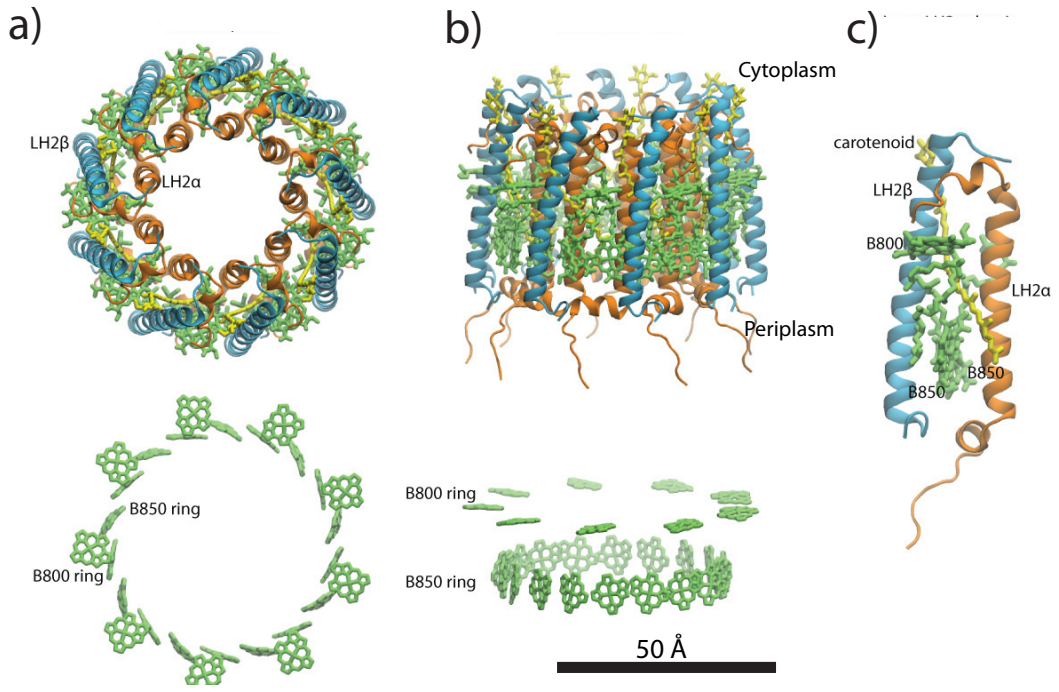

Figure 1.2: (a) An LH2 complex from *Rb. sphaeroides* as viewed from the top, showing the 9-fold symmetry of the complex and the placement of the pigment molecules. (b) LH2 complex as viewed from the side. (c) LH2 subunit. Each LH2 subunit is composed of two transmembrane helices, called the α helix (colored orange) and the β helix (colored blue), three bacteriochlorophylls (colored green) and one carotenoid molecule (colored yellow). See also Table 1.1. A review is available [24].

RC-LH1 Core Complex. Light energy absorbed by LH2 is transported within a few picoseconds to nearby light-harvesting complexes 1 (LH1) [1, 3, 13] as shown in Fig. 1.1. LH1 also absorbs sunlight directly using the same mechanism as LH2, and, actually, has a very similar structure; it is also made of subunits, containing α- and β-proteins, a carotenoid, but only two bacteriochlorophylls (see Table 1.1). LH1 is also ring-like, but forms a wider ring. This ring surrounds another protein complex, the reaction center (RC). Together, the RC-LH1 complex is also termed the photosynthetic core-complex and performs the first processing of the light energy absorbed. Figures 1.3 and 1.4 show the structure of the bacterial photosynthetic core complexes, which exist as a LH1-RC monomer or as a $(\text{LH1-RC})_2$ dimer, depending on the species.

Organization of RC-LH1. We recall that LH2 is a ring-like protein complex, its overall structure being preserved across different bacterial species, but with different numbers (8 or 9) of subunits. LH1 comes in a curious assortment of organizations. In Fig. 1.3, four RC-LH1 arrangements, with the details that are either observed in crystallography [25] or proposed based on electron microscopy [26–30] and atomic force microscopy [31, 32] data, are displayed.

The wide variety of RC-LH1 organization can be classified into two categories: monomeric RC-

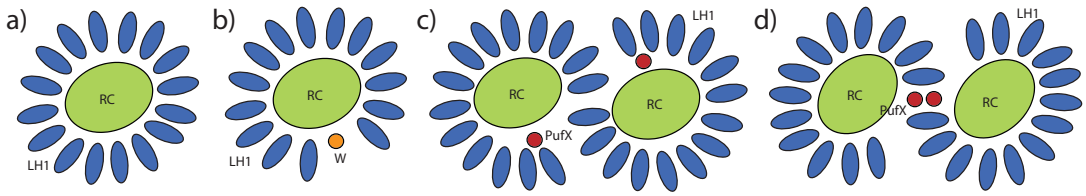

Figure 1.3: Schematics of different organizations of the bacterial photosynthetic core complexes. (a) A core complex in which the LH1 subunits form a complete ring, as seen in *Rhodospirillum rubrum*.[26] See also Fig. 1.4a, b. (b) A core complex in which the LH1 subunits form a ring with a gap, with an extra polypeptide near the gap, as seen in the crystal structure of *Rhodopseudomonas palustris*.[25] (c-d) Two proposed organizations for a dimeric core complex, the dimerization of which requires the extra polypeptide, PufX. (c) is drawn according to the highest structural data for a dimeric core complex, [27] which places PufX near the LH1 openings. See also Fig. 1.4c, d. In (d), PufX is assumed to dimerize and is situated at the symmetry center of the core complex. [31, 32] Dimeric core complexes are seen in certain *Rhodobacter* species, the best-known case being *Rhodobacter sphaeroides* [33].

LH1 and dimeric RC-LH1. For monomeric RC-LH1, the LH1 subunits surrounds the RC, forming a ring. The LH1 ring can either be closed (as in the case of Fig. 1.3a) or interrupted by another protein (as in the case of Fig. 1.3b). Dimeric RC-LH1 is primarily seen for the *Rhodobacter* family of bacteria, although some *Rhodobacter* species have monomeric RC-LH1. [34] For dimeric RC-LH1, an additional protein has been identified, known as the PufX protein. There is no experimentally determined high-resolution structure of a dimeric RC-LH1 yet. Two $(\text{RC-LH1-PufX})_2$ structures have been proposed [27, 29–32, 34–38], their major difference being where PufX is located (Fig. 1.3c and d).

Structures of LH1 and RC. As already pointed out above, the LH1 complex, much like LH2, is an assembly of identical units; each unit comes with two transmembrane α-helices and the pigments sandwiched in between. In Fig. 1.4a, b, an RC-LH1 complex is shown [39]; in Fig. 1.4c, d, a dimeric $(\text{RC-LH1-PufX})_2$ is shown [29, 30]; in Fig. 1.4e, a LH1 subunit is displayed. [39] As can be seen, each LH1 subunit holds two BChls and one Car. LH1 BChls are often referred to as the B875 BChls, as LH1 has a BChl absorption band at $\sim$875 nm; it also has a carotenoid absorption band at 500 nm. Notably, a high-resolution structure for LH1 is yet to be determined, as the only crystal structure of LH1 (Roszak et al., 2003 [25]) does not resolve the terminal ends of LH1. Figure 1.4 actually shows modeled RC-LH1 structures. [29, 30, 39] Given that the α- and β-proteins of LH1 and LH2 have a high degree of sequence identity, [40] the models shown in Fig. 1.3 should be accurate in detail, but may be inaccurate in overall shape.

Unlike in the case of LH1, abundant crystallographic studies have been carried out for the bacterial RC. In 1988, the Nobel Prize in Chemistry was awarded to Deisenhofer, Mitchel and Huber who solved the X-ray structure of a bacterial reaction center. [41] This achievement is extraordinarily

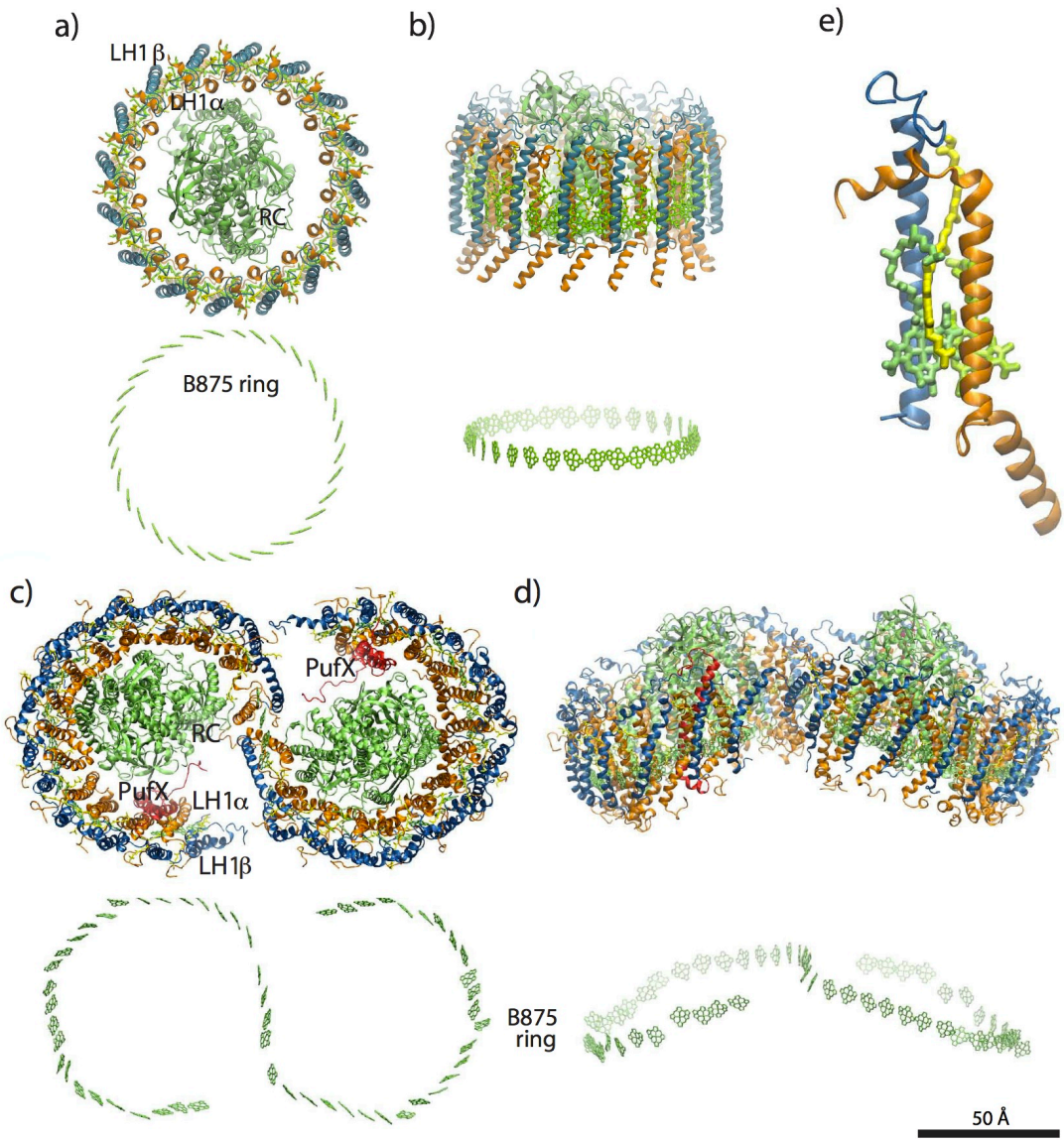

Figure 1.4: (a) Top view of a modeled RC-LH1 core complex, [39] closely resembling that from *Rhodospirillum rubrum*, [26] shown in Fig. 1.3a. (b) Side view of the monomeric core complex model. (c) Top view of a modeled $(\text{RC-LH1-PufX})_2$ dimer [29, 30, 40]; the protein arrangement resembles that of Fig. 1.3c. [27] (d) Side view of the modeled $(\text{RC-LH1-PufX})_2$ dimer; bending of the dimer was observed experimentally through electron microscopy. [28] (e) LH1 subunit consisting of two transmembrane α-helices (the α- and β-proteins), two BChls and one carotenoid; the model shown here is from Ref. (69). The top (a)-(d) shows the whole system, the bottom shows only the B875 BChls.

significant not only in terms of understanding photosynthesis, but also in terms of understanding membrane proteins in general, as the reaction center was the first membrane protein to be crystallized and resolved structurally with atomic resolution. Since then, several crystal structures of the RC for different bacterial species and mutants have been reported. [14, 42, 43]

The photosynthetic reaction center (Fig. 1.5), much like LH2 and LH1, is made of protein and

cofactor components. The protein components of RC consist of three polypeptide subunits: named L, M and H. Subunits L and M both contain five transmembrane helices, while subunit H is a globular domain that caps the RC towards the cytoplasm (Fig. 1.5a). Scaffolded within subunits L and M are the various cofactors found in RC, including four BChl molecules, two bacteriophaeophytin molecules (which are similar to BChl structurally, but do not have a central Mg atom), a carotenoid, and two quinones (labeled Q_A and Q_B) (Fig. 1.5b).

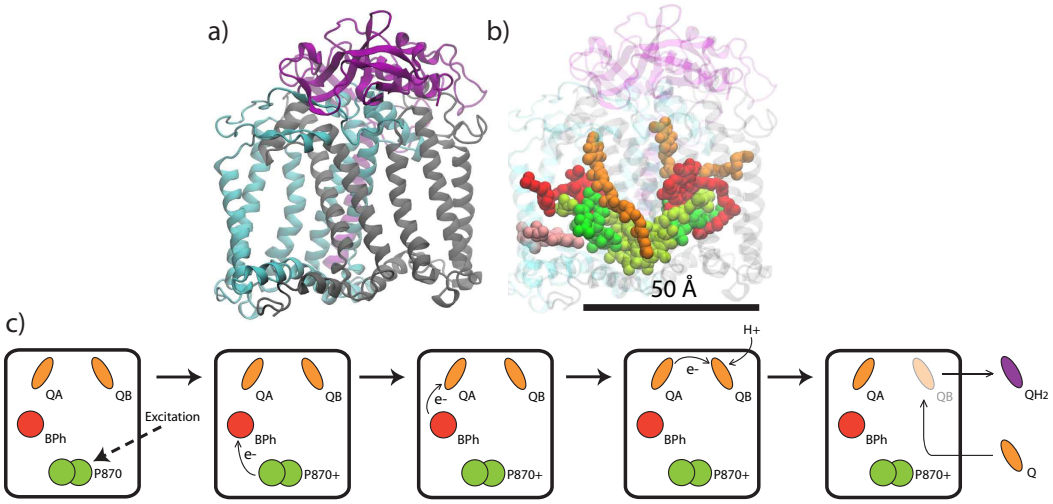

Figure 1.5: Structure and mechanism of the photosynthetic reaction center (RC). (a) The protein components of RC include an H subunit (purple), an M subunit (light blue), and an L subunit (gray). (b) Cofactors in the RC. The four BChls are colored in different shades of green for distinction; the two bacteriopheophytin (BPh) are shown in red; carotenoid is shown in pink; the quinone molecules are shown in orange. (c) A simplified diagram of the energy processing in RC, described in the text; showing only some of the cofactors (omitted are two BChls and one bacteriopheophytin).

The photosynthetic RC utilizes light excitation energy absorbed by the LH1 and LH2 complexes to transfer an electron across the membrane and produce a transmembrane charge difference, i.e., a membrane potential. In Fig. 1.5c the mechanism of RC is outlined (see also Fig. 1.1). Excitation energy from the surrounding LH1 is transfered to the "special pair" BChls in RC (Fig. 1.5c); in *Rhodobacter sphaeroides*, these BChls are known as P870 as they absorb photons of wavelength 870 nm. The excited BChl in the RC transfers an electron to the bacteriopheophytin (BPh) moiety in the RC, which then transfers the electron to Q_A, a quinone. The electron is subsequently delivered to Q_B, which takes on a second electron by repeating the cycle, and is reduced to QH_2. At this point, the QH_2 molecule detaches from the RC and diffuses through the membrane to the Cyt bc_1 complex. Another quinone molecule in the membrane enters the RC to replace Q_B, and the whole process is repeated. The missing electron in one of the special pair BChls is replenished by the protein cytochrome c_2, which shuttles electrons between the Cyt bc_1 complex and the RC. Therefore, the

flow of electrons is cyclic, as shown in Fig. 1. At this point the membrane potential is based on a proton concentration difference between cytoplasm and periplasm.

The theoretical description of excitation dynamics vital to the transfer of photon energy to the reaction center requires the use of advanced theories of quantum dynamics, which is provided by the hierarchy equations of motion (HEOM) [44, 45]. The theory of open quantum systems as well as the HEOM are presented in Chapter 2. These methods are then employed in Chapter 3 to calculate the excitation dynamics in LH2 and examine LH2-LH2 excitation transfer. Chapter 4 presents the results of an investigation where the HEOM is used to address the question of how intra-complex correlated bath fluctuations affects absorption spectra and inter-complex excitation transfer. A consistent set of RC parameters for non-Markovian excitation dynamics is presented in Chapter 5 and then used to investigate LH1-RC excitation transfer. The numerical implementation of the HEOM on parallel shared-memory computers is presented in Chapter 6 and used to examine excitation transfer between LH2 and LH1. Chapter 7 discusses the role that quantum coherence plays in photosynthetic light harvesting.

Chapter 2

Theory

2.1 Introduction

In this chapter the hierarchy equations of motion are introduced as a method for treating the dynamics of a quantum mechanical system embedded in a thermal environment. This method includes dissipative dynamics as well as coherent dynamics in a multi-dimensional system, non-Markovian effects, being often referred to as an "exact" treatment. This chapter serves as an introduction to the methods employed by the calculations in the remaining chapters.

2.2 Open quantum dynamics

Often one is interested in a smaller subsystem S of the total system T, described by the density matrix $\hat{W}(t)$. In this case the dynamics of S only may be obtained by taking the partial trace of $\hat{W}(t)$ to obtain the reduced density matrix

$$\hat{\rho}(t) = \mathrm{tr}_B\{\hat{W}(t)\}, \tag{2.1}$$

where tr_B is the trace over all degrees of freedom not part of S, referred to as the bath B.

Such a case arises when we are only interested in the excitation dynamics of a few pigment molecules that are surrounded by protein, lipids, water, ions, etc.

Hamiltonian. Many systems can be modeled with an effective Hamiltonian [46–48] that describes only a subset of states $|n\rangle$, with energies E_n and interactions V_{nm}, written as

$$H_0 = \sum_n^N E_n |n\rangle \langle n| + \sum_{n,m}^N V_{nm} |n\rangle \langle m| . \tag{2.2}$$

Systems such as those in a biological context are embedded in a thermal environment which can be modeled as an infinite series of harmonic oscillators [49]

$$H_B = \sum_\xi \left[\frac{p_\xi^2}{2m_\xi} + \frac{\omega_\xi^2 q_\xi^2}{2} \right] . \tag{2.3}$$

The thermal bath is coupled to each pigment through the system-bath interaction term

$$H_{SB} = \sum_a^M \hat{F}_a u_a, \tag{2.4}$$

where $u_a = \sum_\xi c_{a\xi}$ and $c_{a\xi}$ is the coupling strength of vibrational mode ξ to the system via operator $\hat{F}_a$. In the case that each pigment is independently coupled to the environment $M = N$ and $\hat{F}_a = |a\rangle \langle a|$. The system-bath coupling introduces a shift in the minimum energy positions of the bath coordinates q_ξ, which can be countered by the renormalization term

$$H_{REN} = \sum_{ab}^M \hat{F}_a \hat{F}_b \sum_\xi \frac{c_{a\xi} c_{b\xi}}{2m_\xi \omega_\xi^2}. \tag{2.5}$$

In the case of independent system-bath coupling for each pigment, the renormalization term reduces to $H_{REN} = \sum_a^N |a\rangle \langle a| \lambda_a$, where $\lambda_a = \sum_\xi c_{a\xi}^2 / 2m_\xi \omega_\xi^2$ is the bath reorganization energy. The total Hamiltonian is thus given by

$$H_T = H_S + H_B + H_{SB}, \tag{2.6}$$

where $H_S = H_0 + H_{REN}$ is the renormalized system Hamiltonian.

The bath degrees of freedom are not of interest and thus are traced out of any dynamics to calculate the bath averaged density matrix evolution as

$$\hat{\rho}(t) \quad = \quad \mathrm{tr}_B \left\{ \int e^{-i\mathcal{L}_T t/\hbar} \hat{\rho}(0) \otimes e^{-\beta H_B} dt \right\} / \mathrm{tr}_B \left\{ e^{-\beta H_B} \right\} = \langle \mathcal{U}(t) \rangle_B \, \hat{\rho}(0), \tag{2.7}$$

where $\beta = 1/k_B T$. Once the thermal average is performed, the influence of the environment enters

only through the bath correlation function given by [50],

$$C_{ab}(t) = \langle u_a(t) u_b(0) \rangle_B = \frac{1}{\pi} \int_{-\infty}^{\infty} d\omega J_{ab}(\omega) \frac{e^{-i\omega t}}{1 - e^{-\beta\hbar\omega}}, \tag{2.8}$$

where the spectral density $J_{ab}(\omega)$ is given by

$$J_{ab}(\omega) = \frac{\pi}{2} \sum_{\xi} \frac{c_{a\xi} c_{b\xi}}{m_\xi \omega_\xi} \delta(\omega - \omega_\xi), \tag{2.9}$$

and is the weighted density of environmental fluctuations. As environmental fluctuations of off-diagonal components in the system Hamiltonian is an order of magnitude smaller than the coupling to diagonal components, i.e. $|C_{ab}| << |C_{aa}|$, they are usually ignored. In this work, only diagonal coupling to the environment is considered.

To obtain a numerically tractable equation of motion from the formal solution, Eq. 2.7, for realistic system sizes is currently only possible using a few different methods [44, 45, 51–54]. The hierarchy equations of motion [44, 45, 54–61] (HEOM) is an attractive method due to its applicability across a broad range of parameters [1, 4, 6, 48, 58, 60, 62–67], despite its computational expense.

Correlation functions. The HEOM arise by exploiting bath correlation functions that decay exponentially in time [44]. This corresponds to employing the spectral density of an over-damped harmonic oscillator, known as the Drude spectral density [50], given by

$$J_{aa}(\omega) = J_a(\omega) = 2\lambda_a \frac{\omega\gamma_a}{(\omega^2 + \gamma_a^2)}, \tag{2.10}$$

where $\lambda_a = \int (J_a(\omega)/\pi\omega)\, d\omega$ is the bath reorganization energy that determines the system-bath interaction strength, and $1/\gamma_a$ is the bath response time. The correlation function associated with the Drude spectral density is [60]

$$C_{aa}(t) = C_a(t) = \sum_{k=0}^{\infty} c_{ak} \exp\left(-\nu_{ak} t\right), \tag{2.11}$$

where $\nu_{a0} = \gamma_a$ and $\nu_{ak\geq 1} = 2\pi k/\beta\hbar$ are the Matsubara frequencies [68] and

$$c_{a0} = \gamma_a \lambda_a \left[\cot(\beta\hbar\gamma_a/2) - i\right] \tag{2.12}$$

$$c_{ak\geq 1} = \frac{4\lambda_a\gamma_a}{\beta\hbar} \frac{\nu_{ak}}{\nu_{ak}^2 - \gamma_a^2}. \tag{2.13}$$

The summation to infinity in Eq. 2.11 needs to be truncated at a finite level, which is achieved by exploiting the approximation that for some finite K, $\nu_{aK}\exp(-\nu_{aK}t) \approx \delta(t)$ [54].

The expansion of the correlation function using Matsubara frequencies, Eqs. 2.11 and 2.13, is not the only possible expansion, and recent work has shown that alternative expansions can yield better results at low K values. [69, 70]

In principle one can also employ correlation functions of the form $C(t) = c\exp(-\gamma t)\cos(\Omega t)$ to derive the HEOM [45, 57], thus enabling the use of arbitrary, multi-peaked spectral densities through a Meier-Tannor decomposition [71]. The oscillation terms in such correlation functions, however, lead to many more terms in the HEOM, such that in practice only Drude spectral densities are employed.

Hierarchy equations of motion. Each exponential term in Eq. 2.11 leads to the introduction of a set of operators called auxiliary density matrices (ADMs) $\hat{\rho}_{\mathbf{n}}$ when deriving the HEOM [45], which are indexed by a vector $\mathbf{n} = (n_{10}, \cdots, n_{1K}, \cdots, n_{M0}, \cdots, n_{MK})$. The equations of motion, which couple the ADMs in a hierarchical structure, are given by [1, 6, 45, 61]

$$\begin{aligned}
\dot{\hat{\rho}}_{\mathbf{n}} &= -\frac{i}{\hbar}\left[\hat{H}_S, \hat{\rho}_{\mathbf{n}}\right] - \sum_{a=1}^{M}\sum_{k=0}^{K} n_{ak}\nu_{ak}\hat{\rho}_{\mathbf{n}} \\
&\quad - \sum_{a=1}^{M}\left(\frac{2\lambda_a}{\beta\hbar^2\gamma_a} - \sum_{k=0}^{K}\frac{c_{ak}}{\hbar\nu_{ak}}\right)\left[\hat{F}_a, \left[\hat{F}_a, \hat{\rho}_{\mathbf{n}}\right]\right] \\
&\quad - i\sum_{a=1}^{M}\left[\hat{F}_a, \sum_{k=0}^{K}\hat{\rho}_{\mathbf{n}_{ak}^{+}}\right] - \frac{i}{\hbar}\sum_{a=1}^{M}\sum_{k=0}^{K} n_{ak}\left(c_{ak}\hat{F}_a\hat{\rho}_{\mathbf{n}_{ak}^{-}} - \hat{\rho}_{\mathbf{n}_{ak}^{-}}\hat{F}_a c_{ak}^{*}\right).
\end{aligned} \tag{2.14}$$

Each ADM with index $\mathbf{n}$ is coupled to ADMs with indices $\mathbf{n}_{ak}^{\pm} = (n_{10}, \cdots, n_{ak} \pm 1, \cdots, n_{MK})$. Any ADM with a negative value for any n_{ak} is automatically set to zero. The system density matrix $\hat{\rho}$ is exactly the density matrix with index vector $\mathbf{n} = 0$. Each density matrix in the hierarchy is assigned to a hierarchy level $L = \sum_{a=1}^{M}\sum_{k=0}^{K} n_{ak}$. The coupling of the HEOM leads to a structure that can be visualized as a Pascal's $d-$simplex, where $d = M(K+1)$. Example hierarchies for $d = 2$, 3 and 4 are shown in Fig. 2.1.

The number of matrices rapidly increase with hierarchy level L (Fig. 2.2) and are in principle infinite. The ADMs account for the non-Markovian extent of the dynamics, meaning that more ADMs are needed to capture dynamics with greater non-Markovian character. Due to this behavior, however, a natural truncation L_T can be chosen such that $L_T \min_{ak}(\nu_{ak}) \gg \omega_{\max}$, where $\omega_{\max}$ is the maximum oscillation frequency in the system, without compromising the dynamics [45]. Employing

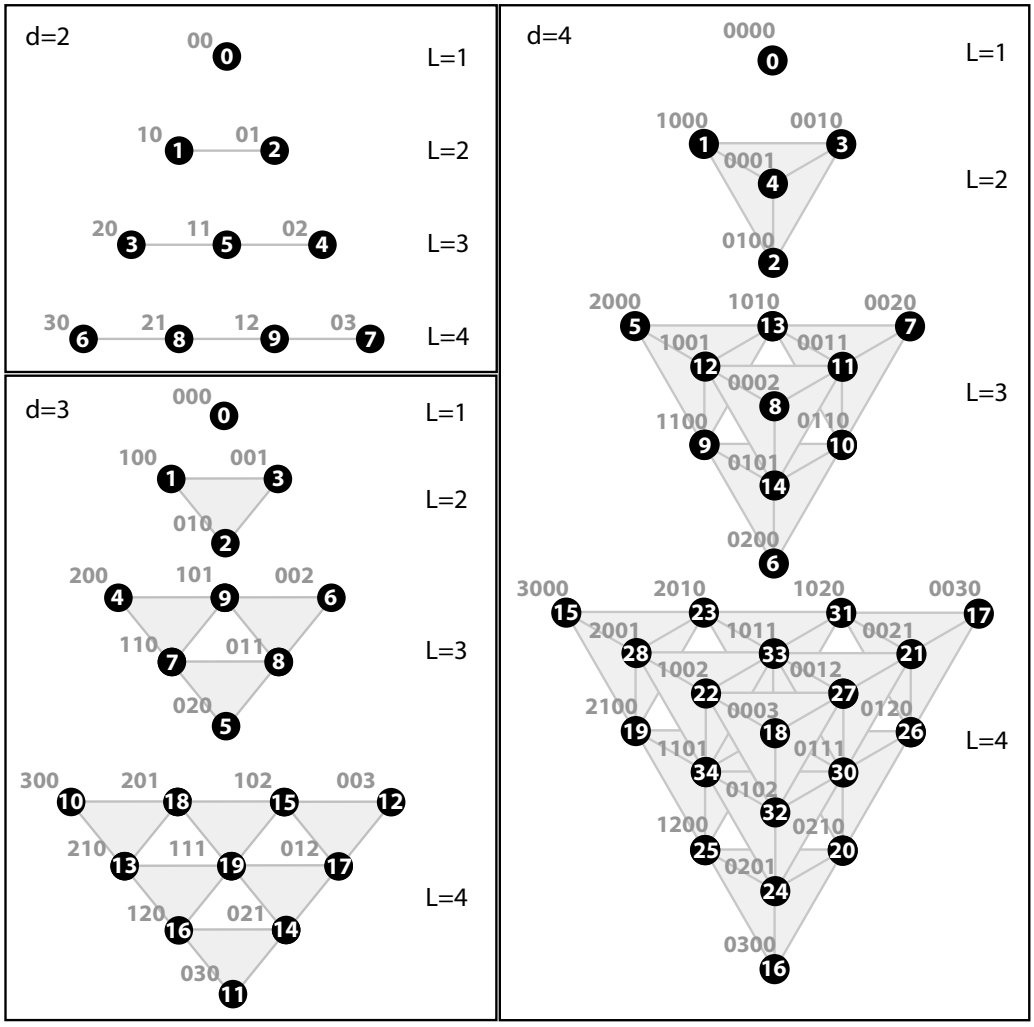

Figure 2.1: The first 4 hierarchy levels of Pascal's $d-$simplices for $d = M(K+1) = 2$, 3, and 4. Each circle corresponds to a single ADM with the corresponding index vectors $\mathbf{n}$ shown in blue text. The numbering inside the circles corresponds to the scheme described in the hierarchy generation algorithm in Listing 1. The shaded regions indicate which ADMs are at the same level. Connectivity of the ADMs to those in the levels above and below is not shown.

such truncation is often unfeasible due to computational limitations, and thus convergence should be carefully checked for each system with feasible values of L_T.

Having chosen a truncation level L_T, the manner by which the HEOM is cut-off must also be specified. There are two ways to truncate the HEOM, either with so-called time non-local (TNL) truncation that sets all ADMs in levels L_T or greater to zero [45], or by so-called time-local (TL) truncation that employs the Markovian approximation for ADMs in level L_T [57, 58, 61]. By

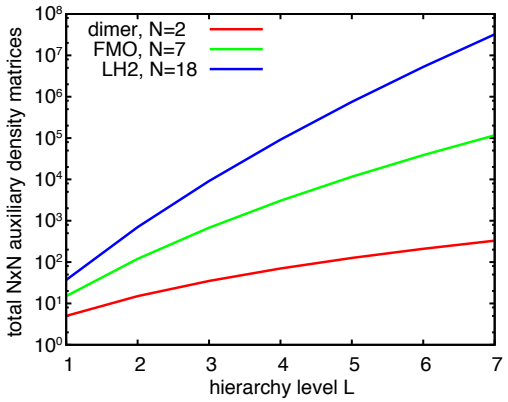

Figure 2.2: Total number of ADMs with increasing hierarchy level L_T for a pigment dimer, the Fenna-Mathews-Olson (FMO) complex and for Light-Harvesting complex 2 (LH2).

employing the Markovian approximation, it is assumed that for all ADMs with $L = L_T - 1$

$$\sum_{k=0}^{K} \hat{\rho}_{\mathbf{n}^+_{ak}} \approx -i \left(\hat{Q}_a^K(t) \rho_{\mathbf{n}} - \rho_{\mathbf{n}} \hat{Q}_a^K(t)^\dagger \right), \tag{2.15}$$

where

$$\hat{Q}_a^K(t) = \int_0^t \left(\sum_{k=0}^{K} c_{ak} \exp\left(-\nu_{ak}\tau\right) \right) \exp\left(-\frac{i}{\hbar} H_S \, \tau \right) \hat{F}_a \exp\left(\frac{i}{\hbar} H_S \, \tau \right) d\tau. \tag{2.16}$$

It has been shown that TNL truncation produces spurious peaks in absorption spectra [58, 61] and thus TL truncation should be employed whenever possible.

Static disorder. The total Hamiltonian H_T, stated in Equation (2.6), describes in principle all possible influences of the thermal bath on the system. However, the ensemble average over the spectral density in Equation (2.10) assumes that the system dynamics is slower than the thermal fluctuations. This precludes the proper description of long time fluctuations that can arise from large scale deformations of the protein complex.

To take the unaccounted for disorder (often termed "static" disorder) into account the excited state energy levels are taken to be Gaussian distributed with means E_n and widths σ_n for each pigment n [1, 61, 72–75]. Thus to include static disorder, one replaces E_n by $E_n + \delta E_n$ where δE_n is drawn from a Gaussian distribution with zero mean and standard root mean squared deviation σ_n.

2.3 Linear spectra

The linear absorption is calculated by explicitly including the ground state in the system Hamiltonian, such that Eq. 2.2 then reads $\hat{H}_0 = \hat{H}_g + \hat{H}_e$ where

$$\hat{H}_g = E_0 \left|0\right\rangle \left\langle 0\right| \tag{2.17}$$

$$\hat{H}_e = \sum_{n=1}^{N} E_n \left|n\right\rangle \left\langle n\right| + \sum_{n,m=1}^{N} V_{nm} \left|n\right\rangle \left\langle m\right|, \tag{2.18}$$

where the ground state energy E_0 is set to 0. Excitation of the system is introduced with the excitation operator

$$\hat{\boldsymbol{\mu}}_+ = \sum_{n=1}^{N} \mathbf{d}_n \left|n\right\rangle \left\langle 0\right|, \tag{2.19}$$

where $\mathbf{d}_n$ is the transition dipole moment of state $|n\rangle$. Conversely, the excitation in the system is measured with the de-excitation operator

$$\hat{\boldsymbol{\mu}}_- = \sum_{n=1}^{N} \mathbf{d}_n \left|0\right\rangle \left\langle n\right|. \tag{2.20}$$

Absorption. In case of absorption spectra the system is initially in the ground state $\hat{\rho}_g = |0\rangle \langle 0|$. It is subsequently excited by a non-polarized light source to give the initial state for absorption calculation

$$\hat{\boldsymbol{\mu}}_A(0) = \hat{\boldsymbol{\mu}}_+ \hat{\rho}_g = \sum_{n=1}^{N} \mathbf{d}_n \left|n\right\rangle \left\langle 0\right|. \tag{2.21}$$

The initial state is then propagated to a time t

$$\hat{\boldsymbol{\mu}}_A(t) = \langle \mathcal{U}(t) \rangle_B \ \hat{\boldsymbol{\mu}}_A(0), \tag{2.22}$$

prior to measurement with the de-excitation operator $\boldsymbol{\mu}_-$. Equilibrium absorption spectra can be calculated by the dipole autocorrelation coefficient. In the site-basis the equation for the absorption spectrum reads [76]

$$A(\omega) \propto \mathrm{Re} \int_0^\infty e^{i\omega t} \ \mathrm{tr} \left\{ \boldsymbol{\mu}_- \cdot \boldsymbol{\mu}_A(t) \right\} dt, \tag{2.23}$$

Calculating the absorption spectrum thus amounts to calculating three independent density matrix evolutions with the initial states given by the x, y and z components of the transition dipole moments

$\mathbf{d}_n$.

Emission. In case of emission spectra the system is initially in the equilibrium excited state

$$\hat{\rho}_e = \sum_{n,m=1}^{N} \rho_{e,nm} \left|n\right\rangle \left\langle m\right|, \tag{2.24}$$

such that $\partial_t \hat{\rho}_e = 0$. It is subsequently de-excited by a non-polarized light source to give the initial state for emission calculation

$$\hat{\boldsymbol{\mu}}_E(0) = \hat{\boldsymbol{\mu}}_- \hat{\rho}_e = \sum_{n=1}^{N} \mathbf{d}_n \sum_{m=1}^{N} \rho_{e,nm} \left|0\right\rangle \left\langle m\right|. \tag{2.25}$$

The initial state is then propagated to a time t

$$\hat{\boldsymbol{\mu}}_E(t) = \left\langle \mathcal{U}(t) \right\rangle_B \ \hat{\boldsymbol{\mu}}_E(0), \tag{2.26}$$

prior to measurement with the excitation operator $\boldsymbol{\mu}_+$. In the site-basis the equation for the emission spectrum reads [76]

$$E(\omega) \quad \propto \quad \mathrm{Re} \int_0^\infty e^{-i\omega t} \ \mathrm{tr} \left\{ \boldsymbol{\mu}_+ \cdot \boldsymbol{\mu}_E(t) \right\} dt, \tag{2.27}$$

For both absorption and emission spectra the propagation of the transition dipole operator $\hat{\boldsymbol{\mu}}_{A/E}(t)$ can be performed with the HEOM. Furthermore, only the propagation of a length N vector needs to be performed, as the ground state energy is set to zero, and is thus computationally cheaper than the propagation of a full density matrix.

The HEOM are employed in the following chapters to investigate excitation dynamics in the light harvesting complexes of purple bacteria. The next chapter presents the investigation excitation dynamics and transfer in light harvesting complex 2.

Chapter 3

Excitation dynamics of light harvesting complex 2

3.1 Introduction

The light harvesting proteins of the purple bacteria chromatophore include light harvesting complex 1 (LH1), light harvesting complex 2 (LH2) and RC complexes (shown in Fig. 3.1). The chromatophore of *Rhodobacter sphaeroides* consists of pools of LH2 complexes that surround dimeric LH1-RC core complexes [13]. LH2 is the primary antenna complex of the chromatophore, not only due to its relative abundance, but also because of its large absorption cross-section [77]. The carotenoid (Car) and bacteriochlorophyll (BChl) molecules in the antenna complexes are the pigments responsible for the absorption of light and subsequent excitation transfer events [78–80]. On initial absorption of light by the pigments of an LH2, the excitation energy is passed between LH2, LH1 and RC complexes. At the RC, the energy is used for charge separation, thus forming an electrical gradient across the membrane and initiating the next, more stable, phase in photosynthetic energy trapping [81].

Prior theoretical investigations of the excitation dynamics of LH2 used Redfield and Förster theories [82–86] and compared results with spectroscopic measurements. Redfield theory describes the excitation dynamics of a system where the environment coupling is significantly weaker than the coupling between pigments. Förster theory is used to calculate the transfer rate between pigments that are strongly coupled to the environment, but are weakly coupled to each other [87, 88]. The conclusion has been drawn that due to the coherence between nearby BChls, Förster theory cannot account for the excitation dynamics within a B850 ring [87, 89–91]. It has been suggested also recently that Redfield theory cannot adequately describe the coherence dynamics in quantum systems [64] thus neither description may be sufficient to describe the excitation dynamics of LH2.

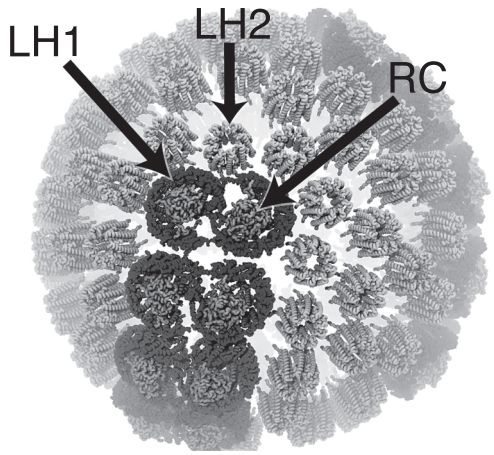

Figure 3.1: Patch of the chromatophore from purple photosynthetic bacteria *Rhodobacter sphaeroides* showing the placement of LH2 and LH1-RC complexes as determined from atomic force microscopy and computational modelling [13]. Pools of LH2 antenna complexes are seen to surround the LH1-RC core complexes; lipids are not shown. As the primary antennae of the chromatophore most of the inter-complex excitation transfer occurs between LH2s.

The coupling between BChls of different light harvesting complexes is much weaker than the coupling to the environment. Förster theory thus provides am accurate description for the inter-complex transfer rates and overall quantum efficiencies of chromatophores [13, 19]. An important assumption is that the timescale of the intra-ring thermal relaxation is sufficiently short to assume it to be instantaneous in comparison with inter-ring excitation transfer. This implies that excitation transfer between LH2 rings arises from Boltzmann-weighted intra-ring exciton states, an assumption which underlies the generalized Förster transfer theory [92].

An accurate description of the overall excitation dynamics in LH2 requires that the environment and both the intra-ring and inter-ring couplings be treated non-perturbatively. In recent years a description of quantum dynamics in a noisy environment has been derived to arbitrary order in system-environment coupling by utilizing a hierarchy of auxiliary density matrices [44, 45]. This method has been used to study the coherence dynamics in the Fenna-Matthews-Olsen pigment-protein complex of green sulphur bacteria [48]. The present study is, to the best of the author's knowledge, the first application of the hierarchical equations of motion to a system as large as two B850 rings. It is the aim of the present study to explore the intra- and inter-ring excitation dynamics of the B850 ring and to investigate the assumptions underlying generalized Förster theory.

In Section 3.2 the theoretical description of the system as well as that of generalized Förster theory is given. Section 3.3 presents the excitation dynamics of a single B850 ring with initial states corresponding to a singly excited BChl and to an 850 nm delocalized state. Section 3.3 also includes

the results of the investigation of excitation transfer between two B850 rings.

3.2 Model of B850 pigments in LH2

The B850 ring is the system of interest and is described by the Hamiltonian

$$H_0 = \sum_{i=1}^{N} E_i \left|i\right\rangle \left\langle i\right| + \sum_{i=1}^{N}\sum_{j=1}^{N} V_{ij} \left|i\right\rangle \left\langle j\right|, \tag{3.1}$$

where $|i\rangle$ represents a localized excitation on BChl i, E_i is the Q_Y excitation energy, and the electronic coupling between excited states is given by V_{ij}. The system Hamiltonian H_0 can be diagonalized to give the exciton spectrum ϵ_ν and associated exciton states $|\widetilde{\epsilon_\nu}\rangle = \sum_i C_\nu^i |i\rangle$.

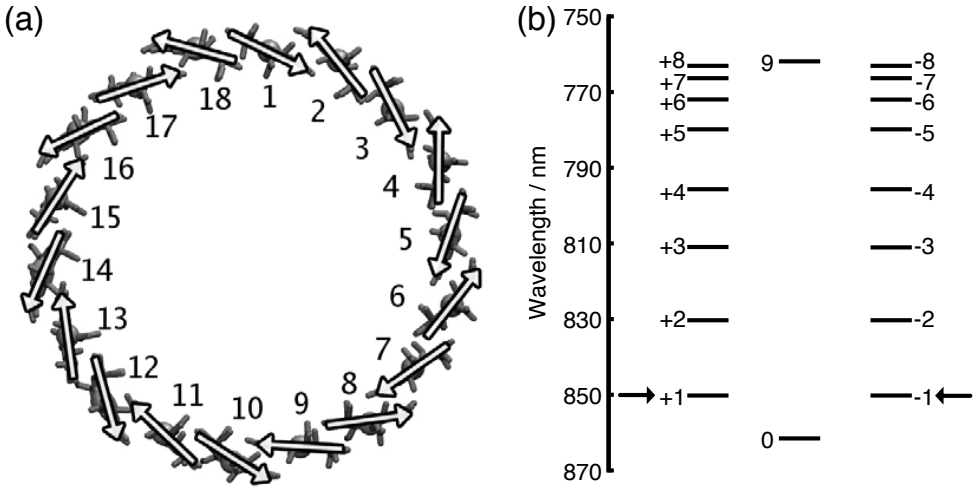

Figure 3.2: (a) B850 ring showing the alternating transition dipole moment orientations giving rise to the 9-fold symmetry. The arrows placed over the Mg atoms show the transition dipole moments from the N_B atom to the N_D atom of each BChl [19]. (b) Exciton spectrum of B850 shown with the familiar k-labels [93]. The arrows indicate the two states with the highest oscillator strength, the so-called 850 nm states.

The B850 ring contains BChls ($N = 18$) that are dimerized to give it a nine-fold symmetry as shown in Fig. 3.2a. The interactions within a dimer and between two dimers thus specify all the nearest neighbor entries in H_0. Due to their close proximity, electrostatic interaction alone cannot account for the nearest neighbor BChl couplings.

Quantum chemistry calculations suggest the coupling V_{ij} between neighboring BChls in a dimer, e.g. V_{12}, as 363 cm^{-1} and between dimers, e.g. V_{23}, as 320 cm^{-1} [13, 94]. The electrostatic environment in the dimer causes the Q_Y excited states of each BChl to be shifted; alternating site energies E_j of 12457.66 cm^{-1} and 12653.66 cm^{-1} reproduce the 850 nm absorption peak in the

exciton spectrum [81]. The non-nearest neighbor couplings V_{jk} are calculated using the induced dipole-induced dipole interaction

$$V_{ij} = C\frac{\mathbf{d}_i \cdot \mathbf{d}_j - 3\left(\mathbf{d}_i \cdot \hat{\mathbf{r}}_{ij}\right)\left(\mathbf{d}_j \cdot \hat{\mathbf{r}}_{ij}\right)}{\left|\mathbf{r}_{ij}\right|^3}. \tag{3.2}$$

The coupling constant $C = 348000$ Å^{3}cm^{-1} is chosen to reproduce the LH2 exciton spectrum shown in Fig. 3.2b [13]. The exciton spectrum consists of 8 degenerate states labeled with quantum numbers $k = \pm 1, \pm 2, \cdots, \pm 8$, and two non-degenerate states $k = 0$ and $k = 9$, the lowest and highest energy states respectively. States $k = \pm 1$, the so-called 850 nm states, contain 89% of the total oscillator strength and produce the 850 nm peak in the absorption spectrum.

Generalized Förster theory calculates the transfer rate between state $|\tilde{\epsilon}_\nu\rangle$ of donor ring D to state $|\tilde{\epsilon}_\mu\rangle$ of acceptor ring A as ($\beta = 1/k_B T$) [95]

$$K_{\mu\nu} = \frac{2\pi}{\hbar}\frac{\exp\left(-\beta\epsilon_\nu\right)}{\sum_\alpha \exp\left(-\beta\epsilon_\alpha\right)}\sum_{i=1}^{N_D}\sum_{j=1}^{N_A} V_{ij}^2 \left|C_\nu^i\right|^2 \left|C_\mu^i\right|^2 J_{DA}^{\nu\mu}, \tag{3.3}$$

The spectral overlap $J_{DA}^{\nu\mu}$ between the donor state $|\tilde{\epsilon}_\nu\rangle$ and the acceptor state $|\tilde{\epsilon}_\mu\rangle$ is

$$J_{DA}^{\nu\mu} = \int dE S_D^\nu(E) S_A^\mu(E), \tag{3.4}$$

for the normalized donor and acceptor spectral line shapes $S_D^\nu(E)$ and $S_A^\mu(E)$. The total transfer rate between the donor and acceptor is calculated as the sum over all states, $K = \sum_\nu \sum_\mu K_{\nu\mu}$.

The bath parameters required to model excitation dynamics in the B850 ring using Drude spectral density (Eq. 2.10) are the bath response time $1/\gamma_j$ and the reorganization energy λ_j. In general, these are site dependent but due to the symmetry and relative homogeneity within the ring we set $1/\gamma_j = 1/\gamma = 100$ fs and $\lambda_j = \lambda = 200$ cm^{-1} to match parameters determined from fits to spectroscopic data [96, 97].

Fourth order Runga-Kutta numerical integration with a 1 fs time-step was used to integrate the hierarchical equations of motion, Eq. 2.14. For one B850 ring (18 BChls) using an eighth order system bath coupling ($L_T = 5$) and two temperature correction terms, 424 270 matrices are required. Using double precision, this requires 12.3 Gb of memory. Two B850 rings with the same number of temperature correction terms and system-bath coupling uses 6 210 820 matrices (720 Gb memory). With a sixth order system-bath coupling ($L_T = 4$) the number of matrices is reduced to 221 815 (26 Gb memory).

3.3 Results

Dynamics of a single B850 ring. Two simulations of the density matrix were performed for a single B850 ring at a temperature of 300K. The first was done with the initial state consisting of only a single excited BChl ($\rho_0 = |1\rangle\langle 1|$) and the second with the initial state given by the 850 nm ($k = +1$) state ($\rho_0 = |\widetilde{\epsilon_2}\rangle\langle\widetilde{\epsilon_2}|$). The coherence length of the system was computed at each time step as the inverse participation ratio, defined by[98]

$$L_\rho = \frac{1}{N}\frac{\left(\sum_{i,j}|\rho_{ij}|\right)^2}{\sum_{i,j}|\rho_{ij}|^2}. \tag{3.5}$$

The site dynamics, depicted in Fig. 3.3a, shows the dissipation of the excitation across all sites from a single initially populated site. The strong coupling between neighboring sites is reflected in the very fast population transfer between them. This is indicated by the rapid increase of BChl 2 population in Fig. 3.3a. Excitation extends rapidly to neighboring sites. The transfer to neighboring sites occurs in less than 15 fs and transfer across half the ring occurs in about 65 fs.

The dissipation of the initial state, such that the site populations converge to their steady-state values, happens in about 0.4 ps. At the steady state the excitation is completely delocalized around the ring. The alternate Q_Y energies within the dimer cause alternating steady state populations of 0.067 and 0.044 such that the total steady-state population of each dimer is 1/9.

The time evolution of the coherence length L_ρ (Fig. 3.3b) presents, as a single quantity, the timescales present in the dynamics of all the coherence terms in the density matrix. The initial coherence length is 1 since initially only a single BChl is occupied. The fast inter-site excitation dynamics is reflected in the rapid fluctuation of the coherence length up to ~ 0.2 ps. After 0.4 ps, once the site populations have reached their steady state values, the coherence terms are still building up to converge to their steady state values in about 1 ps. The final coherence length $L_\rho = 11.2$ is very close to the coherence length calculated for Boltzmann populated exciton states, namely $L_\rho = 11.4$.

The population of exciton state $|\widetilde{\epsilon_\nu}\rangle$ is calculated using $P_\nu(t) = \langle\widetilde{\epsilon_\nu}|\,\rho(t)\,|\widetilde{\epsilon_\nu}\rangle$. Figures 3.3c and 3.3d show the evolution of the exciton states from the initial state $\rho(0) = |\widetilde{\epsilon_2}\rangle\langle\widetilde{\epsilon_2}|$. All states, but the initially excited state and the ground state, converge to their steady state values in 0.2 ps. The ground state and initially excited state converge to their steady state populations on a longer timescale of about 0.8 ps. These timescales match the times seen in Figs. 3.3a and 3.3b for the fast population transfer and the longer build-up of the coherence. Similar bi-exponential timescales are

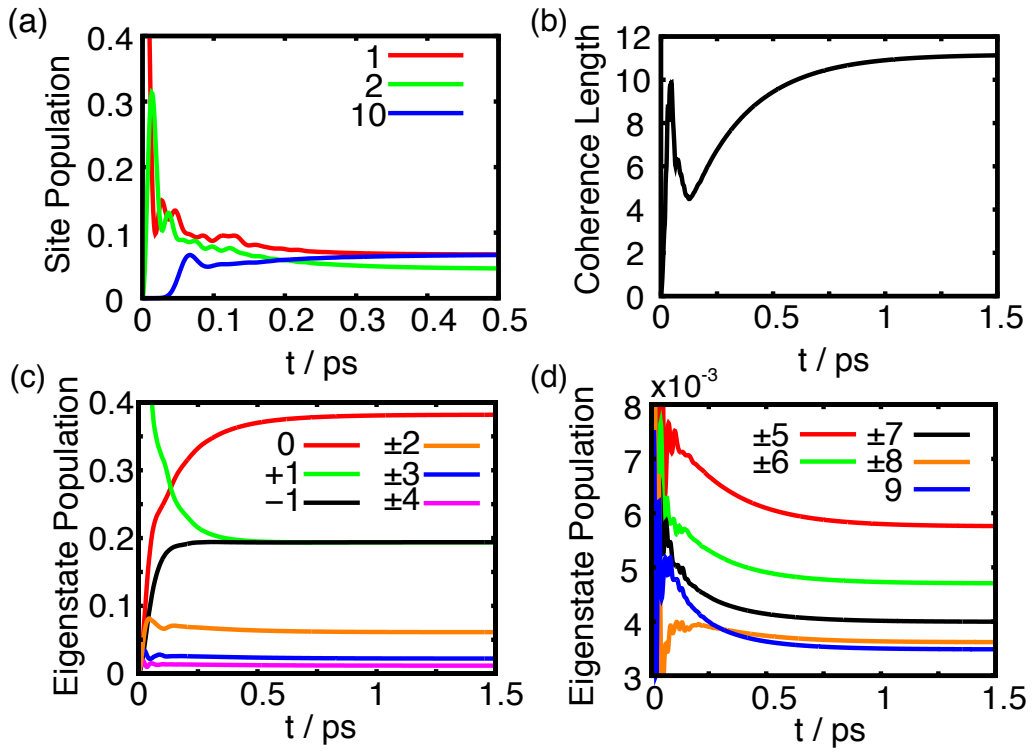

Figure 3.3: (a) Population dynamics of BChls 1, 2 and 10 starting from $\rho_0 = |1\rangle\langle 1|$. The transfer of excitation across half the ring takes about 65 fs. The difference between neighboring BChl populations is seen by the steady state difference of BChls 1 and 2 and is due to the alternating site energies in the Hamiltonian. (b) Time evolution of the coherence length in the B850 ring as measured by the inverse participation ratio starting from $\rho_0 = |1\rangle\langle 1|$. The coherence length converges to $L_\rho = 11.2$. (c) Time evolution of the 9 lowest energy exciton states with $\rho(0) = |\widetilde{\epsilon_2}\rangle\langle\widetilde{\epsilon_2}|$. (d) Time evolution of the 9 highest energy exciton states starting from $\rho(0) = |\widetilde{\epsilon_2}\rangle\langle\widetilde{\epsilon_2}|$.

noted in spectroscopic experiments for LH2 [82, 85, 99, 100] as well as LH1 [101, 102].

The steady-state populations at $t = 5$ ps are shown in Fig. 3.4 along with the populations expected from Boltzmann distributed exciton states. The lowest-lying exciton states, particularly states $k = \pm 1, \pm 2$, assume populations that are close to Boltzmann weights and the overall distribution resembles a Boltzmann distribution. The same steady state is reached independently of the chosen initial state.

To test for convergence, the excitation dynamics of the B850 ring was also calculated using lower L_T values and fewer Matsubara terms. Using a value of $L_T = 2$ (time-nonlocal formalism) we found that the inter-site transfer times were identical; however, the exciton populations' relaxation times were longer and the density matrix did not remain positive definite. With a cut-off of $L_T = 4$ the times for inter-site transfer and exciton relaxation were very close to those seen with $L_T = 5$. The relative difference between the exciton steady state populations with $L_T = 4$ compared to $L_T = 5$ was 0.3% which indicates reasonable convergence with respect to the hierarchy truncation level.

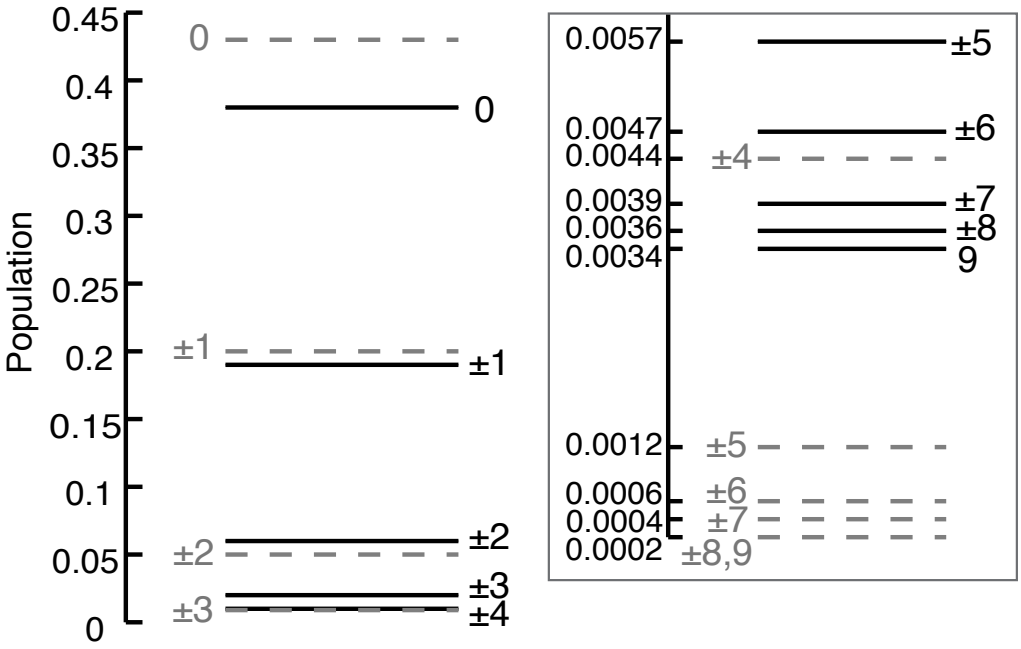

Figure 3.4: Steady state populations (solid lines) and Boltzmann populations (dashed lines) of the exciton states of LH2 B850. The inset shows the exciton populations of the highest energy states. The state labels on the left of the lines denote the Boltzmann populated states and the labels on the right denote the steady state populations.

The inclusion of the temperature correction terms to the formalism greatly enhances convergence with respect to the number of Matsubara terms required. The maximum relative difference for the exciton populations between including only 1 Matsubara term and 2 terms is 0.7%, indicating reasonable convergence with respect to the number of included Matsubara terms.

Dynamics of two B850 rings. The calculation of the excitation dynamics was repeated for two B850 rings (36 sites in total) at 300K. The rings were placed 85 Å apart (center-to-center distance), which corresponds to steric contact of the two LH2 proteins holding the B850 rings. The initial state was set to the $k = +1$ state on the donor ring $\rho(0) = |\epsilon_2\rangle \langle\epsilon_2|$. The dynamics on the donor ring closely echoed what is seen in Figs. 3.3c and 3.3d. In the time it takes to reach the steady-state for a single ring, 10% of the total population is transfered to the acceptor ring. Shown in Fig. 3.5 is the transfer of population from the donor to the acceptor ring. The population transfer from the donor follows a single exponential decay with a decay time of 9.1 ps towards equal donor and acceptor population. Figure 3.5 indicates that the transfer between rings is incoherent and can be described by the kinetic equation

$$\partial_t P = -kP + k\,(1 - P)\,, \tag{3.6}$$

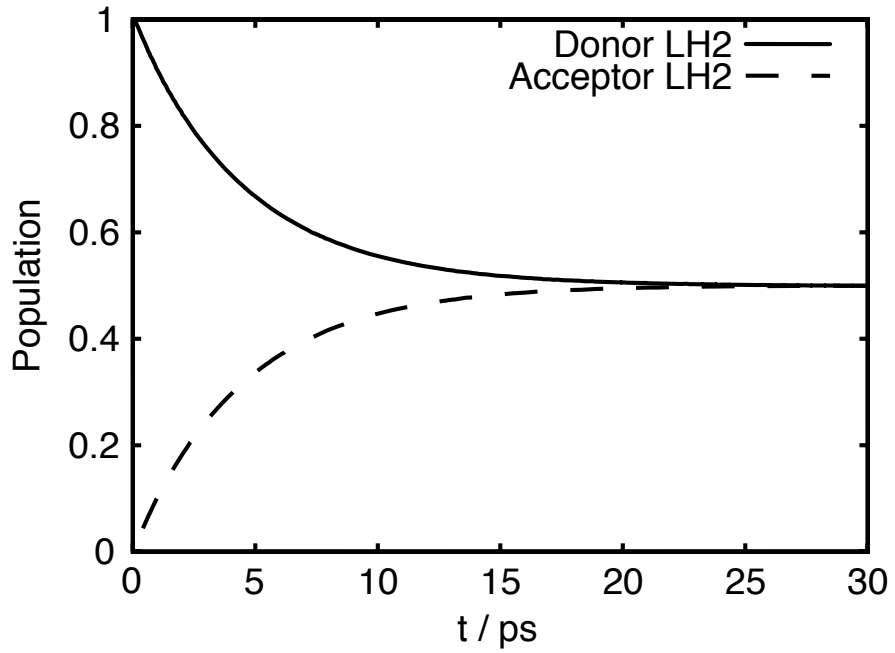

Figure 3.5: Transfer of excitation from donor to acceptor ring, showing single exponential decrease (increase) for the donor (acceptor). The transfer time is 9.1 ps, the transfer time resulting from the generalized Förster calculation is 10.2 ps.

where P is the population of the donor ring. This implies that the inter-complex transfer rate can be accurately calculated using the generalized Förster formalism. Using generalized Förster theory the LH2 to LH2 transfer time is calculated to be 10.2 ps. If the near Boltzmann exciton populations shown in Fig. 3.4 are used instead of Boltzmann populated exciton states, the transfer time is calculated to be 9.5 ps. The remaining difference between the transfer rates is less than the intra-ring relaxation time of ≈ 1 ps. Both results correspond well with the ps scale transfer time measured experimentally [103].

In the calculations using the hierarchy method, not all sources of thermal noise have been taken into account. One such source arises in the protein environment from so-called static disorder [72, 104] due to protein structural dynamics that occur on a timescale much longer than the excitation dynamics. The static disorder is responsible for the inhomogeneous line-broadening in the fluorescence spectra [105], but is computationally expensive to take into account in the hierarchy method. However, the effect of static disorder can easily be taken into account in the generalized Förster formalism; adding Gaussian diagonal disorder with $\sigma = 200$ cm^{-1} increases the transfer

time by 2.2 ps (18%) from the non-disordered calculation, namely to 12.4 ps.

The super-radiance effect of some of the exciton states ($k = 0, \pm 1$) has been shown to be enhanced by the spectral broadening from homogeneous and inhomogeneous disorder [72, 97]. The exciton transfer between complexes is, however, not solely dependent on the oscillator strengths of the exciton states (which characterize the super-radiance effect), but also on the inter-complex couplings, the exciton state populations and the spectral overlap.

Since we have shown that the assumption of Boltzmann-distributed donor states is a reasonable approximation, we can proceed with a further investigation of the primary contributions to the inter-complex transfer rate whilst taking static disorder into account using generalized Förster theory [75, 106–108]. When disorder is introduced, it is not clear, in general, whether the character of individual exciton states of the averaged complex is conserved. However, for the typical disorder seen in LH2 one can still identify the shifted exciton states through their character seen without disorder. Indeed, Fig. 3.6 demonstrates that the exciton states retain their labelling with the inclusion of disorder [93, 97].

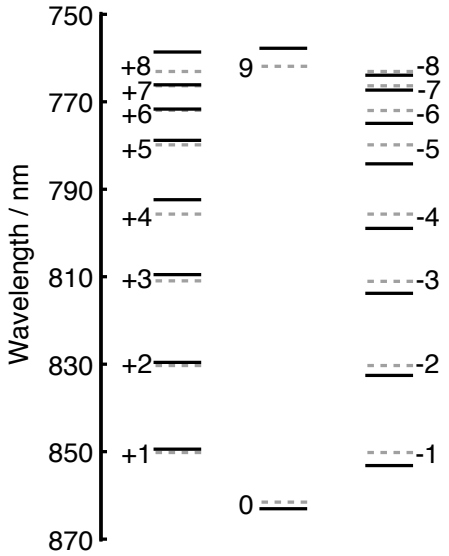

Figure 3.6: Distortion of B850 exciton states due to Gaussian diagonal disorder. The dashed lines correspond to the exciton spectrum of the averaged B850 ring showing the degeneracy for all the states with the exception of the $k = 0$ and $k = 9$ states. The solid lines show the exciton spectrum of a single realization of Gaussian diagonal disorder with a width $\sigma = 200$ cm^{-1}. With the inclusion of disorder, the degeneracies are lifted, yet the exciton states of the disordered Hamiltonian can be linked to those of the ideal Hamiltonian (c.f. Fig. 3.2b).

Table 3.1 lists the individual transfer rates of the disordered systems. The five lowest energy exciton states contain 98% of the total transfer rate. The states with the highest oscillator strength, have 39% of the total exciton population and contribute 69% of the total transfer rate with the

inclusion of disorder. The remaining three states, labeled by $k = 0, +2, -2$, each contribute 8%,12% and 8%, respectively. As would be expected, the degeneracy in the exciton states is lifted with the inclusion of disorder, which is clearly shown through the different Boltzmann populations of the $k = \pm 1$ and $k = \pm 2$ states.

Table 3.1: Boltzmann populations of the exciton states of a B850 ring along with the transfer rates from these states to another B850 ring, averaged over 10 000 realizations of diagonal disorder.

State	Boltzmann Population	Transfer Rate (ps^{-1})	% of Total Rate
0	0.47	1/161	8
+1	0.23	1/35	36
-1	0.16	1/38	33
+2	0.06	1/102	12
-2	0.04	1/145	9
+3	0.01	1/807	1
-3	0.01	1/1244	1
Total	1	1/12.4	100

3.4 Discussion

The excitation dynamics within one B850 ring of LH2 and between two B850 rings have been computed using the hierarchical equations of motion [54] for a quantum system in contact with a thermal bath. Within one B850 ring two timescales for the excitation dynamics were observed, 0.2 ps and 1 ps, corresponding to the relaxation of site populations and coherence terms, respectively. It was shown that the relaxation within a single B850 ring happens on a much faster timescale ($\sim$ 1 ps) compared to the excitation transfer timescale ($\sim$ 10 ps) between two B850 rings. Excitation transfer between two rings exhibits single exponential kinetics, indicating incoherent transfer. This substantiates that generalized Förster theory provides an accurate description of exciton migration between complexes and can furnish quantitative predictions of excitation transfer rates between light harvesting complexes.

The effect of static disorder on the intra-ring excitation dynamics could not be characterized in the framework of the hierarchy calculations. Previous work accounted for intra-ring excitation dynamics including static disorder using Redfield theory. In this case transfer rate across half the ring for LH2 range between 100 and 350 fs for different realizations of disorder [74, 85]. The comparison of these times with those determined here (c.f. Fig. 3.3a) provides a good indication of the effect of

static disorder on the intra-ring excitation dynamics.

The inclusion of static disorder on transfer between B850 rings was investigated employing generalized Förster theory. Diagonal static disorder increased the transfer time by only 2.2 ps, indicating an inherent accommodation of disorder that is to be expected in robust biological systems. It was found that the five lowest lying exciton states are responsible for 98% of the energy transfer between rings. The primary contributors are the $k = \pm 1$ states due to their high oscillator strength; however, $k = 0, \pm 2$ states make non-negligible contributions to the total transfer rate. This has been noted previously and is due to the exciton populations of the $k = 0, \pm 2$ and the mixing of these states with the $k = \pm 1$ states [109].

Freiberg et al. [97] have shown that the thermal baths of BChls in the B850 ring may be correlated. The investigation into effect of correlated bath modes between BChls is presented in the following Chapter.

Chapter 4

Effect of correlated bath fluctuations on exciton transfer

4.1 Introduction

Excitation transfer plays a fundamental role in photosynthetic organisms [15, 16].

While photosynthetic systems have been studied extensively, many questions in relation to excitation transfer in biological contexts remain to be fully addressed [1, 3, 48, 98, 110].

Developing a theory of excitation transfer and dynamics that correctly takes environmental effects into account has been a topic of great interest for many years [44, 87, 89, 90, 107, 111–115].

In the last two decades computational power and theoretical developments have made it possible to include more detail and make fewer assumptions when modeling photosynthetic light harvesting systems. As a result, it is currently possible to calculate excitation dynamics for biologically relevant systems where non-Markovian dynamic disorder and quantum coherence effects cannot be neglected [1, 48, 61, 64, 116].

For multi-pigment systems, the assumption is usually made that pigments are independently coupled to the environment [1, 48, 61].

First, the effect that correlated bath fluctuations within a cluster of pigments can have on inter-cluster excitation transfer is examined. Second, the effect of correlated bath fluctuations and the influence of structural, or static, disorder on linear absorption spectra and excitation transfer is investigated. In the next section we present the hierarchy equations of motion that are used to calculate excitation dynamics and absorption spectra, which is then followed by our results for the effect of correlation in a model BChl dimer and in light harvesting complex 2 (LH2).

4.2 System Hamiltonian parameters

Model Dimer. The system Hamiltonian of the dimer is given by Eq. 2.2 with $N = 2$ and coupling $V_{12} = V = 180\ \text{cm}^{-1}$ between the BChls chosen as the average of the inter- and intra-dimer couplings in LH2. All calculations for the dimer were done with hierarchy cut-offs of $L_T = 13$ and $K = 1$ using the time-local truncation [57, 61] and the Markovian temperature correction [54]. Static disorder widths are assumed to be $\sigma_n = 220\ \text{cm}^{-1}$, a value taken from previous fits to experimental absorption spectra of LH2 [97]. An average over many realizations of static disorder is thus taken for a more realistic view of the excitation dynamics present in the system. Averages over static disorder were performed over 5000 realizations of disorder.

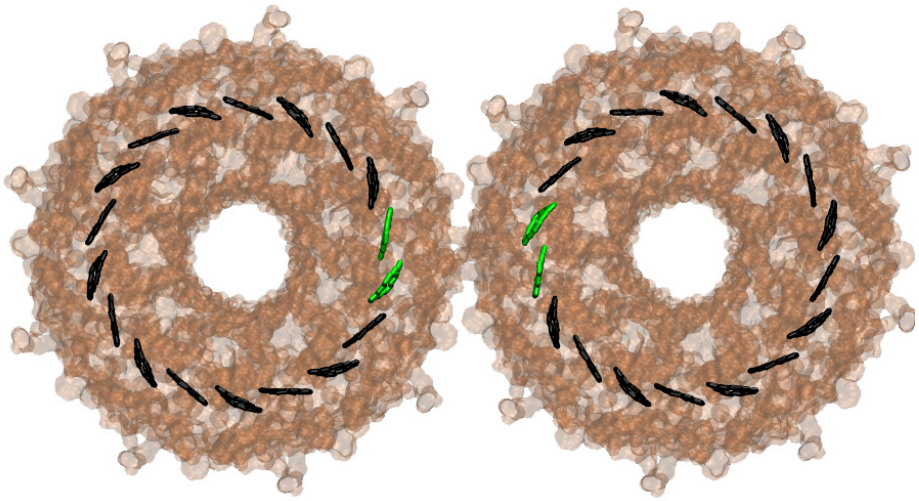

Figure 4.1: Two LH2 complexes in steric contact shown with their respective B850 rings in black. Highlighted in green is the nearest pair of BChls from each ring.

The two nearest B850 BChl pairs from two LH2s in steric contact (see Fig. 4.1) serve as a model for the excitation transfer between B850 rings. The inter-dimer coupling between BChls is chosen to be the highest and next-highest inter-complex coupling values of 10 cm^{-1} and 5 cm^{-1}, respectively. The system of 4 BChls is small enough that the computationally intensive HEOM can be treated in the presence of static disorder.

LH2. The coupling between neighboring BChls in the B850 ring is given by two terms: the coupling between BChls within the same α, β dimer V and the coupling between BChls of neighboring α, β dimers V'. The site energies and nearest neighbor interaction energies for the Q_y state of the B850 BChls are taken to be $E_n = 12,390\ \text{cm}^{-1}$, $V = 315\ \text{cm}^{-1}$ and $V' = 245\ \text{cm}^{-1}$ [97]. The

coupling between non-nearest neighbor BChls are determined using the induced dipole-induced dipole approximation which states

$$V_{nm} = C\frac{\hat{\mathbf{d}}_n \cdot \hat{\mathbf{d}}_m - 3\left(\hat{\mathbf{d}}_n \cdot \hat{\mathbf{r}}_{nm}\right)\left(\hat{\mathbf{d}}_n \cdot \hat{\mathbf{r}}_{nm}\right)}{|\mathbf{r}_{nm}|^3}, \tag{4.1}$$

where the coupling constant is $C = 348000$ Å^{3}cm^{-1} [13], the unit vector $\hat{\mathbf{d}}_n$ defines the orientation of the transition dipole moment of the Q_y excitation of BChl n, and $\mathbf{r}_{nm}$ is the vector connecting the Mg atoms BChls n and m.

4.3 System-bath interaction

To proceed with the integration of the HEOM, the system-bath interaction terms $\hat{F}_a$ need to be specified. Two systems are examined with different forms of correlated bath fluctuations. First a model two-site system is examined with uncorrelated, perfectly correlated and anti-correlated bath fluctuations. The case of the B850 ring of LH2 is then investigated with the already mentioned models of correlation between neighboring BChls; a distance-based correlation is also considered.

Model Dimer. The model dimer consists of the two B850 BChls in an $\alpha\beta$ subunit. Three different system-bath coupling mechanisms for the BChl dimer are investigated. The first corresponds to each BChl independently coupled to the thermal bath. In this case $M = 2$ and $\hat{F}_a = |a\rangle\langle a|$. A change in the position of oscillator q_j can thus affect the energy level of each excited state $|a\rangle$ independently, as given by the individual coupling terms c_{aj}. The interaction Hamiltonian H_{SB} is thus

$$\hat{H}_{SB} = \sum_{a=1}^{2} |a\rangle\langle a| \sum_j c_{aj} q_j. \tag{4.2}$$

The other two cases considered are perfectly correlated, denoted as "+"-correlated, fluctuations between the BChls and perfectly anti-correlated, denoted as "-"-correlated, bath fluctuations. For "+"-correlated fluctuations any change in position of oscillator q_j affects each excited state $|a\rangle$ in exactly the same way – both will either increase or decrease in energy by the same amount. For "-"-correlated fluctuations, any change in position of oscillator q_j will change the energy level of each excited state $|a\rangle$ in exactly opposite ways, i.e. where one increases by a certain amount the other will decrease by the same amount. For both + and "-"-correlated cases there is only a single system-bath interaction term, i.e., $M = 1$ holds in Eqs. 2.4 and 2.5. In the case of "+"-correlated

fluctuations holds $F_1 = (|1\rangle\langle 1| + |2\rangle\langle 2|)$ and the interaction Hamiltonian becomes

$$\hat{H}_{SB} = (|1\rangle\langle 1| + |2\rangle\langle 2|)\sum_j c_j q_j; \tag{4.3}$$

for "-"-correlated fluctuations holds $F_1 = (|1\rangle\langle 1| - |2\rangle\langle 2|)$ and the interaction Hamiltonian becomes

$$\hat{H}_{SB} = (|1\rangle\langle 1| - |2\rangle\langle 2|)\sum_j c_j q_j. \tag{4.4}$$

To investigate the effect of intra-dimer correlated fluctuations on the inter-dimer excitation transfer, a 4 BChl system is constructed from the nearest dimers of two LH2s in steric contact.

LH2. For the B850 ring four cases of correlation are investigated, the three cases discussed above and a distance based correlation. In all cases the system-bath coupling terms $\hat{F}_a$ are normalized such that $\mathrm{tr}\hat{F}_a\hat{F}_a = 1$ to ensure that the total reorganization energy on each BChl is kept constant. For perfectly correlated and perfectly anti-correlated bath fluctuations the system-bath coupling terms are

$$\hat{F}_a^{\pm} = \frac{1}{\sqrt{2}}\sum_{n=1}^{18}\left(|n\rangle\langle n| \pm |n+1\rangle\langle n+1|\right), \tag{4.5}$$

where cyclic counting is employed such that $18 + n \equiv n$.

The distance based correlation is employed to mimic coupling due to Coulomb interactions between charges. The assumption here is that fluctuations in the environment surrounding a BChl n will affect also BChl $m \neq n$ via Coulomb interaction, such that the coupling is inversely proportional to the distance between BChls m and n. The system-bath coupling terms are in this case

$$\hat{F}_a^C = C_a\sum_{n=1}^{18}\left[\frac{r_0}{r_{an}} - \left(1 - \frac{r_0}{r_{an}}\right)\delta_{an}\right]|n\rangle\langle n|, \tag{4.6}$$

where $r_0 = 1$ Å , r_{an} is the distance from BChl a to BChl n and

$$C_a = \left(1 + r_0^2\sum_{n\neq a} r_{an}^{-2}\right)^{-1/2} \tag{4.7}$$

The maximum correlation with the distance-based system-bath coupling terms is then ~ 0.1 for neighboring BChls. QM/MM calculations on LH2 have shown the maximum correlation between

B850 BChls to be near this value [117].

4.4 Results

The effect of correlated bath fluctuations is presented here for the BChl dimer and for the B850 ring of LH2. First, the effect on the absorption spectrum and excitation transfer for different cases of correlation are presented for the BChl dimer, in the presence and the absence of static disorder. Second, the effect on the absorption spectrum and excitation transfer of different cases of correlation are presented for the B850 BChls in LH2. All calculations for the model dimer and for the B850 ring were performed at $T = 300$ Kelvin.

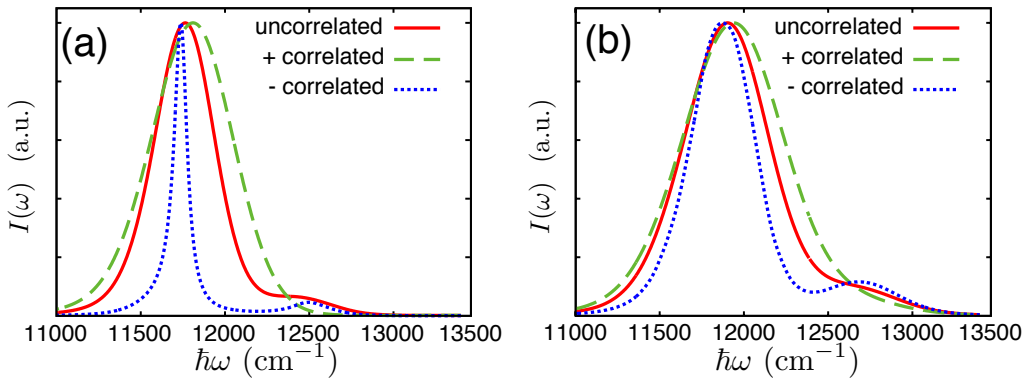

Figure 4.2: Spectra of a dimer with uncorrelated, "+"-correlated and "-"-correlated bath fluctuations without static disorder (a) and with static disorder (b).

Dimer spectrum. The dimer spectrum excluding static disorder is shown in Fig. 4.2a. As expected, perfectly correlated bath fluctuations have a Gaussian absorption spectrum. For both anti-correlated and uncorrelated bath fluctuations the absorption spectrum symmetry is lost and an enhanced tail on the blue edge of the spectrum appears. For anti-correlated fluctuations this tail is more prominent and the absorption spectrum is also significantly narrower than in the other cases. A general trend can be seen as the correlation shifts from positively correlated, to uncorrelated, to negatively correlated: the spectrum width decreases and the high-energy tail becomes more prominent.

The inclusion of diagonal static disorder of $\sigma = 220$ cm^{-1}, shown in Fig. 4.2b, still preserves the tail features of each spectrum and the aforementioned trend for the spectrum width. In each case of correlation, the inclusion of static disorder increases the width of the spectrum; the most significant increase in spectrum width is seen in the case of "-"-correlated bath fluctuations.

Inter-dimer transfer. The two nearest B850 BChl pairs from two LH2s in steric contact (see Fig. 4.1) serve as a model for the excitation transfer between B850 rings.

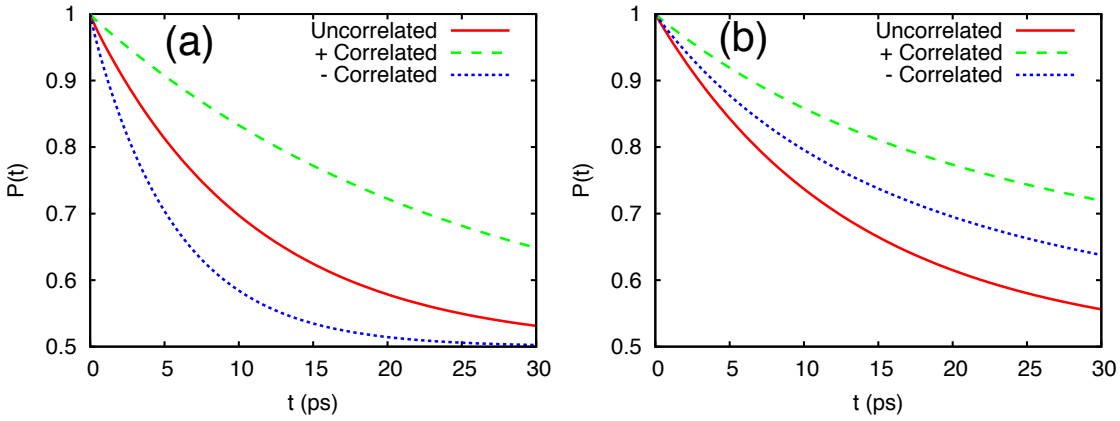

Figure 4.3: Donor population for uncorrelated, "+"-correlated and "-"-correlated bath fluctuations (a) excluding and (b) including static disorder.

Figure 4.3a shows the time-dependent population of the donor pair of BChls. It can be seen that in the absence of static disorder, perfectly correlated bath fluctuations significantly slow excitation transfer from the donor BChl pair to the acceptor pair; in contrast, perfectly anticorrelated bath fluctuations enhance excitation transfer. The transfer time τ can be determined from a fit of $\exp(-2t/\tau)$ to the donor population, and are presented in Table 4.1 for the pair of BChl dimer.

Table 4.1: Inter dimer transfer times from fits of a single exponential curve to $P(t)$ for each case of correlation as shown in Fig. 4.3 for the pair of BChl dimers. All values are in ps.

	"-"-correlated	uncorrelated	"+"correlated
Without static disorder	11.3	21.7	49.5
With static disorder	41.7	27.7	65.5

The inclusion of static disorder has a greater impact on excitation transfer in the presence of correlation than in the absence of correlation, as can be seen by comparing Figs. 4.3a and 4.3b. The fits of single exponential functions to the time evolution of the donor population shows that there is a 265% increase in the transfer time for "-" correlated fluctuations when static disorder is included, compared to 28% and 32% increases for uncorrelated and "+"-correlated fluctuations, respectively.

Excitation transfer in the presence of static disorder is thus fastest in the case of uncorrelated site energy fluctuations. In the presence of static disorder, a dimer with perfectly correlated bath fluctuations exhibits the slowest inter-dimer excitation transfer. Transfer between dimers with perfectly anticorrelated bath fluctuations is comparably faster; the fastest excitation transfer occurs

when each BChl has independent bath fluctuations.

For LH2 only the B850 ring of pigments are considered. Due to the large system size, it is computationally unfeasible to account for static disorder in this case. Also due to the large system size, the cut-off was reduced to $L_T = 4$, still employing time-local truncation.

LH2 spectrum. The linear absorption spectrum for a single B850 ring, shown in Fig. 4.1, was calculated for the cases of (I) uncorrelated bath fluctuations, (II) perfectly correlated fluctuations between each nearest-neighbor pair, (III) perfectly anti-correlated fluctuations between each nearest-neighbor pair and (IV) $1/r$ based correlation. It can be seen that the $1/r$ based correlation yields an absorption spectrum nearly identical to that calculated for uncorrelated bath fluctuations.

The trend of a narrowing spectral width as correlation between pigments goes from positive to negative, found for a BChl dimer, is also seen in Fig. 4.4 for the B850 ring of LH2. The increase in the number of pigments masks the signature of correlation from the high-energy tail region, however there is still a small increase in the tail peak with decreasing correlation. As the spectral features

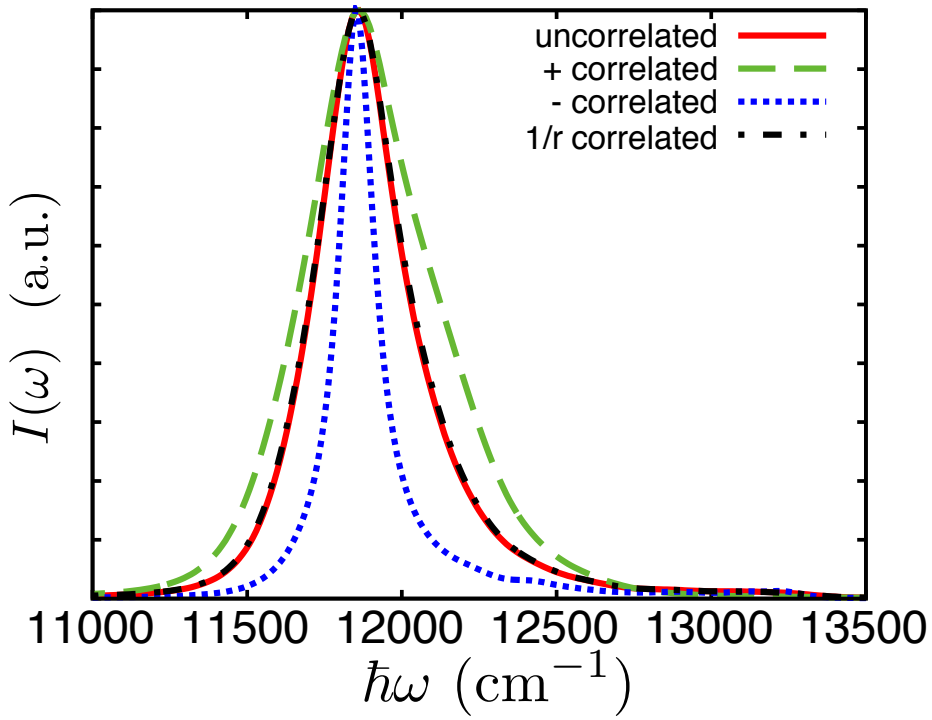

Figure 4.4: Linear absorption spectrum for the B850 ring of LH2 for uncorrelated, "+"-correlated and "-"-correlated and $1/r$ correlated bath fluctuations.

of the BChl dimer were preserved and in some cases enhanced by the inclusion of static disorder, it is expected that the same holds for the LH2 spectrum.

Inter-LH2 transfer. To test the effect of differently correlated bath environments on excitation transfer, the time evolution of the system density matrix $\rho(t)$ was calculated for the B850 rings of two LH2s that are in steric contact (see Fig. 4.1). The increase in system size made the cut-off of $L_T = 4$ computationally too demanding and, thus, was reduced to $L_T = 3$. Although this reduction in the cut-off does have an affect on the excitation relaxation dynamics, it was seen, based on shorter calculations (data not shown) of the donor populations at $t = 1$ ps, that there was less than 2% difference between $L_T = 4$ and $L_T = 3$ for any of the cases of correlated fluctuations. The comparison between the different cases of correlation thus remains valid even for the reduced truncation.

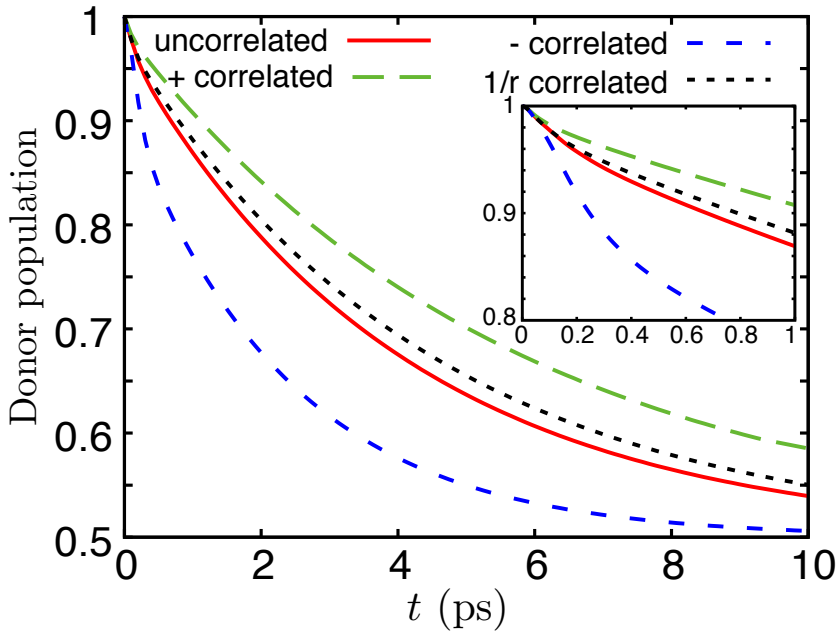

Figure 4.5: Donor B850 population for uncorrelated, "+"-correlated, "-"-correlated and $1/r$ based correlated bath fluctuations, for the pair of LH2s shown in Fig. 4.1

The evolution of the donor population is shown in Fig. 4.5 for the different cases of correlation. In contrast to the linear absorption spectra, there is an observable difference in the excitation transfer between uncorrelated bath fluctuations and $1/r$-correlated bath fluctuations. Perfect correlation between neighboring BChls hinders excitation relaxation from the initial state, which reduces transfer between B850 rings. In contrast, anti-correlated bath fluctuations of neighboring BChls assists relaxation from the initial state. This can be seen from the faster initial decline (see inset of Fig. 4.5) of the donor population for "-"-correlated bath fluctuations compared to the other cases of correlation. The transfer times based on fits of single exponentials to the donor populations shown

in Fig. 4.5 is given in Table 4.2.

Table 4.2: Inter LH2 transfer times determined from fits of a single exponential curve to $P(t)$ for each case of correlation as shown in Fig. 4.5 for the pair of B850 rings. All values are in ps.

"-"-correlated	uncorrelated	$1/r$-correlated	"+"-correlated
4.7	8.03	8.89	11.17

The effect of correlation on excitation transfer between two B850 rings is similar to that on excitation transfer between two BChl dimers. As nearest-neighbor correlation decreases from perfectly correlated, to partially correlated ($1/r$-correlated) to negatively correlated, the transfer time also decreases. This trend is identical to that which is observed for the transfer between two BChl dimers excluding the effect of static disorder.

4.5 Discussion

The effect of correlated dynamic disorder on excitation transfer between clusters of bacteriochlorophylls (BChls) was investigated for a model BChl dimer system and for the B850 ring of light harvesting complex LH2. In either case the extremes of perfectly correlated and perfectly anti-correlated coupling to heat baths were studied and compared to that of completely uncorrelated bath coupling. The aim was to investigate how fluctuations of a heat bath that are correlated between BChls in a cluster affect excitation transfer to another cluster of BChls. It was shown that for both the BChl dimer and the B850 ring, correlated bath fluctuations broaden the absorption spectrum and suppress excitation transfer as compared to uncorrelated bath fluctuations. In contrast, negatively correlated intra-cluster bath fluctuations tend to narrow the absorption spectrum and enhance inter-cluster excitation transfer.

Hennebicq et al. [118] studied the effect of correlated fluctuations between a donor and acceptor pair where, in contrast to the present investigation, the correlations were between the donor and acceptor pigments. They found that in the weak coupling limit, for over-damped Brownian oscillator the effect of same or opposite sign correlations was to cause a respective decrease or increase of the reorganization energy. The effect of an increase in reorganization energy is to damp out the coherent oscillations within the donor cluster of pigments and induce quick relaxation from the initial state into the steady state.

The respective changes in the transfer rate between clusters of pigments with intra-cluster fluc-

tuations can be understood based on the differences in the absorption spectra for each case of correlation. In the case of perfectly anti-correlated fluctuations, the absorption spectrum is narrowest with the effect that most of the excitation is carried by a single, partially coherent, delocalized state. Furthermore, the exciton state carrying most of the excitation is one of the lower energy states with a high transfer rate to the acceptor [1]. As the correlation increases from negative to positive values, the absorption spectrum broadens and the excitation is shared between more of the higher energy exciton states, which have lower transfer rates, and thus the overall transfer is slowed down.

The inclusion of static disorder was also shown to have a significant impact on the absorption spectra and excitation transfer in the case of the BChl dimer. Due to the large size of the B850 ring and the poor scaling of the hierarchy equations of motion, only a dimer system could be modeled with static disorder. It was shown that the inclusion of static disorder slows down excitation transfer and broadens the spectra for all cases of correlation investigated. In particular, the enhancing effect of negative correlation on excitation transfer is countered by the inclusion of static disorder: the narrow absorption band is clearly broadened such that the low energy exciton state with the higher transfer rate carries less of the excitation. This effect is not as prominent in the cases of uncorrelated and positively correlated fluctuations.

Since the absorption spectra and excitation migration of B850 rings follow the same correlation-based trends as seen for the BChl dimers excluding static disorder, it is expected that static disorder should have a similar effect on the B850 rings as it has on BChl dimers. Our results indicate that the inclusion of intra-LH2 correlated bath fluctuations, whether positive or negative, would likely slow inter-LH2 excitation transfer.

There are many questions that remain on this subject, such as how the interplay of the various parameters affect excitation transfer in the presence of correlated fluctuations. Similarly, it would be interesting to understand what the effect of correlated static disorder could be.

It has been shown that inter-LH2 excitation transfer follows simple incoherent transfer kinetics and can, in the case of uncorrelated diagonal disorder, be accurately described by generalized Förster theory. The results for inter-LH2 transfer cannot necessarily be generalized to that of LH1-RC transfer due to the larger size of LH1 compared to LH2 and close packing of LH1 around the RC. The next Chapter presents the results of the investigation on LH1-RC excitation transfer.

Chapter 5

Excitation dynamics of the photosynthetic reaction center and light harvesting complex 1

5.1 Introduction

The structure of the reaction center from the purple bacterium *Rhodobacter* (*Rb.*) *sphaeroides* was solved in 1987 [119], revealing the atomic positions and conformation of the pigment molecules (Fig. 5.1a). Noteworthy in the structure was how two of the six primary pigment molecules, the special pair BChls, were placed very close together (separated by only 7.5 Å) [120]. Additionally, two further BChls and two bacteriopheophytin (BPheo) molecules were also identified and placed. Altogether the six pigments can be classified into three groups, special pair BChls (P), accessory BChls (B) and BPheos (H), each of which has been assigned to one of the three peaks seen in the RC's absorption spectrum [121, 122] (Fig. 5.1b).

The reaction center in purple bacteria is surrounded by an antenna complex known as light harvesting complex 1 (LH1) [123], thus forming the LH1-RC core complex (Fig. 5.1c). LH1 contains 32 additional BChls that result in a strong absorption peak at 875 nm and, hence, are called the B875 BChls. By surrounding the RC with additional pigment molecules the amount of sunlight that the cell can absorb is greatly increased [7, 8], thus allowing the cell to exploit electron transfer in the RC [124–132].

A slight asymmetry in the structure of the RC leads to a similar asymmetry in the energy levels of the pigments. This results in a highly dominant path for charge separation, labeled the "L" side, whereas the non-dominant side is labeled "M" [133–138]. Accordingly, there are altogether six pigment excitation energies to model with site energies $E_{P_{L/M}}$, $E_{B_{L/M}}$, $E_{H_{L/M}}$. The close proximity of the special pair BChls suggests strong interaction between their excited states, leading

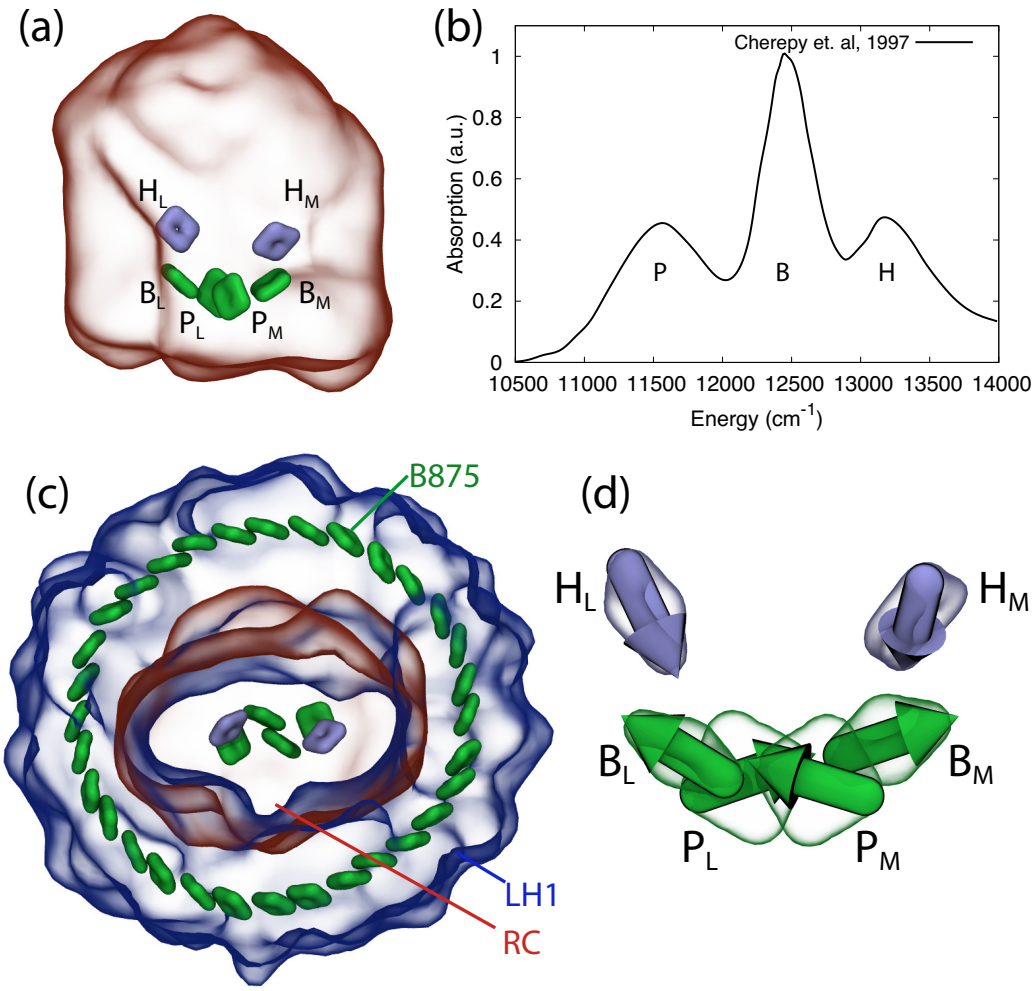

Figure 5.1: (a) Position of bacteriochlorophylls (P_M, P_L, B_M, B_L), and bacteriopheophytins (H_M, H_L) in the reaction center (RC) from *Rhodobacter sphaeroides*. (b) RC infrared absorption spectrum from Ref [122].

to strong, i.e., thermally robust, coherent sharing of excitation between the two BChls [19]. Recent experiments [139] have also revealed coherence effects between the B and H pigments. The three-peaked RC absorption spectrum, therefore, is not simply the sum of the spectra of three separate pigment groups, but results from their coherent mixing.

To account for the RC excited state dynamics, the vertical excitation energies and pigment-pigment interaction energies need to be characterized. There have been many efforts toward this goal [19, 105, 140–150], but only parts of the system were modeled at a time. In the present work we furnish an overall description of RC excitation dynamics employing a method that has become widely accepted [1, 61, 63, 64, 151, 152], namely the hierarchy equations of motion (HEOM) method. To apply the method we suggest an effective Hamiltonian and coupling to the environment. We

demonstrate that the suggested model reproduces well the observed RC absorption spectrum. We examine then the excited state dynamics of the RC pigments.

Similar to the RC, light harvesting complex 1 (LH1) represents a fundamental, much studied photosynthetic system that is also governed by strong pigment - pigment interaction and strong coupling to a finite temperature environment. LH1 and RC interact closely with each other and so they are investigated jointly in the present study by the HEOM approach. For LH1 we resort to a previously chosen effective Hamiltonian [30, 97]. The close proximity of LH1 and RC brings into question whether excitation transfer occurs incoherently between them, as has been previously assumed , but to be expected only for transfer between distant groups of pigments [3, 13, 81].

For the application of the HEOM method we employ the program PHI developed by the author and Schulten [9]. The program, made available to other researchers[1] integrates the HEOM efficiently on single processor and multi-processor shared memory computers.

In the next section we briefly introduce the effective Hamiltonian and model of the coupling to the thermal environment. Stating then two possible choices of the associated model parameters, we present the resulting excitation dynamics of the RC and the LH1-RC excitation transfer.

5.2 Model of pigments in RC

To determine how excitation transfers between LH1 and RC a description of the quantum system comprising the excited LH1 and RC pigments and their interaction with the surrounding protein environment is needed. Due to the complexity of systems like those seen in light-harvesting an effective Hamiltonian description is often used to characterize such systems [1, 13, 46–48, 61]. The effective Hamiltonian involves only the most relevant subset of states. In case of excitation dynamics of light harvesting systems, the low-light photon level in the habitat of the biological organisms permits one to confine the effective Hamiltonian to the manifold of single pigment excitations, yielding an effective Hamiltonian given by

$$H_0 = \sum_n E_n \left|n\right\rangle \left\langle n\right| + \sum_{n,m} V_{nm} \left|n\right\rangle \left\langle m\right|, \tag{5.1}$$

where $|n\rangle$ describes the state in which the n-th pigment is excited and all the others are in the ground state. E_n ais the vertical excitation energy of pigment n; V_{nm} is the interaction matrix element between the excited states of pigments n and m. There exist many parameterizations of

[1] PHI is available at `http://www.ks.uiuc.edu/Research/phi`

the system Hamiltonian, some of which are listed in Table 5.1.

Interaction energies between the excited state of pigments are typically determined using the point-dipole approximation, and are then

$$V_{nm} = C\left[\frac{\hat{\mathbf{d}}_n \cdot \hat{\mathbf{d}}_m - 3\left(\hat{\mathbf{r}}_{nm} \cdot \hat{\mathbf{d}}_m\right)\left(\hat{\mathbf{r}}_{nm} \cdot \hat{\mathbf{d}}_m\right)}{r_{nm}^3}\right], \tag{5.2}$$

where $\mathbf{r}_{nm}$ is the vector connecting the center of pigment n to the center of pigment m, $\mathbf{d}_n$ and $\mathbf{d}_m$ are the transition dipole moments of pigments n and m (see Fig. 5.1d); the constant $C = 146,798$ cm^{-1} is chosen to reproduce BChl Q_y excited state interactions in a protein environment [13]. The point dipole approximation has been shown to account well for interaction energies of well separated pigments ($>$ 1.5 nm Mg-Mg distance), but in case of neighboring pigments in the RC and LH1 ($<$ 1 nm) the interaction energies need to be determined case by case following, for example, the procedure suggested in Ref [19].

Table 5.1: System Hamiltonian parameters for the bacteriochlorophyll and bacteriopheophytin pigments in *Rhodobacter sphaeroides* reaction center (all in cm^{-1}).

	Hu (1997)[19]	Jordanides (2001) [141]	Chang (2001) [142]	Jordanides (2004) [143]	Linnanto (2009)[105]
E_{P_M}	12,746	11,610		11,772	11,807
E_{P_L}	12,746	11,610		11,578	11,710
E_{B_M}	12,860	12,220	12,403	12,400	12,407
E_{B_L}	12,860	12,370	12,500	12,500	12,453
E_{H_M}	12,820	13,150		13,200	
E_{H_L}	12,820	13,020		12,900	
V_{PP}	1000	395	402		600
$V_{P_M B_M}$	-50	-16	30		
$V_{P_L B_L}$	-27	2.82	20	4	
$V_{P_M B_L}$	-496	-104			
$V_{P_L B_M}$	-418	-94		-216	
$V_{B_M H_M}$	442	95		202	
$V_{B_L H_L}$	463	123		184	

The pigments of LH1 and RC are embedded into the protein matrix, all of which fluctuate at ambient temperatures. To model excitation dynamics in the presence of thermal fluctuations the HEOM, presented in Chapter 2, are employed. The fluctuations affecting pigment n are specified in this case through two parameters, the reorganization energy λ_n and response frequency γ_n. The reorganization energy parameter λ_n determines the coupling of thermal fluctuations to the excited state $|n\rangle$. Higher values of λ_n leads to stronger damping of excited state dynamics compared to lower

values, thus λ_n is also referred to as the damping strength. The Drude spectral, Eq. 2.10 density describes the influence of an over-damped harmonic oscillator with damping time $\tau = \hbar/\lambda$, $\hbar$ being the reduced Planck's constant. This spectral density has been shown to reproduce experimental absorption spectra and excitation dynamics in the context of the HEOM [1, 6, 48, 61].

In addition to the fluctuations introduced by the thermal environment, one needs to account for long-time, structural disorder that is not accounted for in the harmonic bath model. In case of the RC calculations disorder is phenomenologically included in the form of Gaussian disorder, often termed static disorder, of the diagonal elements of the system Hamiltonian with widths σ_P, σ_B and σ_H for the P, B and H pigments. An ensemble average over 1000 realizations of static disorder was done for the calculation of the RC absorption spectra. Previously reported bath parameters for the RC pigments in our calculations are given in Table 5.2.

Table 5.2: System-environment interaction parameters for the bacteriochlorophyll and bacteriopheophytin pigments in the *Rhodobacter sphaeroides* reaction center (all in cm^{-1}).

	Jordanides (2001)[141]	Jordanides (2004) [143]	Linnanto (2009)[105]	Jing (2012)[145]
λ_P	100			
λ_{B_M}	80	280		17.6
λ_{B_L}	80	280		16.0
λ_{H_M}	80	280		39.5
λ_{H_L}	80	280		50.5
$\hbar\gamma_P$	88.2			
$\hbar\gamma_B$	88.2			52.9
$\hbar\gamma_H$	88.2			52.9
σ_P	170		93.6	
σ_B	55	55	93.6	410
σ_H	55	55		430

5.3 Results

To reproduce the absorption spectrum of the reaction center using non-Markovian excitation dynamics as calculated by the HEOM, two sets of parameters, largely based on previous choices, are suggested here. The two sets are able to yield the observed RC absorption spectrum, parameter set 1 assuming strong damping (high dynamic disorder) and parameter set 2 assuming weak damping (low dynamic disorder). The RC absorption spectra resulting from parameter sets 1 and 2 are shown in Fig. 5.2. The parameters for the system Hamiltonian, listed in Table 5.3, are very similar for sets 1 and 2 and also show little deviation from what has been reported in the literature [19, 105, 141–

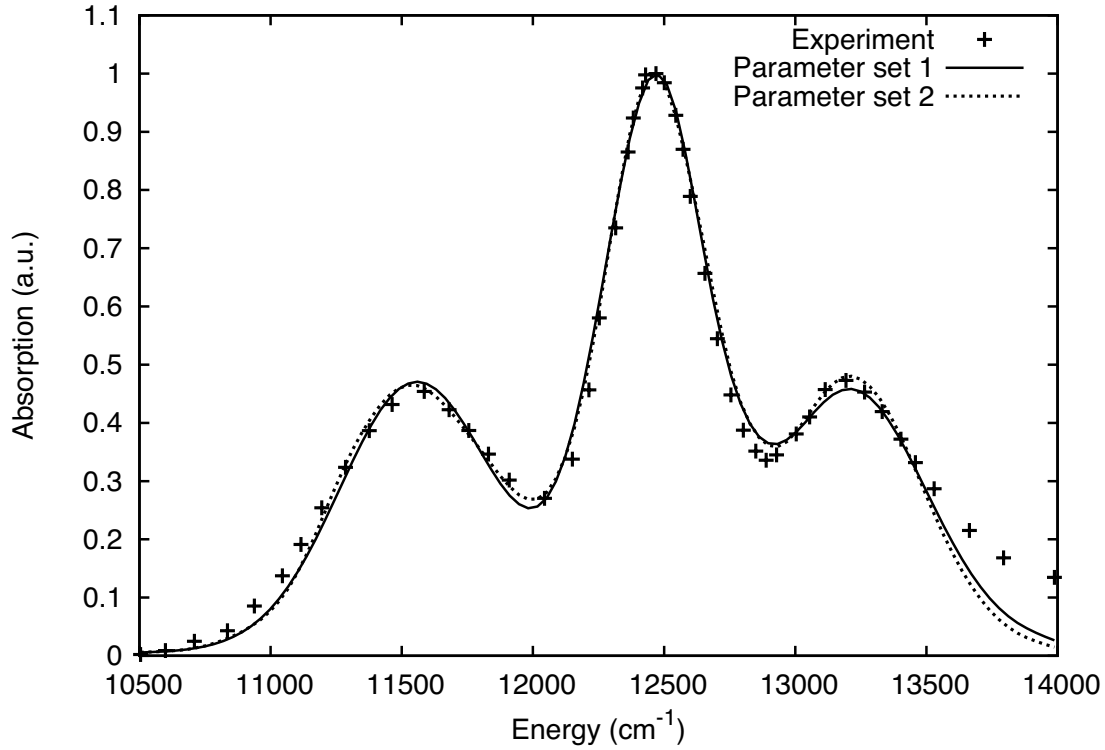

Figure 5.2: Comparison of 300 K linear absorption spectra calculated by the HEOM and observed experimentally as reported in Ref [122].

143]. The calculated linear absorption spectra exhibit greater sensitivity to the effective Hamiltonian parameters than to the bath parameters. The low sensitivity to the bath parameters is apparent from the good fits to the experimental absorption spectrum obtained for both parameter sets.

The excited state populations calculated using parameter sets 1 and 2 is shown in Fig. 5.3. The populations shown are not averaged over static disorder to provide a view for a single RC, as opposed to a view for an ensemble average that may hide detail [152]. The damping times $\tau_n = \hbar/\lambda_n$ associated with parameter set 1 are $\tau_P = 19$ fs, $\tau_B = 48$ fs and $\tau_H = 33$ fs; for parameter set 2 they are $\tau_P = 66$ fs, $\tau_B = 130$ fs and $\tau_H = 100$ fs. Figure 5.3 clearly shows that coherent oscillations of the B and H pigments, similar to those seen in Ref [139].

As the diagonal entries in the effective Hamiltonians of parameter set 1 and 2 differ little, the steady-state populations of the pigments are very similar between the parameter sets, as expected. The relaxation times, however, are very different: in case of parameter set 1, the assumed high damping results in the populations reaching their steady-state values in about 2 ps, compared to 10ps in the case of parameter set 2 that assumes weak damping.

To obtain insight into which pigments comprise the absorption peaks, the exciton states were

Table 5.3: Parameters for the RC Hamiltonian, H_S, and spectral densities J_n, obtained from fits to experimental spectra (all in cm^{-1}).

	Parameter set 1	Parameter set 2		Parameter set 1	Parameter set 2
E_{P_M} †	12,190	12,180	λ_P	280	80
E_{P_L} †	12,090	12,080	λ_B	110	40
E_{B_M} †	12,510	12,500	λ_H	160	50
E_{B_L} †	12,540	12,530	$\hbar\gamma_P$	52.9	52.9
E_{H_M} †	13,280	13,200	$\hbar\gamma_B$	52.9	52.9
E_{H_L} †	13,140	13,170	$\hbar\gamma_H$	52.9	52.9
V_{PP}	500	500	σ_P	240	380
$V_{P_M B_M}$	-60	-50	σ_B	90	190
$V_{P_L B_L}$	-60	-50	σ_H	120	240
$V_{P_M B_L}$	-70	-60			
$V_{P_L B_M}$	-70	-60			
$V_{B_M H_M}$	140	130			
$V_{B_L H_L}$	140	130			

† parameters include the renormalization term H_{REN}.

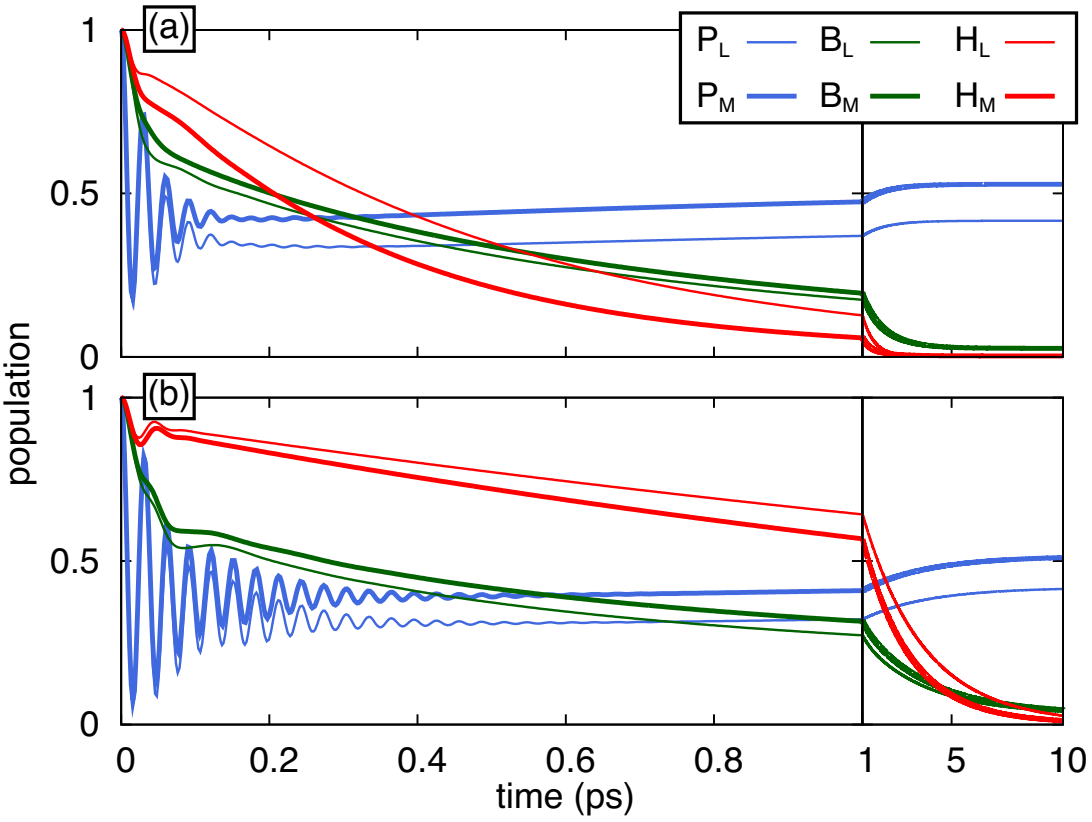

Figure 5.3: Excitation dynamics of the reaction center calculated with system and bath parameters taken from Table 5.3, where parameter set 1 (a) assumes high dynamic disorder and parameter set 2 (b) assumes low dynamic disorder. Populations are shown for the pigments initially excited in each calculation.

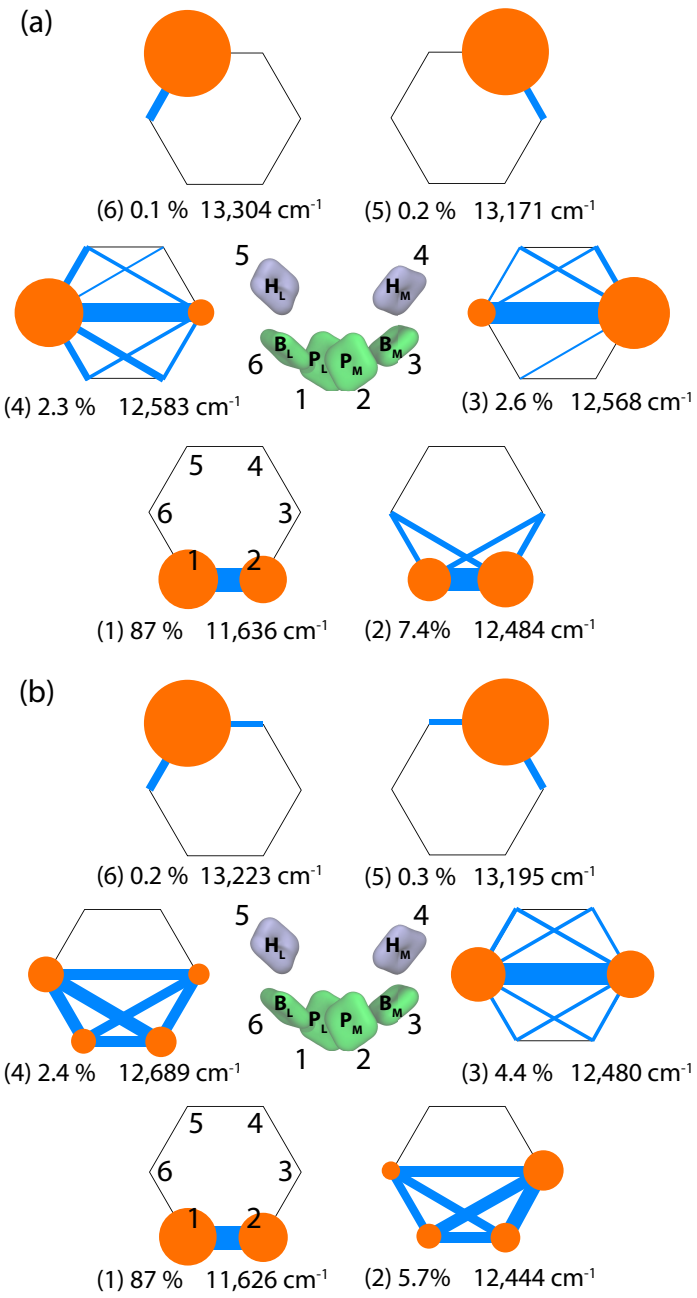

Figure 5.4: Reaction center exciton states. The exciton states, $|\widetilde{\nu}\rangle$, are defined as eigenstates of the stationary state density matrix, namely, $\rho_e|\widetilde{\nu}\rangle = P_\nu|\widetilde{\nu}\rangle$; parameters were taken from Table 5.3, where parameter set 1 (a)assumes high dynamic disorder and parameter set 2 (b) assumes low dynamic disorder. Orange circles (radius scales with diagonal elements of $|\widetilde{\nu}\rangle\langle\widetilde{\nu}|$) indicate the participation of each pigment in an exciton state, and blue lines (thickness scales with absolute value of off-diagonal elements of $|\widetilde{\nu}\rangle\langle\widetilde{\nu}|$) inter-pigment coherence. Listed are also the steady-state population P_ν and energy ϵ_ν of each exciton state. The numbering of the states is in energetically ascending order.

also computed. The exciton states were obtained by diagonalizing the steady state density matrix ρ_e, i.e., by solving for $\langle \mathcal{U}(t)\rangle_B \rho_e = \rho_e$ and diagonalizing the resulting ρ_e. A graphical representation of the exciton states is given in Fig. 5.4, which shows how much a pigment participates in an exciton

state and illustrates the quantum coherence between the pigments associated with each exciton state.

There is little difference between the two parameter sets of the most populated (lowest energy) exciton states. Indeed, the primary difference is only that the exciton states in parameter set 2 exhibit a bit stronger coherence, which is expected due to the localizing effect of the stronger damping for parameter set 1. The special pair BChls are seen to carry the majority of the steady-state population, the accessory BChls carrying only about 10% of the steady state population and the BPheos almost none. The correspondence between pigments and peaks in the absorption spectra can also be discerned from Fig. 4. For both parameter sets the lowest energy peak, around 11,500 cm^{-1}, is produced by only a single exciton state. The middle peak, around $12,500$ cm^{-1} is produced by a combination of three exciton states that are energetically nearly degenerate. These states are coherently delocalized over the P and B pigments due to the pigments' strong interactions and energetic proximity. The highest energy peak, around 13,300 cm^{-1}, is made up of two exciton states that correspond almost exactly to each H pigment.

The spectrum of LH1 and excitation transfer between LH1 and RC were also examined using the HEOM. For these calculations the parameters for the effective Hamiltonian, listed in Table 5.3, were adopted from Ref [30].

The transfer of excitation from the B875 ring to RC pigments is shown in Fig. 5.5b. Although strong damping results in fast equilibration within a complex (see Fig. 5.3), it hinders inter-complex excitation transfer. To obtain inter-complex transfer rates the dynamics were fitted to a simple kinetic model, namely

$$\frac{dP}{dt} = -k_f P + k_b(1-P), \tag{5.3}$$

where P is the LH1 excited state population, k_f is the LH1$\rightarrow$RC transfer rate and k_b is the RC$\rightarrow$LH1 transfer rate. The transfer rates obtained for parameter set 1 are $k_f = 1/(42.1 \text{ ps})$, $k_b = 1/(15.8 \text{ ps})$, and for parameter set 2 are $k_f = 1/(33.8 \text{ ps})$, $k_b = 1/(5.6 \text{ ps})$. The transfer rates obtained with parameter set 2 are closest to previously reported values of k_f =1/(25 ps) and k_b =1/(8 ps) [92, 125, 126, 140, 154, 155]. Including static disorder in the excitation transfer calculation should increase the transfer times by 10-20% [6].

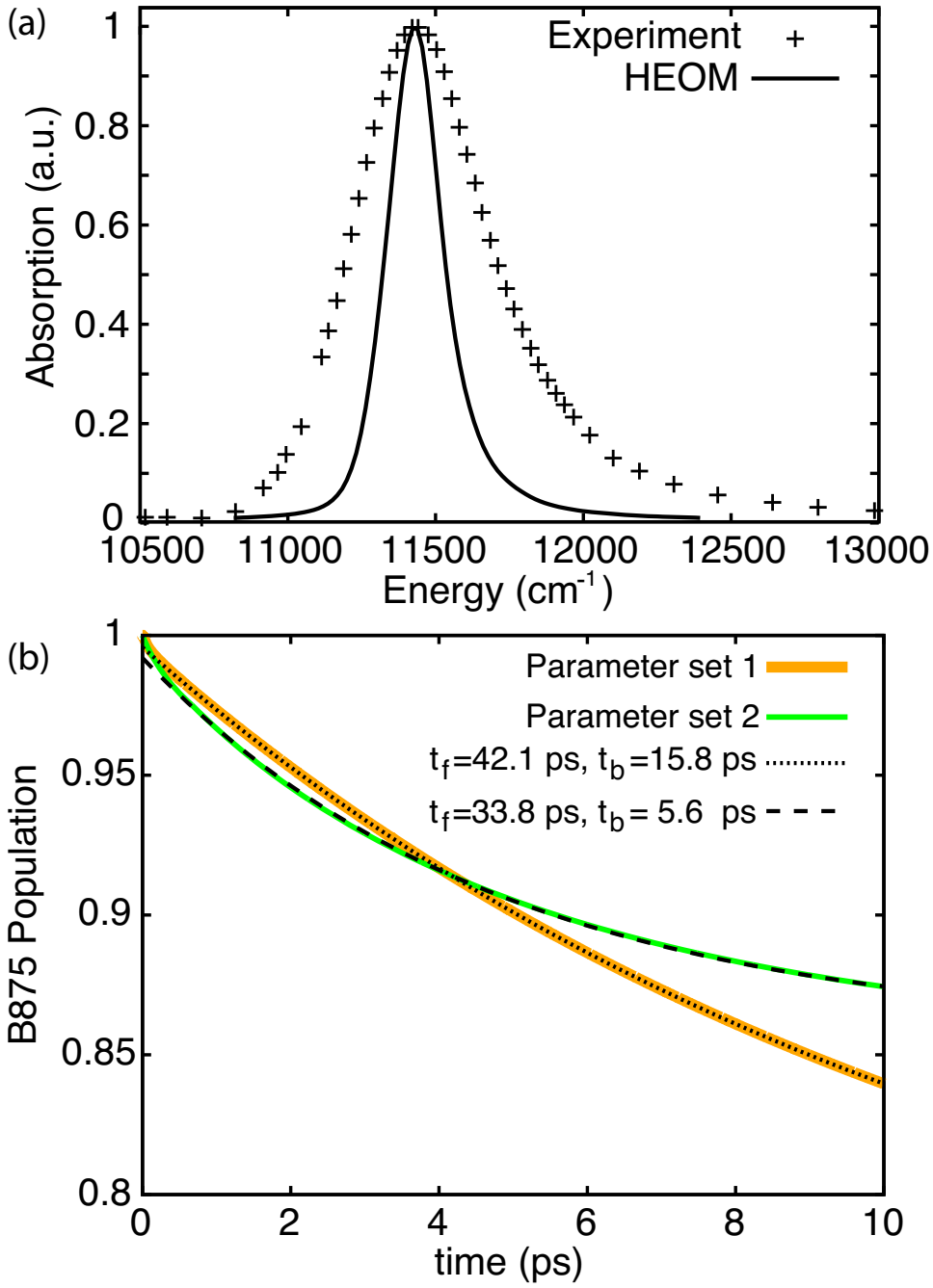

Figure 5.5: (a) LH1 absorption spectrum. Shown is a comparison of spectra from Ref [153].

5.4 Discussion

To investigate excitation transfer between the pigments in the reaction center (RC) and light harvesting complex 1 (LH1), i.e., the complexes comprising the core particle in purple photosynthetic bacteria, a consistent set of parameters for the RC pigments was needed. We have determined an effective

Hamiltonian and coupling to a heat bath for the RC pigments from *Rhodobacter sphaeroides* that reproduce, in the framework of non-Markovian dynamics as described by the HEOM [1, 6, 45, 60], the 300 K linear absorption spectrum and experimental results stemming from particularly sensitive probes of RC excitation dynamics [139].

Prior studies investigating excitation transfer in LH1-RC postulated an incoherent hopping process even though the pigments complexes of RC and LH1 are in relatively close proximity. By employing the HEOM, excitation transfer between LH1 and RC could be investigated without making such an assumption. It was shown that population relaxation due to LH1-RC excitation transfer indeed follows a single exponential function, concluding that it is incoherent and is, as shown in Fig. 5.5b, well described by a simple kinetic model. This result justifies the use of generalized Förster theory [92] in describing LH1-RC excitation transfer.

Our results reveal that the rate of LH1-RC excitation transfer is strongly affected by the environmental coupling of the RC pigments. We find that weak damping leads to slow intra-complex relaxation but results in fast inter-complex excitation transfer. Although at first glance counter-intuitive, RC→LH1 transfer is faster than LH1→RC transfer. The fast back-transfer is still slower than photo-induced $P \rightarrow H_L$ electron transfer and allows captured photon energy, which would otherwise be lost, to be funneled to a different RC in case it reaches one that has recently undergone charge separation [81]; back-transfer also spreads superfluous excitation energy across all pigments, avoiding radiation damage to the RC. Our results show that the back-transfer rate RC→LH1 is significantly faster with weak damping compared to strong damping. Weak coupling between RC pigments and environment, thus, promotes protection from radiation damage and results in overall improvement of light harvesting efficiency.

The calculation of RC spectra and LH1-RC excitation dynamics using the HEOM is only possible with an efficient numerical implementation of the method. Indeed, with only a single CPU, these calculations would not be possible. In the next Chapter the implementation of the HEOM in the software PHI is described and its efficiency is demonstrated by computing excitation transfer for the case of LH2-LH1, a 50-pigment system.

Chapter 6

Open quantum dynamics calculations on parallel computers

6.1 Introduction

Quantum dynamics plays a major role in many biological processes [16, 50, 156, 157]. To model such processes one has to account for the environment in which they occur, that is, one where thermal noise at an ambient temperature is present. Although many methods have been developed that account to some degree for the interaction between a quantum system and a thermal environment [49, 50, 87, 111, 113, 114, 158–164], they typically involve limitations in regard to the relative interaction strengths found within a system and between the system and environment, or make approximations regarding the quantum nature of the system, or neglect non-Markovian effects. Such limitations and approximations are often permissible for a particular system and then the respective methods yield valuable insight, but they do not apply in general.

There are only a few quantum dynamics methods for computation of open quantum system density matrices that take into account arbitrary intra-system and system-environment interactions, include non-Markovian effects, and make no assumptions about the quantum nature of the dynamics [44, 45, 51–55]. The hierarchy equations of motion (HEOM) of Tanimura and Kubo [44], which employ a hierarchy of auxiliary density matrices to account for non-Markovian dynamics without resorting to perturbative approximations [44, 45, 54–61, 68, 165–167], is one of the earliest open quantum system descriptions and remains the only one applicable to large systems [1, 4, 6, 61]. Although the HEOM are computationally expensive, typically requiring many gigabytes (GBs) of computer memory and many days of computation time, their application to large systems has been possible by exploiting GPUs [65] and highly parallel computers [1, 4, 6].

Implementing the HEOM on a multi-processor computer is, however, difficult due to the highly connected nature of the auxiliary density matrices. To achieve peak performance, the communication between processing elements needs to be minimized through a partitioning scheme that assigns each matrix in the hierarchy to a different processor. Additional improvements to calculation time can also be achieved by employing adaptive integration methods: either by adaptively filtering the number of auxiliary matrices or by adaptively adjusting the integration step size.

Besides an application to large photosynthetic systems, such as those found in cyanobacteria, plants and artificial light harvesting [168–172], the HEOM method is applicable to a wide range of other quantum systems. Indeed, any process that can be described by a set of N discrete quantum states in contact with a bosonic environment can be modeled [45].

In the following section we present the partitioning scheme and integration methods used to implement the HEOM, as well as performance benchmarks of our parallel hierarchy integrator PHI [1].

6.2 Numerical integration of HEOM

The HEOM, introduced in Chapter 2, present a significant computational challenge for all systems but one, a two state system. Within single pigment-protein complexes in photosynthetic systems, pigment numbers lie typically between 6 and 90, depending on species and growth conditions [173]. To overcome the issues of poor scaling with system size and truncation (Fig. 2.2), and because of the highly coupled nature of the equations, the HEOM need to be implemented computationally in the most efficient manner. This section describes the implementation of the HEOM in the parallel hierarchy integration software PHI capable of calculating excitation dynamics for systems containing up to 60 pigments at permissible truncation levels [4].

Adaptive integration. Since the HEOM describes thermally averaged time evolution, the ADMs will exponentially approach, in the absence of an external driving field, a steady-state. Any initial state of the system will relax to a steady state, leading during the relaxation to increasingly smaller changes in time of the elements of each ADM.

Shi et al. [60] proposed a rescaling of the ADMs that permits an automatic removal of the ADMs while integrating the HEOM. During integration, the ADMs are adaptively removed when their maximum absolute value is less than a defined filter accuracy δ_F. This filtering greatly reduces the memory requirements for integrating the HEOM for moderate-sized systems [60, 65], but can lead

[1] PHI is presently available at `http://www.ks.uiuc.edu/Research/phi`

to artifacts with choices of δ_F values that are too large.

By employing the same rescaling of the ADMs as employed by Shi et al. [60], one can exploit the damped dynamics by integrating the HEOM with an adaptive timestep. Among the many adaptive integration methods, the Runga-Kutta-Fehlberg (RKF45) method [174] stands out as most practical as it is a 5th order integration algorithm that does not require the re-calculation of a timestep with a different step size in order to evaluate the integration error. The method, instead, re-uses the interim Runga-Kutta steps to also compute a 4th order integration step; at the end of a single timestep, the 4th order timestep calculation is compared with the 5th order timestep calculation and the step is kept or discarded according to a tolerance δ_I and the step size is increased or reduced accordingly.

Adaptive integration by the RKF45 algorithm requires 6 evaluations of the equations of motion, compared to 4 evaluations when using Runga-Kutta 4 (RK4) fixed timestep integration. The additional computation per RK45 step compared to a RK4 step, however, typically results in an order of magnitude decrease in the number of integration steps compared to RK4 with an overall reduction in total computation time. Rapid initial dynamics as well as long-time relaxation to the steady-state are both covered efficiently, with an overall short calculation time and a pre-defined integration error tolerance.

Adaptive timestep integration, however, cannot typically be used in conjunction with the adaptive ADM filtering method of Shi et al. [60] as the latter introduces artifacts in the time evolution of the ADMs that result in the adaptive integration method taking smaller time-steps than without the automatic filtering. As will be shown in Results below, suitable choices of δ_F and δ_I values still result in speed-up within an acceptable error.

Partitioning. Central to efficient integration of the HEOM is the use of parallel computing. Unfortunately, large numbers of processors linked in computer clusters (i.e., in distributed memory computers) with a low network bandwidth cannot be used since the HEOM, particularly for systems of many pigments, are extremely coupled, and require a high bandwidth for inter-processor communication. This communication cost can, however, be managed by employing multiple threads running on a multi-processor, shared memory computer.

In principle it is relatively straightforward to assign P processing threads (where each thread is an independently executing process able to communicate with other threads and access the same shared memory) to a set of ADMs. Integration then proceeds by computing and applying the integration updates from the HEOM in parallel, pausing between each step to synchronize data between the

Listing 6.1: Pseudo-code to generate index vectors $\mathbf{n}$ for any Pascal's d-simplex, where $d = M(K+1)$ for the HEOM, up to a specified truncation level. Scalar assignment operations are indicated by "=="; vector assignment operations are indicated by ":=".

```
d = M*(K+1);
vertexID = 0;                                          # unique ID for each vertex
indexVectorList[vertexID][] := vector of d zeros;      # index vectors
verticesInLevel[0][0] = vertexID;                      # store vertices for each level
numVertsInLevel[0] = 1
vertexID += 1;
totalNumVertices = 1;
for k = 1 to truncationLevel-1
   vertexCount = 0;
   for n = 0 to d-1
      for i = 0 to numVerticesInLevel[k-1]-1
         prevVertexID = verticesInLevel[k-1][i]
         tmpIndexVector[] := indexVectorList[prevVertexId][];
         m = (i+n) modulo d;
         tmpIndexVector[m] += 1
         if tmpIndexVector not in indexVectorList[]
            indexVectorList[vertexID][] := tmpIndexVector[];
            verticesInLevel[k][vertexCount] = vertexID;
            vertexID += 1;
            vertexCount += 1;
   numVertsInLevel[k] = vertexCount;
   totalNumVertices += vertexCount;
```

Listing 6.2: Algorithm to partition the vertices of a Pascal's d-simplex into P sets, minimizing inter-set connections while ensuring the numbers of vertices in each set differ by at most 1. The algorithm employs the results of the index vector generation code in Listing 1. Scalar assignment operations indicated using "="; vector assignment operations indicated using ":="; the "==" operator indicates a test for equality.

```
d=M*(K+1)
numVertsInSet[] := vector of P zeros;
verticesInSet[0][0] = 0;
numVertsInSet[0] = 1;
for vertexID = 1 to d
   setID = (vertexID - 1) modulo P;
   verticesInSet[setID][numVertsInSet[setID]] = vertexID;
   numVertsInSet[setID] += 1;
   nextCornerVertexID = vertexID + d;
   for k = 2 to truncationLevel-1
      verticesInSet[setID][numVertsInSet[setID]] = nextCornerVertexID;
      numVertsInSet[setID] += 1;
      nextCornerVertexID += numVertsInLevel[k]
for vertexID = 2*d+1 to totalNumVertices-1
   if vertexID not in verticesInSet[][]
      if P > d and vertexID  <  P+d+1
         setID = vertexID modulo P;
         verticesInSet[setID][numVertsInSet[setID]] = vertexID;
         numVertsInSet[setID] += 1;
      else
         connectionsToSet[] := vector of P zeros;
         for j = 0 to d-1
            tmpIndexVector[] := indexVectorList[vertexID][];
            tmpIndexVector[j] -= 1;
            tmpVertexID = vertex associated with tmpIndexVector
            setID = id of set containing tmpVertexID
            connectionsToSet[setID] += 1;
         connMax[] := all p where connectionsToSet[p] == max(connectionsToSet[]);
         setID = p in connMax[] where numVertsInSet[p] == min(numVertsInSet[]);
         if numVertsInSet[setID] >= ceil(totalNumVertices / P)
            setID = id where numVertsInSet[id] == min(numVertsInSet[]);
         verticesInSet[setID][numVertsInSet[setID]] = vertexID;
         numVertsInSet[setID] += 1;
```

P threads. The communication overhead due to the highly coupled nature of the HEOM means that even with modern symmetric multi-processing (SMP) hardware, however, the ADMs need to be well partitioned to avoid memory contention and maximize use of memory bandwidth available

to each processor.

An algorithm for generating the index vectors **n** of the ADMs and, thus, the vertices of the associated Pascal's d-simplex, is given in Listing 1. The partitioning algorithm (Listing 2) employs the numbering scheme in Listing 1 to assign each vertex to a set such that the number of inter-set edges is minimal whilst ensuring that each set contains almost the same number of vertices. An example of the partitioning of a hierarchy of ADMs associated with a Pascal's 3-simplex is shown in Fig. 6.1. The partitioning algorithm presented here reduces the inter-set connections compared to either block- or cyclic-partitioning schemes often employed in parallel programming. By assigning each set to a separate thread and, crucially, instructing each thread to allocate the memory required to store the ADMs in its set, reduces inter-processor memory contention and dramatically improves the performance of the parallel HEOM integration software PHI.

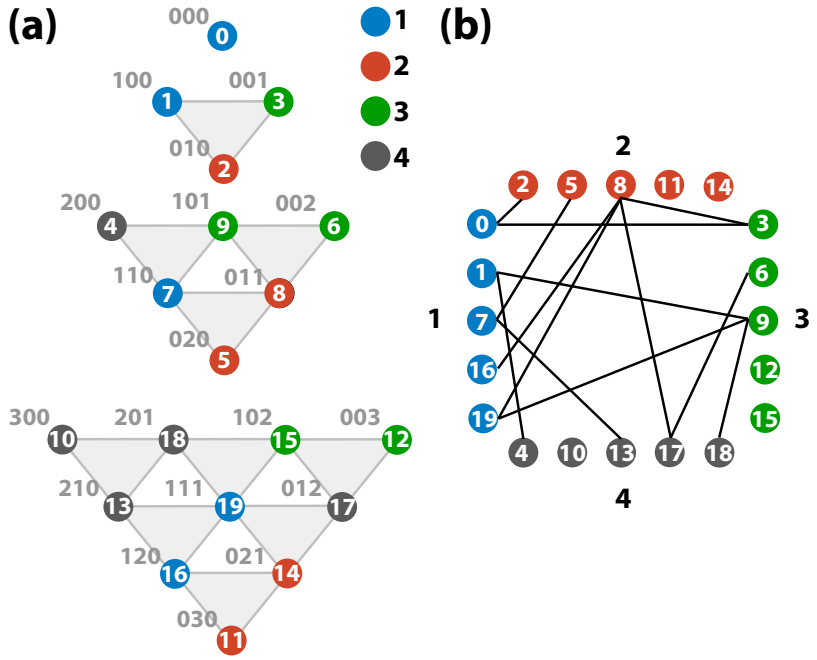

Figure 6.1: Partitioning of a Pascal's 3-simplex into four sets. The partitioning (a) results in each subset containing 5 vertices, with (b) 13 edges crossing between subsets.

6.3 Results

Excitation dynamics is a key process in photosynthetic light harvesting. Excitation needs to be transferred over many nanometers for light energy to be utilized by the cell. Since the excitation life time is rather short, namely only 1 ns, transfer needs to be fast to be efficient. In purple

photosynthetic bacteria, such as *Rps. molischianum*, the needed efficiency is achieved by placing pigment molecules into ring-like structures as shown in Fig. 6.2 and transferring excitation between the ring-like structures. Light energy typically absorbed by light harvesting complex 2 (LH2, B850 ring) [19] is passed by inter-complex excitation transfer to light-harvesting complex 1 (LH1, B875 ring) [39] prior to charge separation at the photosynthetic reaction center [173]. The close packing arrangements and pigment orientations in the ring-like structures result in quantum coherence that enhances excitation transfer between the rings [8].

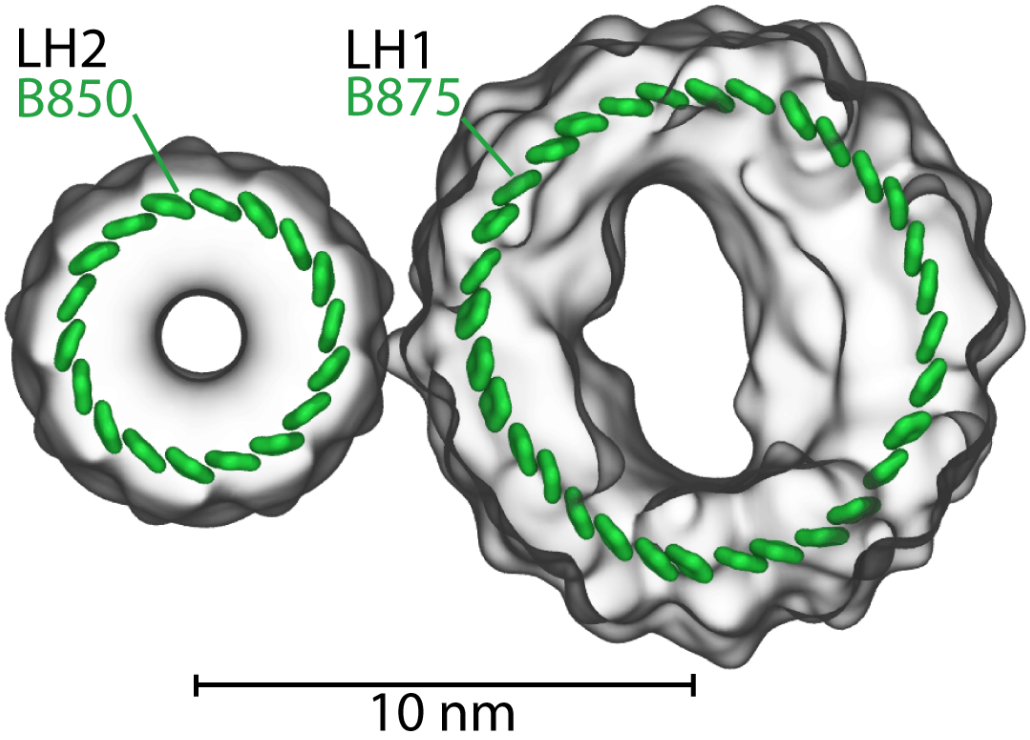

Figure 6.2: Pigment-protein complexes light harvesting complex 2 (LH2) and light harvesting complex 1 (LH1). Shown are the 18 pigments forming the B850 ring of LH2 and the 32 pigments forming the B875 ring of LH1 [19, 39].

We present here the effects of employing different HEOM integration parameters and methods. First, we examine the effect of adaptive timestep integration for a dimer and for an 18-pigment ring, the so-called B850 ring in LH2 [19]. Second, we employ the B850 ring as a model system to investigate the parallel performance of PHI. Finally, the transfer of excitation between the two ring-structures, the B850 ring and the 32-pigment B875 ring in LH1 [39] (shown in Fig. 6.2), is computed.

Effect of integration timestep and method. Below, results are presented to demonstrate the effect of fixed and adaptive timesteps on integration speed and accuracy. First, a model dimer

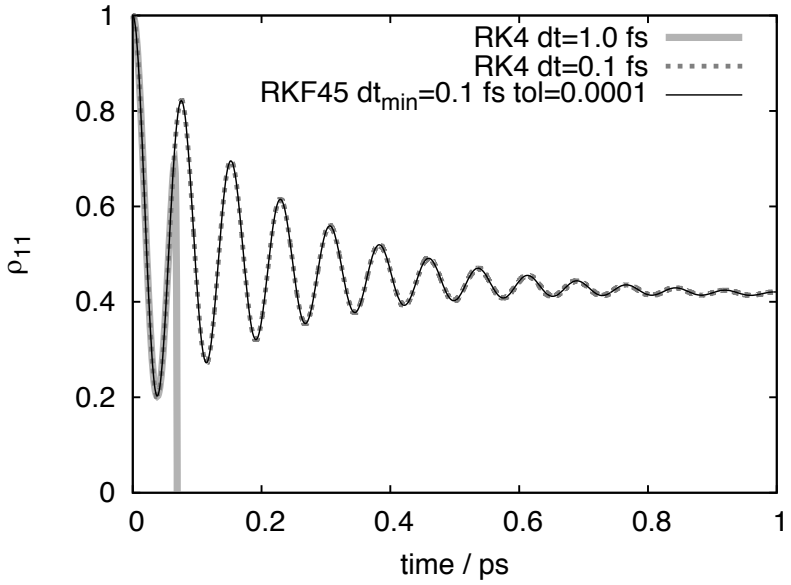

Figure 6.3: Comparison of HEOM integration schemes. Integration on 4 processors (CPU cores) took 0.23 minutes for Runga-Kutta 4 integration using 0.1 fs timesteps, and 0.03 minutes using Runga-Kutta-Fehlberg 4/5 adaptive integration with a minimum timestep of 0.1 fs and a tolerance of 0.0001.

system is employed to highlight the importance of choosing an appropriate timestep. The dimer is specified by $H_S = \Delta E\hat{\sigma}_z + V\hat{\sigma}_x$, where $\Delta E = 100$ cm^{-1}, $V = 200$ cm^{-1}, reorganization energies are $\lambda_1 = \lambda_2 = 50$ cm^{-1}, and response frequencies are $\gamma_1 = \gamma_2 = 1/(0.1$ ps$)$; $\hat{\sigma}_z$ and $\hat{\sigma}_x$ are Pauli matrices [163]. As can be seen from Fig. 6.3, using too large a timestep can rapidly cause integration errors. Fortunately, in such a simple system such gross errors are easy to detect and rectify. For larger systems, however, finding the optimum timestep can be time-consuming. By employing the RKF45 adaptive timestep integration method (see Methods) such effort can be avoided and it becomes much easier to achieve greatly improved performance.

Effect of integration timestep and method. To examine the accuracy and speed of different integration options we consider the case of light excitation of one of the primary absorbing states of the B850 ring of pigments in light harvesting complex 2 (LH2). The excitation dynamics of the 18-pigment B850 ring was previously characterized [1] and calculations are repeated here to investigate the effect of different integration methods. The resulting exciton dynamics is shown in Fig. 6.4 for the reference calculation; Table 6.1 presents the accuracy and computation time of adaptive and non-adaptive integration methods. One can clearly discern that the Shi et al. [60] adaptive filtering dramatically reduces computation time in the case of Runga-Kutta 4 (RK4) integration. Excellent performance can also be achieved using RKF45 adaptive timestep integration, with typically shorter

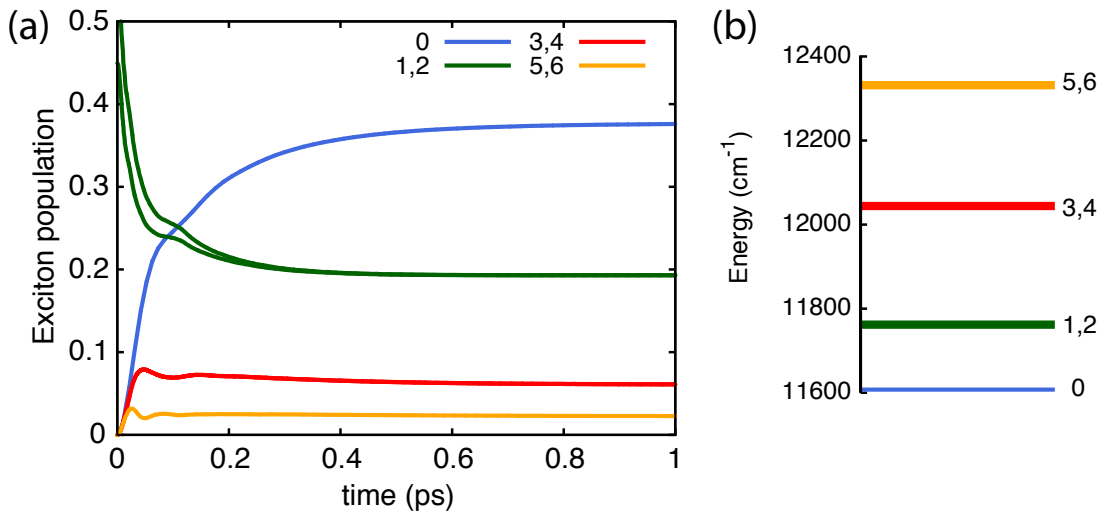

Figure 6.4: Exciton dynamics of the seven lowest-energy exciton states of the B850 ring in LH2 with the initial state given by a super-position of the degenerate 850 nm exciton states 1 and 2. Populations are shown in (a) and energies of associated states in (b).

calculation times and improved accuracy than needed for the other methods listed. Both adaptive methods can be combined for optimal performance as long as the RKF45 tolerance is larger than the ADM filter accuracy, i.e., for $\delta_I > \delta_F$; otherwise longer computation times result. In general, optimal RK4 timestep and ADM filter accuracy both depend on system parameters and, thus, require time-consuming benchmark calculations. Employing RKF45 adaptive timestep integration yields significant performance gains without prior benchmarks.

Parallel performance. Key to employing the HEOM to calculate excitation dynamics in large pigment systems is scalability to many processors. With efficient scaling, the size of problem that can be treated depends only on the size of the computer available and is not limited by the speed of a single processor. To endow *PHI* with optimal scaling capabilities, three steps were taken: (1) memory assignment was changed from being initially assigned to a single large block to being assigned to separate smaller blocks, one for each integration thread; (2) the partitioning of the ADMs was done satisfying minimum inter-thread communication; (3) each thread was assigned to a specific processor. The effect of the three steps, shown in 6.5, is a greater than 3-fold reduction in calculation time when employing 48-cores, and a significantly better scaling compared to cyclic decomposition, a simple and obvious choice, but not an optimal one.

A significant boost in parallel performance is thus gained from the hierarchical partitioning scheme detailed in Listings 1 and 2. The performance saturation seen around 48 cores in 6.5

Table 6.1: Accuracy and performance of different integration methods for calculating excitation dynamics of the B850 pigments of LH2 with parameters and truncation as given in Ref. [1].

integration method	ADM filter† δ_F	integration tolerance‡ δ_I	integration stepsize (fs)	average error‖	calculation time (min)
RK4			0.1	0	920
RK4			1.0	$2.0\text{x}10^{-7}$	91.8
RK4			2.0	$5.4\text{x}10^{-7}$	46.0
RK4	10^{-6}		1.0	$2.0\text{x}10^{-7}$	83.9
RK4	10^{-6}		2.0	$5.5\text{x}10^{-7}$	42.1
RK4	10^{-4}		1.0	$7.8\text{x}10^{-6}$	43.4
RK4	10^{-4}		2.0	$1.1\text{x}10^{-5}$	25.7
RK4	10^{-2}		1.0	$2.7\text{x}10^{-3}$	34.5
RK4	10^{-2}		2.0	$2.9\text{x}10^{-3}$	21.9
RKF45		10^{-6}	1.0→7.5	$6.1\text{x}10^{-7}$	35.6
RKF45		10^{-4}	1.0→7.4	$8.2\text{x}10^{-7}$	33.3
RKF45		10^{-2}	1.0→8.1	$1.2\text{x}10^{-6}$	33.1
RKF45	10^{-6}	10^{-6}	1.0→2.0	$3.3\text{x}10^{-7}$	66.1
RKF45	10^{-6}	10^{-4}	1.0→4.6	$6.7\text{x}10^{-7}$	34.1
RKF45	10^{-6}	10^{-2}	1.0→8.1	$9.9\text{x}10^{-7}$	33.0
RKF45	10^{-4}	10^{-6}	0.6→1.2	$7.8\text{x}10^{-6}$	71.0
RKF45	10^{-4}	10^{-4}	1.0→2.4	$1.1\text{x}10^{-5}$	34.4
RKF45	10^{-4}	10^{-2}	1.0→4.6	$1.5\text{x}10^{-5}$	24.1
RKF45	10^{-2}	10^{-6}	0.3→1.2	$2.0\text{x}10^{-3}$	93.2
RKF45	10^{-2}	10^{-4}	0.7→2.4	$2.8\text{x}10^{-3}$	50.9
RKF45	10^{-2}	10^{-2}	1.0→3.8	$3.3\text{x}10^{-3}$	27.9

† filter constant for Shi et al. adaptive ADM filtering [60].

‡ integration tolerance for Runga-Kutta-Fehlberg 4/5 adaptive integration [174].

‖ $error = (N^2 N_t)^{-1} \sum_n^{N_t} \sum_{i,j}^{N} \left| \rho_{ij}(t_n) - \rho_{ij}^{ref}(t_n) \right|$
is the average absolute error in each element of the system density matrix per timestep.

indicates that inter-processor communication is still a bottleneck and any scheme to reduce this bottleneck will result in further performance improvement. The rapid bandwidth saturation, arising even with the high-bandwidth processor-memory bus (42 GB/sec for the AMD Magny-Cours CPU), suggests that parallel performance on a distributed memory computer is relatively poor.

Excitation transfer between LH2 and LH1. With the improvements in scalability and calculation time for integration of the HEOM described above, one can model excitation transfer between two large pigment-protein complexes, LH2 and LH1 (6.2).

In the photosynthetic light harvesting apparatus of purple bacteria most excitation transfer steps occur between the 18-pigment B850 ring in LH2 and the 32-pigment B875 ring in LH1 [3, 13, 19]. In order to describe this transfer one needs to account for $N = 50$ pigments. Modeling a system of this size is not possible a with single-processor implementation of the HEOM, but requires *PHI*

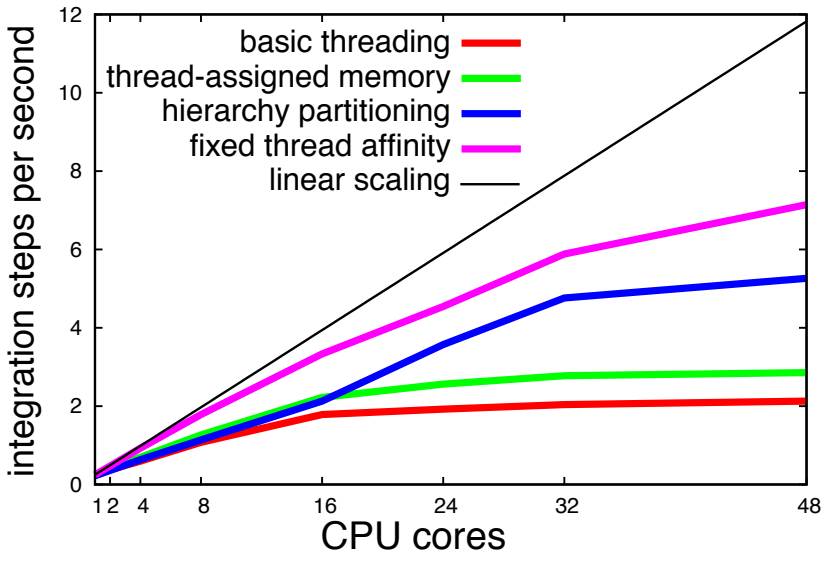

Figure 6.5: Parallel scaling of *PHI* on a 48-core AMD Magny-Cours shared-memory computer running Linux. The system employed for benchmarking is the set of 18 pigments in the B850 ring of LH2 with $L_T = 4$ and $K = 1$. "Basic partitioning" refers to a cyclic partitioning of ADMs and the memory for all ADMs being assigned to a consecutive block; "thread-assigned memory" refers to instructing each thread to perform memory assignment for its set of ADMs in the cycling partitioning scheme; "hierarchy partitioning" refers to employing the partitioning described in Listings 1 and 2 and using thread-assigned memory; "fixed thread affinity" refers to employing the partitioning scheme in Listings 1 and 2, using thread-assigned memory and instructing the operating system's thread scheduler to affix each thread to a particular processor such that no thread migration occurs.

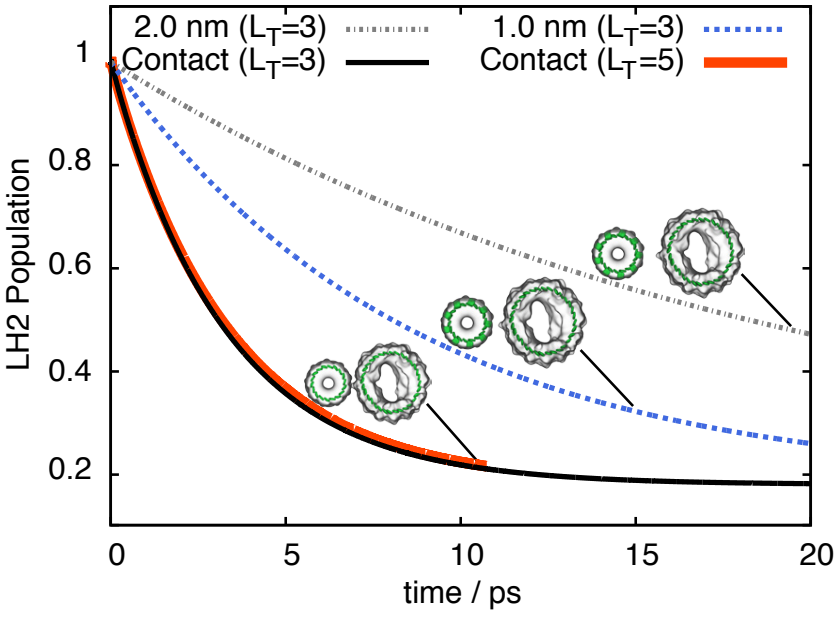

Figure 6.6: Total excited state population of LH2 reflecting inter-complex excitation transfer from LH2 to LH1 at different protein (LH2) - protein (LH1) edge-edge separations.

Table 6.2: Excitation transfer times between the B850 pigments in LH2 and the B875 pigments in LH1.

Hierarchy Truncation	Inter-protein distance (nm)	$\tau_{\mathrm{B850}\rightarrow\mathrm{B875}}$ (ps)	$\tau_{\mathrm{B875}\rightarrow\mathrm{B850}}$ (ps)
$L_T = 5$	0.0	4.1	18.4
$L_T = 3$	0.0	4.0	18.1
$L_T = 3$	1.0	10.4	46.7
$L_T = 3$	2.0	23.6	105

running on a parallel computer.

The parameters describing the B850 and B875 Hamiltonians are taken from Ref. 123, with bath parameters $\lambda_n = \lambda = 180\ \mathrm{cm}^{-1}$ and $1/\gamma_n = 1/\gamma = 100$ fs, a choice that had been shown to reproduce experimental spectra [97]. The population of an initially excited LH2 complex is shown in 6.6 for different truncations and inter-complex separation distances. The results show that TL truncation with a cut-off of $L_T = 3$ yields a population decay close to that of an $L_T = 5$ cut-off. The lower truncation requires 50 MB of memory to store the hierarchy of ADMs and 415 MB of memory for RKF45 integration; the higher truncation requires, however, 12 GB of memory to store the hierarchy of ADMs and 96 GB of memory for RKF45 integration.

The excitation transfer time can be calculated by fitting a simple kinetic model

$$\frac{dP_{\mathrm{B850}}}{dt} = -\frac{P_{\mathrm{B850}}}{\tau_{\mathrm{B850}\rightarrow\mathrm{B875}}} + \frac{1 - P_{\mathrm{B850}}}{\tau_{\mathrm{B875}\rightarrow\mathrm{B850}}} \tag{6.1}$$

describing excitation transfer between B850 and B875 BChl rings (6.6). In our calculations we assumed three separations between the proteins LH1 and LH2 holding the B875 and B850 BChl rings, respectively, namely, edge-edge separations of 2 nm, 1 nm, and 0 nm (contact). In case of contact, transfer times (summarized in 6.2) are $\tau_{\mathrm{B850}\rightarrow\mathrm{B875}} = 5.3$ ps and $\tau_{\mathrm{B875}\rightarrow\mathrm{B850}} = 9.2$ ps; inter-protein separations of 1 nm and 2 nm result in 260% and 590% longer transfer times, respectively.

6.4 Discussion

The hierarchy equations of motion (HEOM) employ a highly coupled set of density matrices to calculate the noise-averaged time evolution of a quantum system coupled to a thermal environment. The large number of matrices required to model multi-pigment systems using the HEOM has restricted the method to systems with only very few pigments. By employing adaptive numerical integration methods (hierarchy filtering of Shi et al. [60] and adaptive timestep integration [174])

and a novel hierarchy partitioning scheme, efficient scaling has been realized. The software implementation available in the program *PHI* can be run on parallel computers allowing the HEOM to be solved for pigment numbers as large as found in biological systems. The performance of *PHI* has been demonstrated here by investigating the accuracy of the adaptive integration methods and by applying *PHI* to model excitation transfer in a 50-pigment system, namely the 18-BChl B850 ring in light harvesting complex 2 (LH2) and 32-BChl B875 ring in light harvesting complex 1 (LH1) of purple photosynthetic bacteria. It was shown that excitation transfer between LH2 and LH1 practically occurs as a Poisson process, i.e., an incoherent hopping process, described by a single exponential decay of excited state population. The excitation transfer times for LH2→LH1 and LH1→LH2 were calculated for direct protein-protein contact, as well as for protein-protein separations of 1 nm and 2 nm. Resulting transfer rates compare well with observations [175] and generalized Förster theory results [46]; the latter agreement should be considered an a posteriori justification of generalized Förster theory.

The efficient parallel implementation of the HEOM makes it possible to model even larger light harvesting systems than studied here such as photosystem 1 and photosystem 2 in cyanobacteria and plants [168, 169], as well as conjugated polymers [171] and pigment dendrimers [172] used in artificial light harvesting. The current implementation of the HEOM would also benefit the calculation of exact quantum dynamics in Wigner space, recently shown to also be computationally challenging due to large memory requirements [176], and is a promising future feature of *PHI*. Additionally, the general applicability of the HEOM lets *PHI* to be used for investigations of other open quantum systems such as charge transfer reactions [177], e.g., in DNA [178] and in the photosynthetic reaction center [179], or coherently coupled spin systems such as those employed in quantum computing [180–182].

It has been established that excitation transfers incoherently between the light harvesting complexes of purple bacteria. The natural question arises that why such strong intra-complex pigment coupling is needed. Strong coupling results in quantum coherence, thus leading to the question of how intra-complex quantum coherence affects inter-complex transfer, and if this is necessary for light harvesting in purple bacteria. This question is addressed in the next Chapter.

Chapter 7

How quantum coherence assists photosynthetic light harvesting

7.1 Introduction

The cooperating pigments display a hierarchical pattern of tight packing and, as a result, exhibit a system of strong and weak electronic interactions that is essential for efficient light harvesting. Within the most strongly interacting groups of pigments, electronic excitation is spread coherently following light absorption [73, 86, 97, 104, 183–187]; however, between pigment groups that are weakly coupled, electronic excitation is shared incoherently, namely through random excitation transfer [1, 13, 105, 136, 188]. The coherent spread is known as exciton dynamics [45, 62, 85, 98] and the incoherent spread as Förster resonant energy transfer (FRET) [7, 98, 107, 189–191]. Photosynthetic light harvesting interweaves both behaviors. Additionally, some pigments fall into an intermediate coupling regime [19, 192–194]. In this regime there is a small amount of coherent spread of electronic excitation, though it is not as well understood how much this influences the efficiency of light harvesting in purple bacteria.

Recently, the role that quantum coherence may play for efficient light harvesting has caught some notoriety (discussed also in a prior Perspective [195]), particularly due to experimental results by Fleming, Engel and Scholes [139, 196–199]. In time-resolved two-dimensional spectroscopy it is possible to see oscillations of exciton state populations, special initial states prepared by carefully chosen laser pulses. The oscillations, lasting up to a few hundred femtoseconds, are attributed to quantum coherence emerging as a result of the initially prepared coherent quantum state and rapid decay (compared to the typical lifetime of excitation in photosynthetic systems of one nanosecond). It is not presently known how much this phenomenon contributes to efficient light harvesting [200].

The quantum coherence that is discussed here arises through strong coupling between bacteriochlorophyll (or chrolophyll) molecules making close contact with each other in the proteins of the photosynthetic apparatus. The focus of this review is to explain how this quantum coherence increases efficiency [201] and architectural flexibility [3] in the light harvesting system of a fundamental photosynthetic life form, namely purple bacteria [5, 173, 202].

7.2 The Reaction Center

The crucial step in photosynthetic light harvesting is the conversion of short-lived excitation energy, resulting from photon absorption, to a form that can be more leisurely used by a living cell, namely that of a charge gradient. This step takes place in a protein complex known as the reaction center (RC). The function of the RC is to receive excitation energy, either by absorbing a solar photon directly, or by excitation transfer from the pigment molecules of nearby light harvesting complexes, and to convert the excitation into a charge-separated state [203–206].

The reaction center contains four bacteriochlorophyll (BChl) pigments and two bacteriopheophytins (akin to a BChl without its magnesium) that absorb light (Fig. 7.1). The light energy absorbed by all six pigments is eventually delivered as an excitation to the central pair of the four BChls, the so-called special pair (SP = Chl_1 + Chl_2, Fig. 7.1). We have included here a generalized view for all photosynthetic systems; thus Chl here is for both chlorophyll and bacteriochlorophyll; and Ph is for both pheophytin and bacteriopheophytin. Light absorbed by pigments with higher electronic excitation energy (Chl_3, Chl_4, Ph_1, Ph_2) leads to coherent (excitonic) oscillations between excited states involving these pigments, as shown in recent experiments [139], before settling into pigments with lower electronic excitation energy, namely Chl_1 and Chl_2 of the SP. The SP initializes charge separation by transferring an excited electron through Chl_3 to a nearby pigment, a bacteriopheophytin (Ph_1). The electron subsequently transfers to a permanently bound molecule of quinone, Q_1, and, finally, to a second, exchangeable quinone, Q_2. The series of electron transfers establish within about a hundred microseconds a charge separated state Q_2^- + SP^+.

A chlorophyll under bright daylight conditions would absorb about 10 photons every second, fewer still in the actual dark habitat of purple bacteria, e.g., at the bottom of ponds. As a result, the RC would be idling most of the time, had biological photosynthesis not evolved a feeder system of pigments. This feeder system comprises mainly of an array of external BChls that funnel electronic excitation to the RC through the FRET mechanism at a high enough rate to keep the RC busy

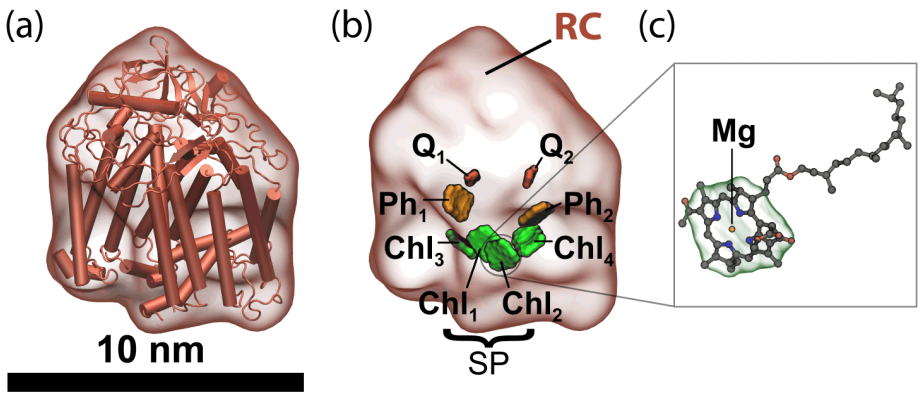

Figure 7.1: (a) Cartoon representation of the photosynthetic reaction center protein with surface outline. (b) Surface outline of the reaction center showing bacteriochlorophylls (Chl_1, Chl_2, Chl_3 and Chl_4) in green, bacteriopheophytins (Ph_1 and Ph_2) in orange and quinones (Q_1 and Q_2) in red. The central bacteriochlorophylls, Chl_1 and Chl_2, form the so-called special pair (SP). (c) Atomic structure of a BChl.

forming charge separated states, keeping the bacterium from starving. However, there is a principle obstacle to this feeder strategy, namely the tendency of BChls too close to the RC to intercept electron transfers towards the $Q_2^- + SP^+$ charge separated state and lead the captured electrons astray.

Fortunately, the rate of electron transfer to BChls has a shorter range than FRET from BChls. This is because electron transfer involves tunneling and decays exponentially with SP-BChl separation, while FRET involves (induced dipole – induced dipole) Coulomb interaction and thus the transfer rate decays as $1/R^6$ [7, 107]. As a result, the latter process has a wider effective range. This range difference permits a corridor around the RC, i.e., a circular region where BChls are far enough to prevent electron transfer away from the RC, yet close enough for efficient energy transfer to the SP [81, 202]. Such a corridor, seen in a wide range of photosynthetic organisms, can be realized apparently only because the SP exhibits a unique FRET potential, without which the FRET range would potentially be shorter than the electron transfer range.

FRET is widely employed in the modern physics laboratory for single molecule measurement of distances [207, 208]. The well known expression for the rate of FRET between a donor (D) and an acceptor (A) molecule, reviewed recently [7], is

$$\text{FRET rate } D \to A \;=\; \frac{2\pi}{\hbar}\,\kappa_{DA}^2\,J_{DA}\,|\mathbf{d}_D|^2|\mathbf{d}_A|^2\,R_{DA}^{-6}, \tag{7.1}$$

Here κ_{DA}^2 is a geometrical factor, usually near unity, accounting for the orientation of the two molecules; J_{DA} is the spectral overlap between donor emission and acceptor absorption; R_{DA} is the center-center distance between donor and acceptor molecules. The key molecular properties

determining the range over which the nanosecond-lived electronic excitation can be transferred are the so-called transition dipole moments $\mathbf{d}_D$ and $\mathbf{d}_A$ characterizing the relevant donor and acceptor emission and absorption processes. Excitation transfer described by Eq. 7.1 occurs between weakly interacting pigments, where the point-dipole approximation is valid (with inter-pigment separations > 1 nm). In the intermediate or strong interaction regimes, more complex formalisms are needed to describe excitation transfer [1, 193]. As such, Eq. 7.1 cannot be used to calculate excitation transfer within any individual light-harvesting complex, but is valid for excitation transfer between complexes [1].

The RC utilizes quantum coherence to achieve a particularly high $|\mathbf{d}_A|$ value to enhance its potential for FRET. For this purpose the RC poses Chl_1 and Chl_2 of the SP within a close (8 Å) Mg–Mg distance of each other such that their excited states are strongly coupled, namely by about 500 cm^{-1} (8066 cm^{-1} = 1 eV) [209]. As a result, electronic excitation of one of the BChls becomes coherently shared among Chl_1 and Chl_2, even under the circumstances of high physiological temperature T ($k_\mathrm{B}T = 209$ cm^{-1}). The excited SP is then found in the states $\widetilde{|\pm\rangle}$

$$\widetilde{|\pm\rangle} = 2^{-\frac{1}{2}} \left(|1\rangle \pm |2\rangle\right) \tag{7.2}$$

where $|1\rangle, |2\rangle$ represent the excited states of Chl_1, Chl_2. The states $\widetilde{|\pm\rangle}$ that share the BChl excitations coherently with each other are called exciton states; according to basic quantum physics, the excitons have an energy difference of 1000 cm^{-1}; as a result the absorption spectrum of the SP is split into two lines. A rather straightforward calculation reveals that, given the sign of the coupling energy and the directions of $\mathbf{d}_1$ and $\mathbf{d}_2$, the transition dipole moment of the lowest energy exciton state is $\sqrt{2}|\mathbf{d}|$, where $|\mathbf{d}| = |\mathbf{d}_1| = |\mathbf{d}_2|$, while the upper exciton state has an almost vanishing transition dipole moment. From this calculation,one can conclude that the lower energy exciton has a stronger FRET potential ($\mathbf{d}_A = \sqrt{2}\mathbf{d}$) with a 12% further FRET range than that a single BChl has ($\mathbf{d}_A = \mathbf{d}$), e.g., a range of 56 Å for the SP instead of only 50 Å for an individual BChl. The comparison assumes that the shifted exciton state has at least the same spectral overlap with feeder BChls as the individual SP BChls. Actually, energy shifts arising through exciton formation in light harvesting systems usually improve spectral overlap (Fig. 7.2).

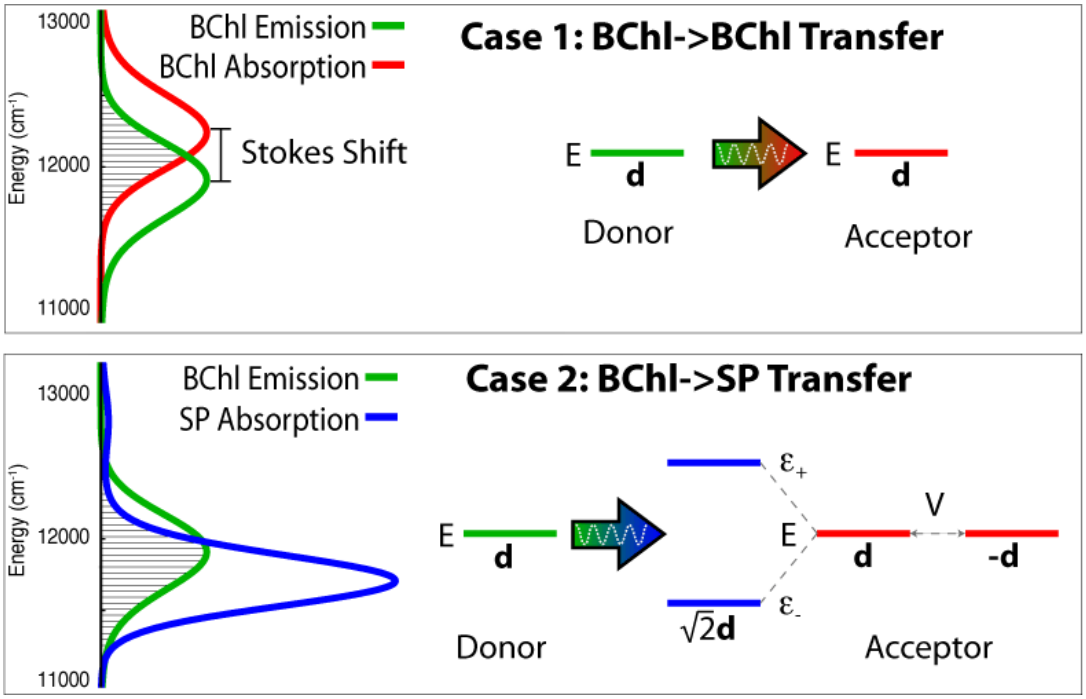

Figure 7.2: When excitation is transferred from a donor bacteriochlorophyll (BChl) to an acceptor BChl, the Stokes shift between the emission and absorption spectra causes an imperfect energy overlap, as shown in Case 1 (see filled area illustrating overlap J_{DA}). This results in a reduced rate of excitation transfer. The reaction center can counter the reduced overlap by introducing a second acceptor BChl that is strongly coupled to the first, forming the special pair (SP). Strong coupling, accounted for by an interaction energy of $V = 500$ cm^{-1} (V is determined in Ref. [21]), coherently spreads excitation between the two acceptor SP BChls, shifting also the SP exciton energies from the single BChl excited state energy E to energies ε_- and ε_+. This shift alters the absorption spectrum, as shown in Case 2, and accordingly increases the overlap, J_{DA}, between emission (green line) and absorption (blue line) spectra (see filled area). Furthermore, due to the anti-parallel orientation of the SP BChl's transition dipole moments, the lower energy exciton state $\widetilde{|-\rangle}$ attains a transition dipole moment of $\mathbf{d}_A = \sqrt{2}\mathbf{d}$. The combination of better spectral overlap J_{DA} and a stronger $\mathbf{d}_A$ value increases the rate of excitation transfer for Case 2 over that of Case 1.

7.3 Light Harvesting Complex 1

The purple bacterial light harvesting system, indeed, places feeder BChls in the expected ring-shaped corridor around the SP of the RC. The feeder system is an awesome structure [39], having 32 BChls stacked as close as feasible in the ring as shown in Fig. 7.3. The BChls are held by a protein complex, called light harvesting complex 1 (LH1), that is made of 32 separate transmembrane α-helices forming a scaffold for the BChls and 16 carotenoids; the latter important light harvesting partners [21] are not further considered here.

The 32 BChls and 16 carotenoids greatly increase the cross section for light absorption of the RC, but the BChl ring, known as the B875 ring for its absorption peak at 875 nm, should be far enough away from the SP to prevent electron tunneling from the excited SP, but close enough to transfer electronic excitation faster than the excitation lifetime, τ_0, of a nanosecond; an acceptable

transfer time, τ_1, is 50 ps or less (corresponding to a transfer efficiency of $\tau_0/(\tau_0+\tau_1) = 95$ %). To reach such quick FRET does not only require a large FRET potential on the SP side, but also on the side of the LH1 BChl ring.

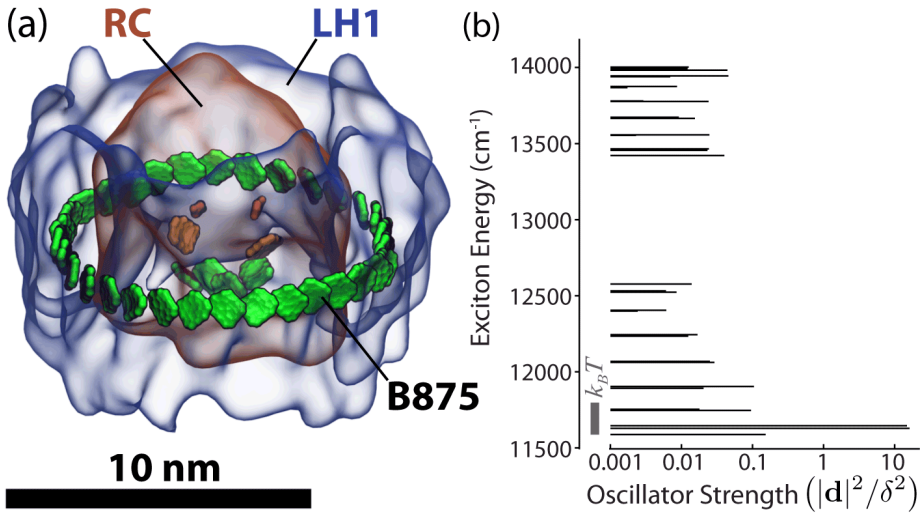

Figure 7.3: (a) Light harvesting complex 1 (LH1) surrounding the photosynthetic reaction center. The 32 LH1 bacteriochlorophylls forming the B875 ring are shown in green. (b) Exciton spectrum and oscillator strengths of the B875 ring. The transition dipole moment of a single bacteriochlorophyll is given by $\delta = 6.3$ Debye. The gray bar indicates the amount of thermal energy at 300 Kelvin.

The BChls in the LH1 ring are packed together nearly as tightly as the two SP BChls with an average Mg–Mg distance of 1 nm. The tight packing results again in strong (compared to $k_{\mathrm{B}}T$) electronic interaction between nearest-neighbors, such that excitation is coherently shared between the LH1 BChls despite thermal disorder [72, 97, 187, 201, 210, 211], just as it is in the SP of the RC. The coherent spread of excitation over single BChl states $|j\rangle$, $j = 1, \cdots, 32$, is described by exciton states $\overline{|\mu\rangle} = \sum_j \alpha_{\mu j} |j\rangle$ for $\mu = 1, \cdots, 32$, where $\alpha_{\mu j}$ are the expansion coefficients of the exciton states in the site basis and are calculated from the B875 Hamiltonian, as shown in Ref. [19].

The exciton spectrum of the B875 ring is shown in Fig. 7.3 along with the squared transition dipole moment values of each state, the so-called oscillator strengths. One can recognize that the exciton energies are spread over 2450 cm^{-1}, a value that exceeds $k_{\mathrm{B}}T$ 12-fold, such that thermalization among the exciton states, which arises within 1-2 picoseconds after light absorption into the B875 ring [1], leads to a significant population gradient among the exciton states [210, 211].

After fast thermalization, the B875 excitons $\overline{|\mu\rangle}$ transfer their energy to the SP states $\widetilde{|\nu\rangle}$ as described by a generalization of the FRET rate expression (Eq. 7.1)

$$k_{\mu\nu} = \frac{2\pi}{\hbar} V_{\mu\nu}^2 J_{\mu\nu} \tag{7.3}$$

where $V_{\mu\nu}$ is the interaction energy between LH1 exciton state $\overline{|\mu\rangle}$ and SP exciton state $\widetilde{|\nu\rangle}$ and $J_{\mu\nu}$ is the two states' spectral overlap density [7, 98, 190, 191]. Accounting for the thermal populations p_μ of the LH1 exciton states, the overall transfer rate is

$$k_{LH1\to SP} = \sum_{\mu\in LH1}\sum_{\nu\in SP} p_\mu k_{\mu\nu}. \tag{7.4}$$

Calculation of the FRET rate $k_{LH1\to SP}$, accounting for the actual geometry of the LH1-RC complex shown in Fig. 7.3, yields a value of 1/(30 ps) which is high enough compared to the excitation decay rate of 1/ns. The corresponding FRET rate for a single LH1 BChl and a single SP Chl (average taken over Chl_1 and Chl_2) is calculated to be 1/(480 ps). The comparison shows that quantum coherence greatly accelerates LH1 $\to$ SP FRET, making it feasible to extend light harvesting capacity by engaging 32 LH1 BChls.

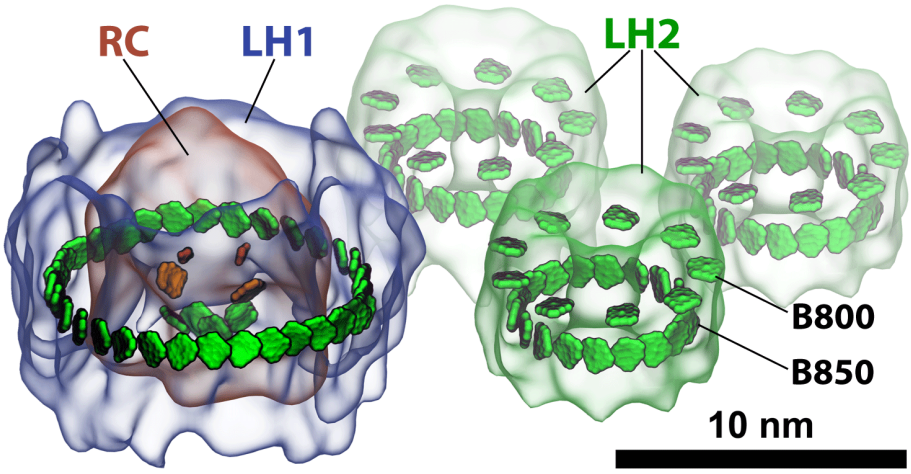

Figure 7.4: One LH1-RC complex with three LH2 complexes nearby. The upper and lower rings of BChls in LH2 are the B800 and B850 rings, respectively.

7.4 Light Harvesting Complex 2

It turns out that in the dark habitat of many purple bacteria, even the LH1 pigments do not feed enough excitation to the RC for cells to thrive. Purple bacteria evolved a further pigment pool to absorb photons more completely and increase excitation feed to the RC. For this purpose the bacteria simply extend the exciton mechanism described for LH1. One might guess at this point that the bacteria simply add more "empty" LH1 rings next to the LH1-RC complex, but that solution would leave gaping holes in the middle of the additional LH1 rings, i.e., would not amount to a

maximal pigment density. Also, LH1 rings are only stable when they surround an RC. Instead, the bacteria add around the LH1-RC complexes smaller, stable ring proteins. These proteins are highly homologous to the LH1 protein, but they form rings of only about half the size. The smaller rings, called light harvesting complex 2 (LH2) and shown in Fig. 7.4, involve a scaffold of 18 (in some cases 16) separate trans-membrane helices with 27 (24) BChls and 9 (8) carotenoids [17, 18].

The LH2 BChls form actually two BChl rings, a B850 ring and a B800 ring, named after their absorption peaks at 850 nm and 800 nm [212]. The B850 ring contains 18 (16) BChls that are, in the same fashion as the BChls of the B875 ring, tightly packed with strong nearest-neighbor interactions. The B800 BChls, also seen in Fig. 7.4, are not spaced as tightly and, as a result, do not form thermally stable excitons. Indeed, they also do not contribute to long-range FRET, their role being to add more absorption power; with an orientation perpendicular to the B850 BChls, the B800 BChls optimally absorb photons polarized in the membrane plane. Once a B800 BChl absorbs light, it transfers the excitation quickly (within 1 ps [213]) to the B850 ring for further excitation transfer. The coupling between B800-carotenoid couplings and the B850-carotenoid couplings fall into an intermediate regime [19, 214], enhancing the rate of excitation transfer from B800 to B850 BChls [19, 123]. Although the B800 to B850 transfer remains to be fully understood [193, 215, 216], it's influence on light harvesting efficiency, due to the short B800 to B850 transfer time, is simply optimal and cannot be improved further..

Quantum coherence of the B850 excitons benefits LH2→LH2 and LH2→LH1 FRET in the same way as it benefits LH1→RC FRET [93, 105]. In fact, one can employ the same description, using expressions (Eq. 7.3, Eq. 7.4), except that indices μ refer to LH2 excitons and ν to LH1 excitons. Calculations [3] show that through exciton coherence the FRET rates increase so much that large LH2→LH1 and LH2→LH2 transfer distances become feasible, i.e., large distances with FRET rates higher than 1/(20 ps). The distances correspond to a maximum edge-to-edge separation between LH1 and LH2 proteins of 12 Å and between two LH2s of 8 Å. Such distances and short transfer times make it possible for cells to add, depending on the ambient light level, numerous LH2s to LH1-RC complexes into a functioning cellular membrane, in fact, up to five or more LH2s for each LH1-RC. Due to excitonic coupling, FRET rates become high enough to ensure that the energy of every photon absorbed reaches a RC within about 100 ps, achieving thus an efficiency of 90 %. To understand how such light harvesting systems are engineered one needs to employ experimental imaging methodologies and theoretical descriptions that work at the level of hundreds of proteins.

7.5 Chromatophores

Purple bacteria assemble in their cellular membrane about a hundred light harvesting proteins, typically 50-100 LH2s and 10-20 LH1-RC complexes, which achieve light driven charge separated states in the RCs [3, 13, 188]. The quinone Q_2 gets charged twice, sequentially, by electron transfer from the extracellular to the intracellular side of the membrane while attracting two protons from the intracellular side, forming hydroquinone, $Q \rightarrow QH_2$. The QH_2 leaves the RC and diffuses through the membrane to proteins called Cyt bc_1 complex, usually present at a 2:1 ratio of LH1-RC to bc1 complex [217]. In the bc_1 complex, electrons and protons are taken from the quinone; the electrons are returned to the RC through a shuttling protein called cytochrome c_2; the protons are released to the extracellular side, forming thus a membrane potential of the same polarity as the electrons did before.

The supra-molecular assembly of membrane proteins thus described is called the photosynthetic chromatophore. A purple bacterial cell may contain over a thousand chromatophores [218], each containing over 3000 BChls [13]. In many species, chromatophores form spherical vesicles such as the one shown in Fig. 7.5 [3]. The chromatophore is an amazing biological device whose primary function is light harvesting and the formation of a membrane potential. This function can be traced in great detail across many time scales beginning with the capture and sub-picosecond transfer of light energy among its constituent pigments.

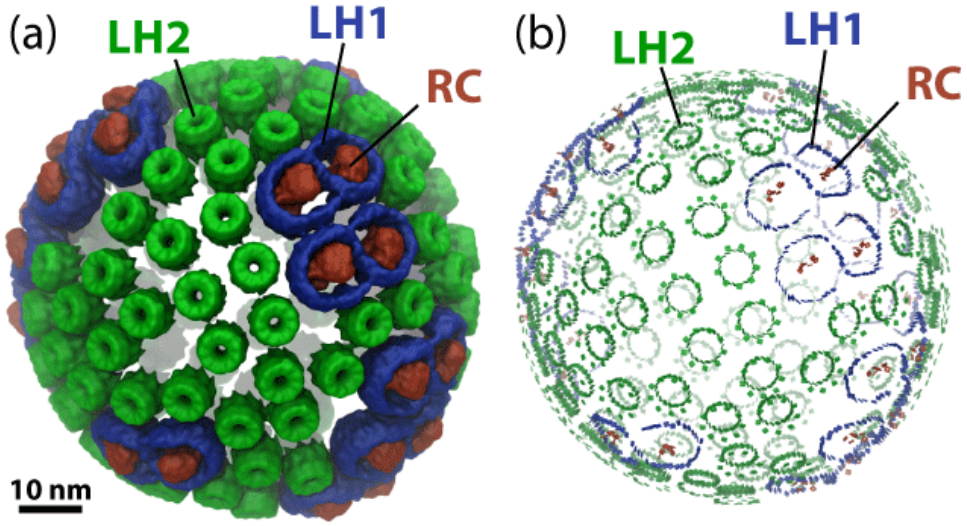

Figure 7.5: Spherical chromatophore from *Rhodobacter sphaeroides* showing (a) proteins and (b) bacteriochlorophylls. Reaction center (RC) is shown in red, light harvesting complex 1 (LH1) in blue and light harvesting complex 2 (LH2) in green. LH1-RC complexes form figure-8 shaped dimers in *Rhodobacter sphaeroides* [3].

The overall efficiency of light harvesting in the chromatophore can be calculated by combining

four processes in a so-called stochastic rate equation: (i) light absorption; (ii) excitation migration as described by the FRET rates in Eqs. (7.1, 7.3, 7.4); (iii) electron transfer in the RC; (iv) fluorescence or so-called internal conversion that lead to the finite nanosecond life time of BChl electronic excitation. Process (iv) limits the efficiency of light harvesting: the longer the time from light absorption to electron transfer at the RC, the less the efficiency, due to loss of excitation to fluorescence or internal conversion. The solution of the stochastic rate equation [3, 13, 188] permits one to calculate various characteristics of the chromatophore, in particular its light harvesting efficiency of 90%. It should be noted that optimal light harvesting efficiency is not the only relevant constraint to give a photosynthetic organism a competitive advantage. For example, the organism also needs to protect itself from photo-oxidative damage, especially under high light conditions, by dissipating excitation energy across its whole light harvesting apparatus rather than only in the RCs.

The chromatophore of purple bacteria displays a remarkable simplicity compared to its evolutionary competitors in cyanobacteria, algae, and plants; the latter usurped the biosphere by evolving a more complex photosynthetic apparatus that feeds photo-excited electrons into various cellular processes, e.g., synthesis of sugar, splitting water into oxygen gas, electrons, and protons (the purple bacteria just circulate electrons in the chromatophore). Nonetheless, by studying the chromatophore, the simplest known incarnation of biological photosynthesis, the key features of the quantum biology of light harvesting in all of biological photosynthesis are revealed, in particular the role of quantum coherence.

The role of quantum coherence in purple bacteria light harvesting was first established in 1997 [19]. Quantum coherence manifests itself in exciton states of BChl clusters that bunch up transition dipole moments of individual BChls. Additionally, quantum coherence shifts energy levels and improves resonance (spectral overlap) between BChl clusters. As a result, quantum coherence critically increases FRET rates, which allows additional pigments, placed a distance away from the RC, to capture additional photons and rapidly feed excitation energy to the SP for conversion into an electronic gradient before significant loss of energy occurs. Quantum coherence thus also allows antenna protein complexes to be spaced far enough apart that other processes, such as diffusion of quinone molecules in the chromatophore membrane, can proceed unhindered, whilst maintaining remarkably high light harvesting efficiency.

The chromatophore is an amazing opto-electronic device. It amasses pigments, in a hierarchical pattern, as shown in Fig. 7.5b, exploiting quantum coherence in a beautiful and elegant manner.

Chapter 8

Conclusions

Photosynthetic light harvesting is efficient, clean and occurs in many different ways in nature. Purple photosynthetic bacteria contain some of the simplest biological machine capable of efficiently harvesting sunlight. With the advent of large-memory, multi-processor parallel computers it is possible to employ the most advanced theoretical methods to describe the quantum events responsible for efficient light harvesting. It has been shown that the software PHI, developed for the work presented in this Dissertation, can be used to model excitation dynamics of many-pigment systems.

Generalized Förster theory was used in prior studies of excitation transfer between the pigment-complexes in purple bacteria. Generalized Förster theory was used as much out of necessity (more advanced methods were too computationally expensive) as out of the assumption that excitation transfer occurs incoherently and that exciton states could be approximated by the diagonal states of the system Hamiltonian, i.e., the so-called zero Kelvin exciton states that don't take into account the influence of environmental fluctuations. Testing these assumptions requires the use of an advanced theory of quantum dynamics that neither employs perturbative approximations nor makes assumptions about the quantum nature of the system. The hierarchy equations of motion is such a theory and was used to examine excitation dynamics within and between light harvesting complex 2 (LH2), light harvesting complex 1 (LH1) and reaction center (RC) complexes of purple bacteria.

In the case of LH2 and LH1, the large pigment numbers lead to only minor corrections to the exciton states arising from strong system-environment coupling. Despite also strong inter-exciton interaction arising from the anti-aligned pigment arrangements in LH2 and LH1, the strong system-environment coupling leads to incoherent inter-complex exciton transfer. Taken together, these results show that generalized Förster theory can adequately account for inter-complex exciton transfer.

The RC, in contrast to LH2 and LH1, has relatively weaker system-environment coupling and fewer pigment numbers. Despite the weaker system-environment coupling in the RC, the LH1-RC exciton coupling is still weaker, thus resulting in incoherent transfer between the complexes.

Furthermore, the weak system-environment coupling results in high inter-complex exciton transfer rates, particularly in the case of RC→LH1 back-transfer, which is important for protecting absorbed photon energy from loss at charged RCs.

Excitons in purple bacteria are coherently delocalized over a number of pigments in LH2, LH1 and RC complexes. The resulting inter-pigment quantum coherence within a complex has a significant benefit for photosynthetic light harvesting. Due to the anti-aligned ring-like arrangement of transition dipole moments, pigment oscillator strength is gathered in one or two exciton states. This purely quantum mechanical effect leads to greatly improved inter-complex exciton transfer rates. Thus, photon energy absorbed far from a RC can be rapidly transported there long before its loss to the environment.

There are many questions that remain to be answered. In the case of light harvesting in purple bacteria, the effect of static disorder needs to be quantified. This was done in the present work only for the case of inter-dimer exciton transfer due to the significant computational cost involved in performing density matrix evolutions on thousands of realizations of disorder. In addition to including static disorder, the effect of more realistic spectral densities for the pigments in purple bacteria needs to be investigated.

Light harvesting in other organisms, while employing similar pigments molecules, utilize different antenna structures and methods to funnel excitation to the RC. The HEOM is an ideal method to investigate the physical principles underlying light harvesting in other organisms. Such investigations require, however, the determination of many system Hamiltonian matrix elements, and system-environment coupling parameters (spectral densities), but will undoubtedly yield great insights into other methods that Nature has found to efficiently harvest solar energy.

References

[1] Strümpfer, J. & Schulten, K. (2009). Light harvesting complex II B850 excitation dynamics. *J. Chem. Phys.*, **131**, 225101. (9 pages).

[2] Hsin, J., Chandler, D. E., Gumbart, J., Harrison, C. B., Sener, M., Strumpfer, J. & Schulten, K. (2010). Self-assembly of photosynthetic membranes. *ChemPhysChem*, **11**, 1154–1159.

[3] Sener, M., Strumpfer, J., Timney, J. A., Freiberg, A., Hunter, C. N. & Schulten, K. (2010). Photosynthetic vesicle architecture and constraints on efficient energy harvesting. *Biophys. J.*, **99**, 67–75.

[4] Hsin, J., Strümpfer, J., Sener, M., Qian, P., Hunter, C. N. & Schulten, K. (2010). Energy transfer dynamics in an RC-LH1-PufX tubular photosynthetic membrane. *New J. Phys.*, **12**, 085005. (19 pages).

[5] Strümpfer, J., Hsin, J., Sener, M., Chandler, D. & Schulten, K. (2011). The light-harvesting apparatus in purple photosynthetic bacteria, introduction to a quantum biological device. In B. Roux, ed., *Molecular Machines*, chapter 2, 19–48. World Scientific Press.

[6] Strümpfer, J. & Schulten, K. (2011). The effect of correlated bath fluctuations on exciton transfer. *J. Chem. Phys.*, **134**, 095102. (9 pages).

[7] Sener, M., Strümpfer, J., Hsin, J., Chandler, D., Scheuring, S., Hunter, C. N. & Schulten, K. (2011). Förster energy transfer theory as reflected in the structures of photosynthetic light harvesting systems. *ChemPhysChem*, **12**, 518–531.

[8] Strumpfer, J., Sener, M. & Schulten, K. (2012). How quantum coherence assists photosynthetic light harvesting. *J. Phys. Chem. Lett.*, **3**, 536–542.

[9] Strümpfer, J. & Schulten, K. (2012). Open quantum dynamics calculations with the hierarchy equations of motion on parallel computers. *J. Chem. Theor. Comp.* In press.

[10] Strümpfer, J. & Schulten, K. (2012). Excited state dynamics in photosynthetic reaction center and light harvesting complex 1. *J. Chem. Phys.* In press.

[11] Humphrey, W., Dalke, A. & Schulten, K. (1996). VMD – Visual Molecular Dynamics. *J. Mol. Graphics*, **14**, 33–38.

[12] Blankenship, R. E., Tiede, D. M., Barber, J., Brudvig, G. W., Fleming, G., Ghirardi, M., Gunner, M. R., Junge, W., Kramer, D. M., Melis, A., Moore, T. A., Moser, C. C., Nocera, D. G., Nozik, A. J., Ort, D. R., Parson, W. W., Prince, R. C. & Sayre, R. T. (2011). Comparing photosynthetic and photovoltaic efficiencies and recognizing the potential for improvement. *Science*, **332**, 805–809.

[13] Sener, M. K., Olsen, J. D., Hunter, C. N. & Schulten, K. (2007). Atomic level structural and functional model of a bacterial photosynthetic membrane vesicle. *Proc. Natl. Acad. Sci. USA*, **104**, 15723–15728.

[14] Ben-Shem, A., Frolow, F. & Nelson, N. (2003). Crystal structure of plant photosystem I. *Nature*, **426**, 630–635.

[15] Sauer, K. (1975). Primary events and the trapping of energy. In Govindjee, ed., *Bioenergetics of Photosynthesis*, 115–181. Academic Press.

[16] Knox, R. S. (1977). Photosynthetic efficiency and exciton transfer and trapping. In J. Barber, ed., *Primary Processes of Photosynthesis*, 55–97. Elsevier, Amsterdam.

[17] McDermott, G., Prince, S. M., Freer, A. A., Hawthornthwaite-Lawless, A. M., Papiz, M. Z., Cogdell, R. J. & Isaacs, N. W. (1995). Crystal structure of an integral membrane light-harvesting complex from photosynthetic bacteria. *Nature*, **374**, 517–521.

[18] Koepke, J., Hu, X., Muenke, C., Schulten, K. & Michel, H. (1996). The crystal structure of the light harvesting complex II (B800-850) from *Rhodospirillum molischianum*. *Structure*, **4**, 581–597.

[19] Hu, X., Ritz, T., Damjanović, A. & Schulten, K. (1997). Pigment organization and transfer of electronic excitation in the purple bacteria. *J. Phys. Chem. B*, **101**, 3854–3871.

[20] Clegg, R. M., Sener, M. & Govindjee (2010). From förster resonance energy transfer to coherent resonance energy transfer and back (invited paper). In *Optical Biopsy VII, edited by Robert R. Alfano, Proceedings of SPIE, Vol 7561*, 7561–12. SPIE, Bellingham, WA.

[21] Damjanović, A., Ritz, T. & Schulten, K. (1999). Energy transfer between carotenoids and bacteriochlorophylls in a light harvesting protein. *Phys. Rev. E*, **59**, 3293–3311.

[22] Pfennig, N. (1967). Photosynthetic bacteria. *Annu. Rev. Med.*, **21**, 285–324.

[23] Pfennig, N. (1969). *Rhodopseudomonas acidophila*, sp. n., a new species of the budding purple nonsulfur bacteria. *J. Bacteriol.*, **99**, 597–602.

[24] Hu, X. & Schulten, K. (1997). How nature harvests sunlight. *Physics Today*, **50**, 28–34.

[25] Roszak, A. W., Howard, T., Southall, J., Gardiner, A. T., Law, C. J., Isaacs, N. W. & Cogdell, R. J. (2003). Crystal structure of the RC-LH1 core complex from *Rhodopseudomonas palustris*. *Science*, **302**, 1969–1972.

[26] Fotiadis, D., Qian, P., Philippsen, A., Bullough, P. A., Engel, A. & Hunter, C. N. (2004). Structural analysis of the reaction center light-harvesting complex I photosynthetic core complex of *Rhodospirillum rubrum* using atomic force microscopy. *J. Biol. Chem.*, **279**, 2063–2068.

[27] Qian, P., Hunter, C. N. & Bullough, P. A. (2005). The 8.5 Å projection structure of the core RC-LH1-PufX dimer of *Rhodobacter sphaeroides*. *J. Mol. Biol.*, **349**, 948–960.

[28] Qian, P., Bullough, P. A. & Hunter, C. N. (2008). Three-dimensional reconstruction of a membrane-bending complex: The RC-LH1-PufX core dimer of *Rhodobacter sphaeroides*. *J. Biol. Chem.*, **283**, 14002–14011.

[29] Hsin, J., Gumbart, J., Trabuco, L. G., Villa, E., Qian, P., Hunter, C. N. & Schulten, K. (2009). Protein-induced membrane curvature investigated through molecular dynamics flexible fitting. *Biophys. J.*, **97**, 321–329.

[30] Sener, M. K., Hsin, J., Trabuco, L. G., Villa, E., Qian, P., Hunter, C. N. & Schulten, K. (2009). Structural model and excitonic properties of the dimeric RC-LH1-PufX complex from Rhodobacter sphaeroides. *Chem. Phys.*, **357**, 188–197.

[31] Scheuring, S., Francia, F., Busselez, J., Melandris, B. A., Rigaud, J.-L. & Levy, D. (2004). Structural role of PufX in the dimerization of the photosynthetic core complex of *Rhodobacter sphaeroides*. *J. Biol. Chem.*, **279**, 3620–3626.

[32] Scheuring, S., Busselez, J. & Lévy, D. (2005). Structure of the dimeric PufX-containing core complex of *Rhodobacter blasticus* by *in situ* atomic force microscopy. *J. Biol. Chem.*, **280**, 1426–1431.

[33] Jungas, C., Ranck, J., Rigaud, J., Joliot, P. & Verméglio, A. (1999). Supramolecular organization of the photosynthetic apparatus of *Rhodobacter sphaeroides*. *EMBO J.*, **18**, 534–542.

[34] Busselez, J., Cottevielle, M., Cuniasse, P., Gubellini, F., Boisset, N. & Lévy, D. (2007). Structural basis for the PufX-mediated dimerization of bacterial photosynthetic core complexes. *Structure*, **15**, 1674–1683.

[35] Frese, R., Olsen, J., Branvall, R., Westerhuis, W., Hunter, C. & van Grondelle, R. (2000). The long-range supraorganization of the bacterial photosynthetic unit: A key role for PufX. *Proc. Natl. Acad. Sci. USA*, **97**, 5197–5202.

[36] Siebert, C. A., Qian, P., Fotiadis, D., Engel, A., Hunter, C. N. & Bullough, P. A. (2004). Molecular architecture of photosynthetic membranes in *Rhodobacter sphaeroides*: the role of PufX. *EMBO J.*, **23**, 690–700.

[37] Scheuring, S. (2006). AFM studies of the supramolecular assembly of bacterial photosynthetic core-complexes. *Curr. Opin. Chem. Biol.*, **10**, 387–393.

[38] Hsin, J., Chipot, C. & Schulten, K. (2009). A glycophorin A-like framework for the dimerization of photosynthetic core complexes. *J. Am. Chem. Soc.*, **131**, 17096–17098.

[39] Hu, X. & Schulten, K. (1998). A model for the light-harvesting complex I (B875) of *Rhodobacter sphaeroides*. *Biophys. J.*, **75**, 683–694.

[40] Chandler, D., Hsin, J., Harrison, C. B., Gumbart, J. & Schulten, K. (2008). Intrinsic curvature properties of photosynthetic proteins in chromatophores. *Biophys. J.*, **95**, 2822–2836.

[41] Deisenhofer, J. & Michel, H. (1987). In J. Breton & A. Vermeglio, eds., *The crystal structure of the photosynthetic reaction center from Rhodopseudomonas viridis*, The photosynthetic bacterial reaction center: Structure and dynamics, 1–3. Plenum Press, London.

[42] Jordan, P., Fromme, P., Witt, H. T., Klukas, O., Saenger, W. & Krauß, N. (2001). Three-dimensional structure of cyanobacterial photosystem I at 2.5 Å resolution. *Nature*, **411**, 909–917.

[43] Guskov, A., Kern, J., Gabdulkhakov, A., Broser, M., Zouni, A. & Saenger, W. (2009). Cyanobacterial photosystem II at 2.9- resolution and the role of quinones, lipids, channels and chloride. *Nat. Struct. Mol. Biol.*, **16**, 334–342.

[44] Tanimura, Y. & Kubo, R. (1989). Two-time correlation functions of a system coupled to a heat bath with a Gaussian-Markoffian interaction. *J. Phys. Soc. Jpn.*, **58**, 1199–1206.

[45] Ishizaki, A. & Fleming, G. R. (2009). Unified treatment of quantum coherent and incoherent hopping dynamics in electronic energy transfer: Reduced hierarchy equation approach. *J. Chem. Phys.*, **130**, 234111–10.

[46] Hu, X., Ritz, T., Damjanović, A., Autenrieth, F. & Schulten, K. (2002). Photosynthetic apparatus of purple bacteria. *Quart. Rev. Biophys.*, **35**, 1–62.

[47] Şener, M. & Schulten, K. (2005). Physical principles of efficient excitation transfer in light harvesting. In D. L. Andrews, ed., *Energy Harvesting Materials*, 1–26. World Scientific, Singapore.

[48] Ishizaki, A. & Fleming, G. R. (2009). Theoretical examination of quantum coherence in a photosynthetic system at physiological temperature. *Proc. Natl. Acad. Sci. USA*, **106**, 17255.

[49] Cardeira, A. O. & Leggett, A. J. (1983). Quantum tunnelling in a dissipative system. *J. Ann. Phys.(N.Y.)*, **149**, 374–456.

[50] May, V. & Kühn, O. (2000). *Charge and Energy Transfer Dynamics in Molecular Systems*. WILEY-VCH, Berlin.

[51] Prior, J., Chin, A., Huelga, S. & Plenio, M. (2010). Efficient simulation of strong system-environment interactions. *Phys. Rev. Lett.*, **105**, 50404.

[52] Chin, A., Rivas, Á., Huelga, S. & Plenio, M. (2010). Exact mapping between system-reservoir quantum models and semi-infinite discrete chains using orthogonal polynomials. *J. Math. Phys.*, **51**, 092109.

[53] Topaler, M. & Makri, N. (1993). System-specific discrete variable representations for path integral calculations with quasi-adiabatic propagators. *Chem. Phys. Lett.*, **210**, 448–457.

[54] Ishizaki, A. & Tanimura, Y. (2005). Quantum dynamics of system strongly coupled to Low-Temperature colored noise bath: Reduced hierarchy equations approach. *J. Phys. Soc. Jpn.*, **74**, 3131–3134.

[55] Tanimura, Y. (1990). Nonperturbative expansion method for a quantum system coupled to a harmonic-oscillator bath. *Phys. Rev. A*, **41**, 6676–6687.

[56] Yan, Y., Yang, F., Liu, Y. & Shao, J. (2004). Hierarchical approach based on stochastic decoupling to dissipative systems. *Chem. Phys. Lett.*, **395**, 216–221.

[57] Xu, R. X., Cui, P., Li, X. Q., Mo, Y. & Yan, Y. J. (2005). Exact quantum master equation via the calculus on path integrals. *J. Phys. Chem.*, **122**, 041103.

[58] Schröder, M., Kleinekathöfer, U. & Schreiber, M. (2006). Calculation of absorption spectra for light-harvesting systems using non-Markovian approaches as well as modified redfield theory. *J. Chem. Phys.*, **124**, 084903.

[59] Xu, R. X. & Yan, Y. J. (2007). Dynamics of quantum dissipation systems interacting with bosonic canonical bath: Hierarchical equations of motion approach. *Phys. Rev. E*, **75**, 031107–11.

[60] Shi, Q., Chen, L., Nan, G., Xu, R. & Yan, Y. (2009). Efficient hierarchical Liouville space propagator to quantum dissipative dynamics. *J. Chem. Phys.*, **130**, 084105–4.

[61] Chen, L., Zheng, R., Shi, Q. & Yan, Y. (2009). Optical line shapes of molecular aggregates: Hierarchical equations of motion method. *J. Chem. Phys.*, **131**, 094502–11.

[62] Kleinekathöfer, U. (2004). Non-Markovian theories based on a decomposition of the spectral density. *J. Chem. Phys.*, **121**, 2505.

[63] Schröder, M., Schreiber, M. & Kleinekathöfer, U. (2007). Reduced dynamics of coupled harmonic and anharmonic oscillators using higher-order perturbation theory. *J. Chem. Phys.*, **126**, 114102.

[64] Ishizaki, A. & Fleming, G. R. (2009). On the adequacy of the Redfield equation and related approaches to the study of quantum dynamics in electronic energy transfer. *J. Chem. Phys.*, **130**, 234110–8.

[65] Kreisbeck, C., Kramer, T., Rodriguez, M. & Hein, B. (2011). High-performance solution of hierarchial equations of motions for studying energy-transfer in light-harvesting complexes. *J. Chem. Theor. Comp.*

[66] Chen, X. & Silbey, R. J. (2011). Excitation energy transfer in a non-Markovian dynamical disordered enviornment: localization, narrowing, and transfer efficiency. *JPCB*, **115**, 5499–5509.

[67] Hein, B., Kreisbeck, C., Kramer, T. & Rodríguez, M. (2012). Modelling of oscillations in two-dimensional echo-spectra of the fenna–matthews–olson complex. *New J. Phys.*, **14**, 023018.

[68] Yan, Y. J. & Xu, R. X. (2005). Quantum mechanics of dissipative systems. *Annu. Rev. Phys. Chem.*, **56**, 187.

[69] Tian, B., Ding, J., Xu, R. & Yan, Y. (2010). Biexponential theory of drude dissipation via hierarchical quantum master equation. *J. Chem. Phys.*, **133**, 114112.

[70] Hu, J., Xu, R. & Yan, Y. (2010). Communication: Padé spectrum decomposition of fermi function and bose function. *J. Chem. Phys.*, **133**, 101106.

[71] Meier, C. & Tannor, D. (1999). Non-markovian evolution of the density operator in the presence of strong laser fields. *J. Chem. Phys.*, **111**, 3365.

[72] Trinkunas, G. & Freiberg, A. (2006). A disordered polaron model for polarized fluorescence excitation spectra of LH1 and LH2 bacteriochlorophyll antenna aggregates. *J. Luminesc.*, **119-120**, 105–110.

[73] Janusonis, J., Valkunas, L., Rutkauskas, D. & van Grondelle, R. (2008). Spectral dynamics of individual bacterial Light-Harvesting complexes: Alternative disorder model. *Biophys. J.*, **94**, 1348–1358.

[74] van Grondelle, R. & Novoderezhkin, V. I. (2006). Energy transfer in photosynthesis: experimental insights and quantitative models. *Phys. Chem. Chem. Phys.*, **8**, 793–807.

[75] Şener, M. & Schulten, K. (2002). A general random matrix approach to account for the effect of static disorder on the spectral properties of light harvesting systems. *Phys. Rev. E*, **65**, 031916. (12 pages).

[76] Zhu, K., Xu, R., Zhang, H., Hu, J. & Yan, Y. (2011). Hierarchical dynamics of correlated system- environment coherence and optical spectroscopy. *J. Phys. Chem. B*, **115**, 5678–5684.

[77] Cogdell, R., Isaacs, N., Freer, A., Arrelano, J., Howard, T., Papiz, M., Hawthornthwaite-Lawless, A. & Prince, S. (1997). The structure and function of the lh2 (b800-b850) complex from the purple bacterium *rhodopseudomonas acidophila* strain 10050. *Progr. Biophys. Molec. Biol.*, **68**, 1–27.

[78] Pullerits, T. & Sundström, V. (1996). Photosynthetic light-harvesting pigment-protein complexes: Toward understanding how and why. *Acc. Chem. Res.*, **29**, 381–389.

[79] Blankenship, R. E., Madigan, M. T. & Bauer, C. E., eds. (1995). *Anoxygenic Photosynthetic Bacteria*. Kluwer Academic Publishers.

[80] Fleming, G. R. & van Grondelle, R. (1997). Femtosecond spectroscopy of photosynthetic light-harvesting systems. *Curr. Opin. Struct. Biol.*, **7**, 738–48.

[81] Şener, M. K. & Schulten, K. (2008). From atomic-level structure to supramolecular organization in the photosynthetic unit of purple bacteria. In C. N. Hunter, F. Daldal, M. C. Thurnauer & J. T. Beatty, eds., *The Purple Phototrophic Bacteria*, volume 28 of *Advances in Photosynthesis and Respiration*, 275–294. Springer.

[82] Sundström, V., Pullerits, T. & van Grondelle, R. (1999). Photosynthetic light-harvesting: Reconciling dynamics and structure of purple bacterial LH2 reveals function of photosynthetic unit. *J. Phys. Chem. B*, **103**, 2327–2346.

[83] Novoderezhkin, V. I. & Razjivin, A. P. (1996). The theory of forster-type migration between clusters of strongly interacting molecules: application to light-harvesting complexes of purple bacteria. *Chem. Phys.*, **211**, 203–214.

[84] Novoderezhkin, V. I. & van Grondelle, R. (2002). Exciton-vibrational relaxation and transient absorption dynamics in LH1 of *Rhodopseudomonas viridis*: A Redfield theory approach. *J. Phys. Chem. B*, **106**, 6025–6037.

[85] Novoderezhkin, V. I., Rutkauskas, D. & van Grondelle, R. (2006). Dynamics of the emission spectrum of a single LH2 complex: Interplay of slow and fast nuclear motions. *Biophys. J.*, **90**, 2890–2902.

[86] Valkunas, L., Janusonis, J., Rutkauskas, D. & van Grondelle, R. (2007). Protein dynamics revealed in the excitonic spectra of single LH2 complexes. *J. Luminesc.*, **127**, 269–275.

[87] Yang, M. & Fleming, G. R. (2002). Influence of phonons on exciton transfer dynamics: comparison of the Redfield, Förster, and modified Redfield equations. *Chem. Phys.*, **282**, 163–180.

[88] May, V. (2006). Open system dynamics approach to polyatomic molecules: Excitons in chromophore complexes. *Int. J. Quantum Chem.*, **106**.

[89] Kühn, O. & Sundström, V. (1997). Pump–probe spectroscopy of dissipative energy transfer dynamics in photosynthetic antenna complexes: A density matrix approach. *J. Chem. Phys.*, **107**, 4154–4164.

[90] Renger, T., May, V. & Kühn, O. (2001). Ultrafast excitation energy transfer dynamics in photosynthetic pigment-protein complexes. *Phys. Rep.*, **343**, 137–254.

[91] Zhang, W. M., Meier, T., Chernyak, V. & Mukamel, S. (1998). Exciton-migration and three-pulse femtosecond optical spectroscopies of photosynthetic antenna complexes. *J. Chem. Phys.*, **108**, 7763–7774.

[92] Damjanović, A., Ritz, T. & Schulten, K. (2000). Excitation energy trapping by the reaction center of *Rhodobacter sphaeroides*. *Int. J. Quantum Chem.*, **77**, 139–151.

[93] van Oijen, A. M., Katelaars, M., Köhler, J., Aartsma, T. J. & Schmidt, J. (1999). Unraveling the electronic structure of individual photosynthetic pigment-protein complexes. *Science*, **285**, 400–402.

[94] Tretiak, S., Middleton, C., Chernyak, V. & Mukamel, S. (2000). Bacteriochlorophyll and caretoid excitonic couplings in the LH2 system of purple bacteria. *J. Phys. Chem. B*, **104**, 9540–9553.

[95] Ritz, T., Damjanović, A. & Schulten, K. (2002). The quantum physics of photosynthesis. *ChemPhysChem*, **3**, 243–248.

[96] Zerlauskiene, O., Trinkunas, G., Gall, A., Robert, B., Urboniene, V. & Valkunas, L. (2008). Static and dynamic protein impact on electronic properties of Light-Harvesting complex LH2. *J. Phys. Chem. B*, **112**, 15883–15892.

[97] Freiberg, A., Ratsep, M., Timpmann, K. & Trinkunas, G. (2009). Excitonic polarons in quasi-one-dimensional LH1 and LH2 bacteriochlorophyll a antenna aggregates from photosynthetic bacteria: A wavelength-dependent selective spectroscopy study. *Chem. Phys.*, **357**, 102–112.

[98] Damjanović, A., Kosztin, I., Kleinekathoefer, U. & Schulten, K. (2002). Excitons in a photosynthetic light-harvesting system: A combined molecular dynamics, quantum chemistry and polaron model study. *Phys. Rev. E*, **65**, 031919. (24 pages).

[99] Liu, W., Yan, Y., Liu, K., Xu, C. & Qian, S. (2006). The study of photo-induced ultrafast dynamics in light-harvesting complex LH2 of purple bacteria. *Front. Phys. China*, **1**, 283–294.

[100] Vulto, S., Kennis, J., Streltsov, A., Amesz, J. & Aartsma, T. (1999). Energy relaxation within the B850 absorption band of the isolated light-harvesting complex LH2 from *rhodopseudomonas acidophila* at low temperature. *J. Phys. Chem. B*, **103**, 878–883.

[101] Visser, H. M., Somsen, O. J. G., van Mourik, F. & van Grondelle, R. (1996). Excited state energy equillibration via subpicosecond energy transfer within the inhomogeneously broadened light-harvesting antenna of lh-1-only *rhodobacter sphaeroides* mutants m2192 at room temperature and 4.2 k. *J. Phys. Chem.*, **100**, 18859–18867.

[102] Bradforth, S. E., Jimenez, R., van Mourik, F., van Grondelle, R. & Fleming, G. R. (1995). Excitation transfer in the core light-harvesting complex (LH-1) of rhodobacter sphaeroides: an ultrafast fluorescence depolarization and annihilation study. *J. Phys. Chem.*, **99**, 16179–16191.

[103] Freiberg, A., Godik, V. I., Pullerits, T. & Timpmann, K. (1989). Picosecond dynamics of directed excitation transfer in spectrally heterogeneous light-harvesting antenna of purple bacteria. *Biochim. Biophys. Acta*, **973**, 93–104.

[104] Herman, P., Kleinekathöfer, U., Barvík, I. & Schreiber, M. (2001). Exciton scattering in light-harvesting systems of purple bacteria. *J. Luminesc.*, **94-95**, 447–450.

[105] Linnanto, J. & Korppi-Tommola, J. (2009). Modelling excitonic energy transfer in the photosynthetic unit of purple bacteria. *Chem. Phys.*, **357**, 171–180.

[106] Ritz, T., Park, S. & Schulten, K. (2001). Kinetics of excitation migration and trapping in the photosynthetic unit of purple bacteria. *J. Phys. Chem. B*, **105**, 8259–8267.

[107] Jang, S., Newton, M. D. & Silbey, R. J. (2004). Multichromophoric Förster resonance energy transfer. *Phys. Rev. Lett.*, **92**, 218301.

[108] Scholes, G. D. (2003). Long-range resonance energy transfer in molecular systems. *Annu. Rev. Phys. Chem.*, **54**, 57–87.

[109] Monshouwer, R., Abrahamsson, M., van Mourik, F. & van Grondelle, R. (1997). Superradiance and exciton delocalization in bacterial photosynthetic light-harvesting systems. *J. Phys. Chem. B*, **101**, 7241–7248.

[110] Kosztin, I. & Schulten, K. (2008). Molecular dynamics methods for bioelectronic systems in photosynthesis. In T. Aartsma & J. Matysik, eds., *Biophysical Techniques in Photosynthesis II*, volume 26 of *Advances in Photosynthesis and Respiration*, 445–464. Springer, Dordrecht.

[111] Förster, T. (1948). Zwischenmolekulare Energiewanderung und Fluoreszenz. *Ann. Phys. (Leipzig)*, **2**, 55–75.

[112] Redfield, A. G. (1965). The theorie of relaxation process. *Adv. Magn. Reson.*, **1**, 1.

[113] Haken, H. & Strobl, G. (1973). An exactly solvable model for coherent and incoherent exciton motion. *Z. Physik A*, **262**, 135–148.

[114] Renger, T. & Marcus, R. A. (2002). On the relation of protein dynamics and exciton relaxation in pigment-protein complexes: An estimation of the spectral density and a theory for the calculation of optical spectra. *J. Chem. Phys.*, **116**, 9997–10019.

[115] Kühn, O. & Tanimura, Y. (2003). Two-dimensional vibrational spectroscopy of a double minimum system in a dissipative environment. *J. Chem. Phys.*, **119**, 2155.

[116] Ishizaki, A., Calhoun, T. R., Schlau-Cohen, G. S. & Fleming, G. R. (2010). Quantum coherence and its interplay with protein environments in photosynthetic electronic energy transfer. *Phys. Chem. Chem. Phys.*, **12**. In press.

[117] Olbrich, C. & Kleinekathöfer, U. (2010). Time-dependent atomistic view on the electronic relaxation in light-harvesting system II. *J. Phys. Chem. B.* In press.

[118] Hennebicq, E., Beljonne, D., Curutchet, C., Scholes, G. D. & Silbey, R. J. (2009). Shared-mode assisted resonant energy transfer in the weak coupling regime. *J. Chem. Phys.*, **130**, 214505–6.

[119] Allen, J., Yeates, T., Komiya, H. & Rees, D. (1987). Structure of the reaction center from *Rhodobacter sphaeroides* R-26: the protein subunits. *Proc. Natl. Acad. Sci. U.S.A.*, **84**, 6162–6166.

[120] Allen, J., Yeates, T., Komiya, H. & Rees, D. (1987). Structure of the reaction center from *Rhodobacter sphaeroides* R-26: the cofactors. *Proc. Natl. Acad. Sci. U.S.A.*, **84**, 5730–5734.

[121] Jonas, D. M., Lang, M. J., Nagasawa, Y., Joo, T. & Fleming, G. R. (1996). Pump-probe polarization anisotropy study of femtosecond energy transfer within the photosynthetic reaction center of *rhodobacter sphaeroides* r26. *J. Phys. Chem.*, **100**, 12660–12673.

[122] Cherepy, N., Shreve, A., Moore, L., Boxer, S. & Mathies, R. (1997). Temperature dependence of the qy resonance raman spectra of bacteriochlorophylls, the primary electron donor, and bacteriopheophytins in the bacterial photosynthetic reaction center. *Biochemistry*, **36**, 8559–8566.

[123] Hu, X., Damjanović, A., Ritz, T. & Schulten, K. (1998). Architecture and function of the light harvesting apparatus of purple bacteria. *Proc. Natl. Acad. Sci. USA*, **95**, 5935–5941.

[124] Won, Y. & Friesner, R. A. (1988). Simulation of optical spectra from reaction center of *rhodopseudomonas viridis*. *J. Phys. Chem.*, **92**, 2208–2214.

[125] Timpmann, K., Zhang, F., Freiberg, A. & Sundström, V. (1993). Detrapping of excitation energy from the reaction centre in the photosynthetic purple bacterium *rhodospirillum rubrum*. *Biochim. Biophys. Acta – Bioener.*, **1183**, 185–193.

[126] Timpmann, K., Freiberg, A. & Sundström, V. (1995). Energy trapping and detrapping in the photosynthetic bacterium *rhodopseudomonas viridis*: transfer-to-trap-limited dynamics. *Chem. Phys.*, **194**, 275–283.

[127] Pawlowicz, N., Van Grondelle, R., Van Stokkum, I., Breton, J., Jones, M. & Groot, M. (2008). Identification of the first steps in charge separation in bacterial photosynthetic reaction centers of rhodobacter sphaeroides by ultrafast mid-infrared spectroscopy: electron transfer and protein dynamics. *Biophys. J.*, **95**, 1268–1284.

[128] Cheng, Y. & Fleming, G. (2009). Dynamics of light harvesting in photosynthesis. *Annu. Rev. Phys. Chem.*, **60**, 241–262.

[129] Lin, S., Jaschke, P., Wang, H., Paddock, M., Tufts, A., Allen, J., Rosell, F., Mauk, A., Woodbury, N. & Beatty, J. (2009). Electron transfer in the rhodobacter sphaeroides reaction center assembled with zinc bacteriochlorophyll. *Proc. Natl. Acad. Sci. USA*, **106**, 8537.

[130] Pawlowicz, N. P., van Stokkum, I. H., Breton, J., van Grondelle, R. & Jones, M. R. (2009). Identification of the intermediate charge-separated state in a leucine m214 to histidine mutant of the rhodobacter sphaeroides reaction center using femtosecond midinfrared spectroscopy. *Biophys. J.*, **96**, 4956 – 4965.

[131] Collins, A. M., Kirmaier, C., Holten, D. & Blankenship, R. E. (2011). Kinetics and energetics of electron transfer in reaction centers of the photosynthetic bacterium roseiflexus castenholzii. *Biochim. Biophys. Acta – Bioener.*, **1807**, 262 – 269.

[132] Guo, Z., Lin, S., Xin, Y., Wang, H., Blankenship, R. & Woodbury, N. (2011). Comparing the temperature dependence of photosynthetic electron transfer in chloroflexus aurantiacus and rhodobactor sphaeroides reaction centers. *J. Phys. Chem. B.*

[133] Kirmaier, C., Holten, D. & Parson, W. (1985). Temperature and detection-wavelength dependence of the picosecond electron-transfer kinetics measured in rhodopseudomonas sphaeroides reaction centers. resolution of new spectral and kinetic components in the primary charge-separation process. *Biochim. Biophys. Acta – Bioener.*, **810**, 33–48.

[134] Steffen, M., Lao, K. & Boxer, S. (1994). Dielectric asymmetry in the photosynthetic reaction center. *Science*, **264**, 810–816.

[135] van Brederode, M. E. & van Grondelle, R. (1999). New and unexpected routes for ultrafast electron transfer in photosynthetic reaction centers. *FEBS Lett.*, **455**, 1–7.

[136] van Brederode, M., van Mourik, F., van Stokkum, I., Jones, M. & van Grondelle, R. (1999). Multiple pathways for ultrafast transduction of light energy in the photosynthetic reaction center of *rhodobacter sphaeroides*. *Proc. Natl. Acad. Sci. USA*, **96**, 2054–2059.

[137] Chuang, J., Boxer, S., Holten, D. & Kirmaier, C. (2008). Temperature dependence of electron transfer to the m-side bacteriopheophytin in rhodobacter capsulatus reaction centers. *J. Phys. Chem. B*, **112**, 5487–5499.

[138] Wang, H., Hao, Y., Jiang, Y., Lin, S. & Woodbury, N. W. (2012). Role of protein dynamics in guiding electron-transfer pathways in reaction centers from rhodobacter sphaeroides. *J. Phys. Chem. B*, **116**, 711–717.

[139] Lee, H., Cheng, Y.-C. & Fleming, G. R. (2007). Coherence dynamics in photosynthesis: Protein protection of excitonic coherence. *Science*, **316**, 1462–1465.

[140] Pullerits, T., Visscher, K. J., Hess, S., Sundström, V., Freiberg, A. & Timpmann, K. (1994). Energy transfer in the inhomogeneously broadened core antenna of purple bacteria: A simultaneous fit of low-intensity picosecond absorption and fluorescence kinetics. *Biophys. J.*, **66**, 236–248.

[141] Jordanides, X., Scholes, G. & Fleming, G. (2001). The mechanism of energy transfer in the bacterial photosynthetic reaction center. *J. Phys. Chem. B*, **105**, 1652–1669.

[142] Chang, C., Hayashi, M., Liang, K., Chang, R. & Lin, S. (2001). A theoretical analysis of absorption spectra of photosynthetic reaction centers: Mechanism of temperature dependent peak shift. *J. Phys. Chem. B*, **105**, 1216–1224.

[143] Jordanides, X., Scholes, G., Shapley, W., Reimers, J. & Fleming, G. (2004). Electronic couplings and energy transfer dynamics in the oxidized primary electron donor of the bacterial reaction center. *J. Phys. Chem. B*, **108**, 1753–1765.

[144] Linnanto, J. & Korppi-Tommola, J. (2006). Quantum chemical simulation of excited states of chlorophylls, bacteriochlorophylls and their complexes. *Phys. Chem. Chem. Phys.*, **8**, 663–687.

[145] Jing, Y., Zheng, R., Li, H. & Shi, Q. (2012). Theoretical study of the electronic-vibrational coupling in the q_y states of the photosynthetic reaction center in purple bacteria. *J. Phys. Chem. B.*

[146] Dilworth, Y., Lee, H. & Fleming, G. (2007). Measuring electronic coupling in the reaction center of purple photosynthetic bacteria by two-color, three-pulse photon echo peak shift spectroscopy. *J. Phys. Chem. B*, **111**, 7449–7456.

[147] Cheng, Y., Lee, H. & Fleming, G. (2007). Efficient simulation of three-pulse photon-echo signals with application to the determination of electronic coupling in a bacterial photosynthetic reaction center. *J. Phys. Chem. A*, **111**, 9499–9508.

[148] Frolov, D., Marsh, M., Crouch, L. I., Fyfe, P. K., Robert, B., van Grondelle, R., Hadfield, A. & Jones, M. R. (2010). Structural and spectroscopic consequences of hexacoordination of a bacteriochlorophyll cofactor in the rhodobacter sphaeroides reaction center,. *Biochemistry*, **49**, 1882–1892.

[149] Vassiliev, S., Mahboob, A. & Bruce, D. (2011). Calculation of chromophore excited state energy shifts in response to molecular dynamics of pigment–protein complexes. *Photosyn. Res.*, 1–14.

[150] Linnanto, J., Freiberg, A. & Korppi-Tommola, J. (2011). Quantum chemical simulations of excited-state absorption spectra of photosynthetic bacterial reaction center and antenna complexes. *J. Phys. Chem. B*.

[151] Kelly, A. & Rhee, Y. (2011). Mixed quantum-classical description of excitation energy transfer in a model fenna- matthews- olsen complex. *J. Phys. Chem. Lett.*, **2**, 808–812.

[152] Ishizaki, A. & Fleming, G. (2011). On the interpretation of quantum coherent beats observed in two-dimensional electronic spectra of photosynthetic light harvesting complexes. *J. Phys. Chem. B*.

[153] Jimenez, R., van Mourik, F., Yu, J. Y. & Fleming, G. R. (1997). Three-pulse photon echo measurements on LH1 and LH2 complexes of *Rhodobacter sphaeroides*: A nonlinear spectroscopic probe of energy transfer. *J. Phys. Chem. B*, **101**, 7350–7359.

[154] van Grondelle, R., Dekker, J. P., Gillbro, T. & Sundström, V. (1994). Energy transfer and trapping in photosynthesis. *Biochim. Biophys. Acta*, **1187**, 1–65.

[155] Freiberg, A. (2004). Coupling of antennas to reaction centers. *Anoxygenic Photosynthetic Bacteria*, 385–398.

[156] Hopfield, J. J. (1974). Electron transfer between biological molecules by thermally activated tunneling. *Proc. Natl. Acad. Sci. USA*, **71**, 3640–3644.

[157] Marcus, R. A. & Sutin, N. (1985). Electron transfers in chemistry and biology. *Biochim. Biophys. Acta*, **811**, 265–322.

[158] Redfield, A. (1957). On the theory of relaxation processes. *IBM Journal of Research and Development*, **1**, 19–31.

[159] McLachlan, A. D. (1964). A variational solution of the time-dependent schrodinger equation. *Mol. Phys.*, **8**, 39.

[160] Micha, D. A. (1983). A self-consistent eikonal treatment of electronic transitions in molecular collisions. *J. Chem. Phys*, **78**, 7138–45.

[161] Haken, H. & Reineker, P. (1972). The coupled coherent and incoherent motion of excitons and its influence on the line shape of optical absorption. *Z. Physik A*, **249**, 253–268.

[162] Mukamel, S. (1995). *Principles of Nonlinear Optical Spectroscopy*. Oxford University Press, New York.

[163] Weiss, U. (2008). *Quantum dissipative systems*. World Scientific Publishing Company.

[164] Breuer, H. P. & Petruccione, F. (2002). *The theory of open quantum systems*. Oxford University Press, USA.

[165] Tanimura, Y. (2006). Stochastic Liouville, Langevin, Fokker–Planck, and master equation approaches to quantum dissipative systems. *J. Phys. Soc. Jpn.*, **75**, 082001.

[166] Ishizaki, A. & Tanimura, Y. (2007). Dynamics of a multimode system coupled to multiple heat baths probed by two-dimensional infrared spectroscopy. *J. Phys. Chem. A*, **111**, 9269–9276.

[167] Xu, R. X., Tian, B. L., Xu, J. & Yan, Y. J. (2009). Exact dynamics of driven brownian oscillators. *J. Chem. Phys.*, **130**, 074107–8.

[168] Wientjes, E., Van Stokkum, I., Van Amerongen, H. & Croce, R. (2011). Excitation-energy transfer dynamics of higher plant photosystem i light-harvesting complexes. *Biophys. J.*, **100**, 1372–1380.

[169] Croce, R. & Van Amerongen, H. (2011). Light-harvesting and structural organization of photosystem ii: From individual complexes to thylakoid membrane. *J. Photochem. Photobiol. B*, **104**, 142–153.

[170] Scholes, G., Fleming, G., Olaya-Castro, A. & van Grondelle, R. (2011). Lessons from nature about solar light harvesting. *Nat. Chemistry*, **3**, 763–774.

[171] Bolinger, J. C., Traub, M. C., Adachi, T. & Barbara, P. F. (2011). Ultralong-range polaron-induced quenching of excitons in isolated conjugated polymers. *Science*, **331**, 565–567.

[172] Imahori, H. (2004). Giant multiporphyrin arrays as artificial light-harvesting antennas. *J. Phys. Chem. B*, **108**, 6130–6143.

[173] Blankenship, R. E. (2002). *Molecular Mechanisms of Photosynthesis*. Blackwell Science, Malden, MA.

[174] Fehlberg, E. (1985). Some old and new Runge-Kutta formulas with stepsize control and their error coefficients. *Computing*, **34**, 265–270.

[175] Hess, S., Chachisvilis, M., Timpmann, K., Jones, M., Fowler, G., Hunter, C. & Sundström, V. (1995). Temporally and spectrally resolved subpicosecond energy transfer within the peripheral antenna complex (LH2) and from LH2 to the core antenna complex in photosynthetic purple bacteria. *Proc. Natl. Acad. Sci. USA*, **92**, 12333–12337.

[176] Sakurai, A. & Tanimura, Y. (2011). Does $\hbar$ play a role in multidimensional spectroscopy? reduced hierarchy equations of motion approach to molecular vibrations. *J. Phys. Chem. A*.

[177] Tanaka, M. & Tanimura, Y. (2009). Quantum dissipative dynamics of electron transfer reaction system: Nonperturbative hierarchy equations approach. *J. Phys. Soc. Jpn.*, **78**, 73802.

[178] Dijkstra, A. G. & Tanimura, Y. (2010). Correlated fluctuations in the exciton dynamics and spectroscopy of dna. *New J. Phys.*, **12**, 055005.

[179] Xu, D. & Schulten, K. (1994). Coupling of protein motion to electron transfer in a photosynthetic reaction center: Investigating the low temperature behaviour in the framework of the spin-boson model. *Chem. Phys.*, **182**, 91–117.

[180] Palma, G. M., Suominen, K.-A. & Ekert, A. K. (1996). Quantum computers and dissipation. *Proc. R. Soc. A*, **452**, 567–584.

[181] Stamp, P. & Gaita-Ariño, A. (2009). Spin-based quantum computers made by chemistry: hows and whys. *J. Mater. Chem*, **19**, 1718–1730.

[182] Caruso, F., Huelga, S. F. & Plenio, M. B. (2010). Noise-enhanced classical and quantum capacities in communication networks. *Phys. Rev. Lett.*, **105**, 190501.

[183] Timpmann, K., Trinkunas, G., Qian, P., Hunter, C. N. & Freiberg, A. (2005). Excitons in core LH1 antenna complexes of photosynthetic bacteria: Evidence for strong resonant coupling and off-diagonal disorder. *Chem. Phys. Lett.*, **414**, 359–363.

[184] Freiberg, A., Rätsep, M., Timpmann, K., Trinkunas, G. & Woodbury, N. W. (2003). Self-Trapped excitons in LH2 antenna complexes between 5 k and ambient temperature. *J. Phys. Chem. B*, **107**, 11510–11519.

[185] Sumi, H. (2001). Bacterial photosynthesis begins with quantum-mechanical coherence. *Chem. Rec.*, **1**, 480–493.

[186] Zhao, Y., Meier, T., Zhang, W., Chernyak, V. & Mukamel, S. (1999). Superradiance coherence size in single-molecule spectroscopy of lh2 antenna complexes. *J. Phys. Chem. B*, **103**, 3954–3962.

[187] Meier, T., Chernyak, V. & Mukamel, S. (1997). Multiple exciton coherence sizes in photosynthetic antenna complexes viewed by pumpprobe spectroscopy. *J. Phys. Chem. B*, **101**, 7332–7342.

[188] Caycedo-Soler, F., Rodríguez, F. J., Quiroga, L. & Johnson, N. F. (2010). Interplay between excitation kinetics and reaction-center dynamics in purple bacteria. *New J. Phys.*, **12**, 095008.

[189] Leegwater, J. A. (1996). Coherent versus incoherent energy transfer and trapping in photosynthetic antenna complexes. *J. Phys. Chem.*, **100**, 14403–14409.

[190] Sumi, H. (1999). Theory on rates of excitation-energy transfer between molecular aggregates through distributed transition dipoles with application to the antenna system in bacterial photosynthesis. *J. Phys. Chem. B*, **103**, 252–260.

[191] Scholes, G. D., Jordanides, X. J. & Fleming, G. R. (2001). Adapting the förster theory of energy transfer for modeling dynamics in aggregated molecular assemblies. *J. Phys. Chem. B*, **105**, 1640–1651.

[192] Cheng, Y. C. & Silbey, R. J. (2006). Coherence in the b800 ring of purple bacteria lh2. *Phys. Rev. Lett.*, **96**, 028103.

[193] Jang, S., Newton, M. D. & Silbey, R. J. (2007). Multichromophoric förster resonance energy transfer from b800 to b850 in the light harvesting complex 2: Evidence for subtle energetic optimization by purple bacteria. *J. Phys. Chem. B*, **111**, 6807–6814.

[194] Ginsberg, N. S., Cheng, Y.-C. & Fleming, G. R. (2009). Two-dimensional electronic spectroscopy of molecular aggregates. *Acc. Chem. Res.*, **42**, 1352–1363.

[195] Scholes, G. (2010). Quantum-coherent electronic energy transfer: Did nature think of it first? *J. Phys. Chem. Lett.*, **1**, 2–8.

[196] Brixner, T., Stenger, J., Vaswani, H. M., Cho, M., Blankenship, R. E. & Fleming, G. R. (2005). Two-dimensional spectroscopy of electronic couplings in photosynthesis. *Nature*, **434**, 625–628.

[197] Gregory, S., Tessa, R., Elizabeth, L., Tae-Kyu Ahn, T., Mančal, T., Cheng, Y.-C., Blankenship, R. & Fleming, G. (2007). Evidence for wavelike energy transfer through quantum coherence in photosynthetic systems. *Nature*, **446**, 782–786.

[198] Panitchayangkoon, G., Hayes, D., Fransted, K. A., Caram, J. R., Harel, E., Wen, J., Blankenship, R. E. & Engel, G. S. (2010). Long-lived quantum coherence in photosynthetic complexes at physiological temperature. *Proc. Natl. Acad. Sci. USA*, **107**, 12766–12770.

[199] Collini, E., Wong, C. Y., Wilk, K. E., Curmi, P. M. G., Brumer, P. & Scholes, G. D. (2010). Coherently wired light-harvesting in photosynthetic marine algae at ambient temperature. *Nature*, **463**, 644–647.

[200] Hayes, D., Wen, J., Panitchayangkoon, G., Blankenship, R. & Engel, G. (2011). Robustness of electronic coherence in the fenna–matthews–olson complex to vibronic and structural modifications. *Faraday Discuss.*

[201] Olaya-Castro, A., Lee, C. F., Olsen, F. F. & Johnson, N. F. (2008). Efficiency of energy transfer in a light-harvesting system under quantum coherence. *Phys. Rev. B*, **78**, 085115.

[202] Cogdell, R. J., Gall, A. & Köhler, J. (2006). The architecture and function of the light-harvesting apparatus of purple bacteria: from single molecules to *in vivo* membranes. *Quart. Rev. Biophys.*, **39**, 227–324.

[203] Breton, J., Martin, J.-L., Migus, A., Antonetti, A. & Orszag, A. (1986). Femtosecond spectroscopy of excitation energy transfer and initial charge separation in the reaction center of the photosynthetic bacterium rhodopseudomonas viridis. *Proc. Natl. Acad. Sci. USA*, **83**, 5121–5125.

[204] Kirmaier, C., Gaul, D., DeBrey, R., Holten, D. & Schenk, C. (1991). Charge separation in a reaction center incorporating bacteriochlorophyll for photoactive bacteriopheophytin. *Science*, **251**, 922–927.

[205] Deisenhofer, J. & Michel, H. (1989). The photosynthetic reaction center from the purple bacterium rhodopseudomonas viridis. *Science*, **245**, 1463–1473.

[206] Parson, W. W. & Warshel, A. (2008). Mechanism of charge separation in purple bacterial reaction centers. In C. N. Hunter, F. Daldal, M. C. Thurnauer & J. T. Beatty, eds., *The Purple Phototrophic Bacteria*, volume 28 of *Advances in Photosynthesis and Respiration*, 355–377. Springer Netherlands.

[207] Ha, T. (2001). Single molecule fluorescence resonance transfer. *Methods*, **25**, 78.

[208] Fruhwirth, G. O., Fernandes, L. P., Weitsman, G., Patel, G., Kelleher, M., Lawler, K., Brock, A., Poland, S. P., Matthews, D. R., Kéri, G., Barber, P. R., Vojnovic, B., Ameer-Beg, S. M., Coolen, A. C. C., Fraternali, F. & Ng, T. (2011). How förster resonance energy transfer imaging improves the understanding of protein interaction networks in cancer biology. *ChemPhysChem*, **12**, 442–461.

[209] Eccles, J., Honig, B. & Schulten, K. (1988). Spectroscopic determinants in the reaction center of *Rhodopseudomonas viridis*. *Biophys. J.*, **53**, 137–144.

[210] Richter, M. F., Baier, J., Prem, T., Oellerich, S., Francia, F., Venturoli, G., Oesterhelt, D., Southall, J., Cogdell, R. J. & Köhler, J. (2007). Symmetry matters for the electronic structure of core complexes from rhodopseudomonas palustris and rhodobacter sphaeroides pufx$^-$. *Proc. Natl. Acad. Sci. USA*, **104**, 6661–6665.

[211] Richter, M. F., Baier, J., Cogdell, R. J., Oellerich, S. & Köhler, J. (2010). The influence of symmetry on the electronic structure of the photosynthetic pigment-protein complexes from purple bacteria. In A. Gräslund, R. Rigler, J. Widengren, F. Schäfer, J. Toennies & W. Zinth, eds., *Single Molecule Spectroscopy in Chemistry, Physics and Biology*, volume 96 of *Springer Series in Chemical Physics*, 513–533. Springer Berlin Heidelberg.

[212] Cory, M. G., Zerner, M. C., Hu, X. & Schulten, K. (1998). Electronic excitations in aggregates of bacteriochlorophylls. *J. Phys. Chem. B*, **102**, 7640–7650.

[213] Herek, J. L., Fraser, N. J., Pullerits, T., Martinsson, P., Polívka, T., Scheer, H., Cogdell, R. J. & Sundström, V. (2000). B800–¿b850 energy transfer mechanism in bacterial lh2 complexes investigated by b800 pigment exchange. *Biophys. J.*, **78**, 2590–2596.

[214] Krueger, B. P., Scholes, G. D. & Fleming, G. R. (1998). Calculation of couplings and energy-tranfer pathways between the pigments of LH2 by the ab initio transition density cube method. *J. Phys. Chem. B*, **102**, 5378–5386.

[215] Hess, S., Visscher, K. J., Pullerits, T., Sundström, V., Fowler, G. J. S. & Hunter, C. N. (1994). Enhanced rates of subpicosecond energy transfer in blue-shifted light harvesting LH2 mutants of *Rhodobacter sphaeroides*. *Biochemistry*, **33**, 8300–8305.

[216] Fowler, G. J. S., Visschers, R. W., Grief, G. G., van Grondelle, R. & Hunter, C. N. (1992). Genetically modified photosynthetic antenna complexes with blueshifted absorbance bands. *Nature*, **355**, 848–850.

[217] Joliot, P., Vermeglio, A. & Joliot, A. (1989). Evidence for supercomplexes between reaction centers, cytochrome c_2 and cytochrome bc_1 complex. *Biochim. Biophys. Acta*, **975**, 336–345.

[218] Vatter, A. & Wolfe, R. (1958). The structure of photosynthetic bacteria. *J. Bacteriol.*, **75**, 480.